

## **General Disclaimer**

### **One or more of the Following Statements may affect this Document**

- This document has been reproduced from the best copy furnished by the organizational source. It is being released in the interest of making available as much information as possible.
- This document may contain data, which exceeds the sheet parameters. It was furnished in this condition by the organizational source and is the best copy available.
- This document may contain tone-on-tone or color graphs, charts and/or pictures, which have been reproduced in black and white.
- This document is paginated as submitted by the original source.
- Portions of this document are not fully legible due to the historical nature of some of the material. However, it is the best reproduction available from the original submission.

**NASA CONTRACTOR REPORT 166403**

**(NASA-CR-166403) COMPARATIVE FEASIBILITY  
STUDY OF TWO CONCEPTS FOR A SPACE-BASED  
ASTROMETRIC SATELLITE (Lockheed Missiles and  
Space Co.) 221 p HC A10/MF A01 CSCL 22B**

**N83-13137**

**G3/15 01432**  
**Unclas**

Comparative Feasibility Study of Two Concepts  
For A Space-Based Astrometric Satellite

Dr. L. Bander mann  
Dr. N. Bareket  
Dr. W. Metheny



**CONTRACT NAS2-11040**  
November 1982

**NASA**

**NASA CONTRACTOR REPORT 166403**

**Comparative Feasibility Study of Two Concepts  
For A Space-Based Astrometric Satellite**

Dr. L. Bandermann  
Dr. N. Bareket  
Dr. W. Metheny  
Lockheed Palo Alto Research Labaoratory  
Palo Alto, California

Prepared for  
Ames Research Center  
under Contract NAS2-11040



National Aeronautics and  
Space Administration

**Ames Research Center**  
Moffett Field, California 94035

FOREWORD

This report gives results of two parallel and interdependent studies carried out by Lockheed Missiles and Space Company, Inc. at the Palo Alto Research Laboratories:

1. FEASIBILITY STUDY FOR AN ASTROMETRIC SPACE TELESCOPE  
(Contract NAS2-11040, NASA/Ames)
2. FEASIBILITY STUDY OF A SPACE-BASED INTERFEROMETER  
(Contract G68100-2050, California Space Institute)

Both studies were under the guidance of Dr. D. Black (NASA/ARC). The technical monitor and NASA study manager was Mr. S. Rathjen. The principal study personnel at LMSC were Drs. L. Bander mann (study leader), N. Bareket and W. Metheny.

PRECEDING PAGE BLANK NOT FILMED



# ACKNOWLEDGEMENT

We thank Dr. G. Gatewood (Allegheny Observatory), originator of the astrometric telescope concept, and Dr. M. Shao (MIT)\*, originator of the interferometer concept, and Drs. B. Jones (UC, Santa Cruz), R. Reasenberg (MIT), and J. Scargle (NASA/ARC) for helpful discussions, critique and advice during the study.

PRECEDING PAGE BLANK NOT FILMED

\*  
Now at NRL

## SUMMARY

The objective of this effort was to conduct a comparative feasibility study of two concepts for an astrometric satellite: a visual imaging telescope with a 16.5 meter focal length, proposed by G. Gatewood (Allegheny Observatory), and a white-light interferometer with a 15 meter baseline separation, proposed by M. Shao (MIT).

The primary mission of the satellite would be to search for extra-solar planets. Other astrometric programs identified in this report and which could have a significant impact on a wide range of astrophysical problems are also feasible with the systems discussed here. The satellite would be a Shuttle-deployed free-flyer with a nominal mission of 5 years. The instrument would operate in the visible part of the spectrum, have primary optics of about 1 meter diameter, and have a field-of-view (FOV) diameter of 10 arcminutes. Measurement accuracy of relative star positions to 1 micro-arcsecond is required for the detection of an earth-mass planet in a 5-year orbit around a K5 star at a distance of 10 parsecs (32 light-years) from the Earth (baseline task).

The imaging telescope is within the state-of-the-art, and a conceptual baseline design was developed which uses available technology. An improved baseline concept makes use of advances in solid state detectors expected to occur in the next several years. The photon-noise limited integration time for the baseline task is 1-10 hours, depending on the exact nature of the stellar reference frame and on the total photon efficiency. How closely this limit can be approached depends on the development of an optimal measurement algorithm and will require extensive modeling of the system performance in the presence of systematic and random

errors identified in this report.

Our preferred baseline design for the imaging telescope has a 1 meter diameter parabolic primary mirror (no secondary mirror) and an 8 meter focal length scaled down from 16.5 meters: There is no significant loss of accuracy but a significant cost advantage with this smaller system.

The overall length of the telescope system is 13 meters, and the weight is 2900 kg. The main structure is a thermally self-compensating steel-aluminum metering truss supporting the telescope and the spacecraft. The primary mirror focusses the starlight onto a moving grating (Ronchi ruling) resulting in a modulated signal. Information about the relative positions of the stars in the FOV is encoded in the modulated signal. The grating is laser-stabilized relative to the mirror. The FOV is imaged onto a set of four CCD (Charge Coupled Device) arrays plus a separate detector for the central bright star. The focal plane is passively cooled.

The spacecraft suggested for this system is the Multi-Mission Modular Spacecraft (MMS). The MMS propulsion system is adequate to boost the satellite from Shuttle handoff at 150 n.mi. to the suggested operational altitude of 325 n. mi. The total cost of the system is \$148M in constant 1982 dollars, which includes \$92 payload (instrument) and \$56M spacecraft plus integration costs.

Comparison of the interferometer and the imaging telescope shows that the interferometer has significantly better sensitivity. However, there are two difficulties in obtaining sufficient measurement accuracy with the interferometer: One lies with instrumental errors, and the other with the fact that only a few stars in the FOV can be observed simultaneously and are thus available for reducing the systematic errors.

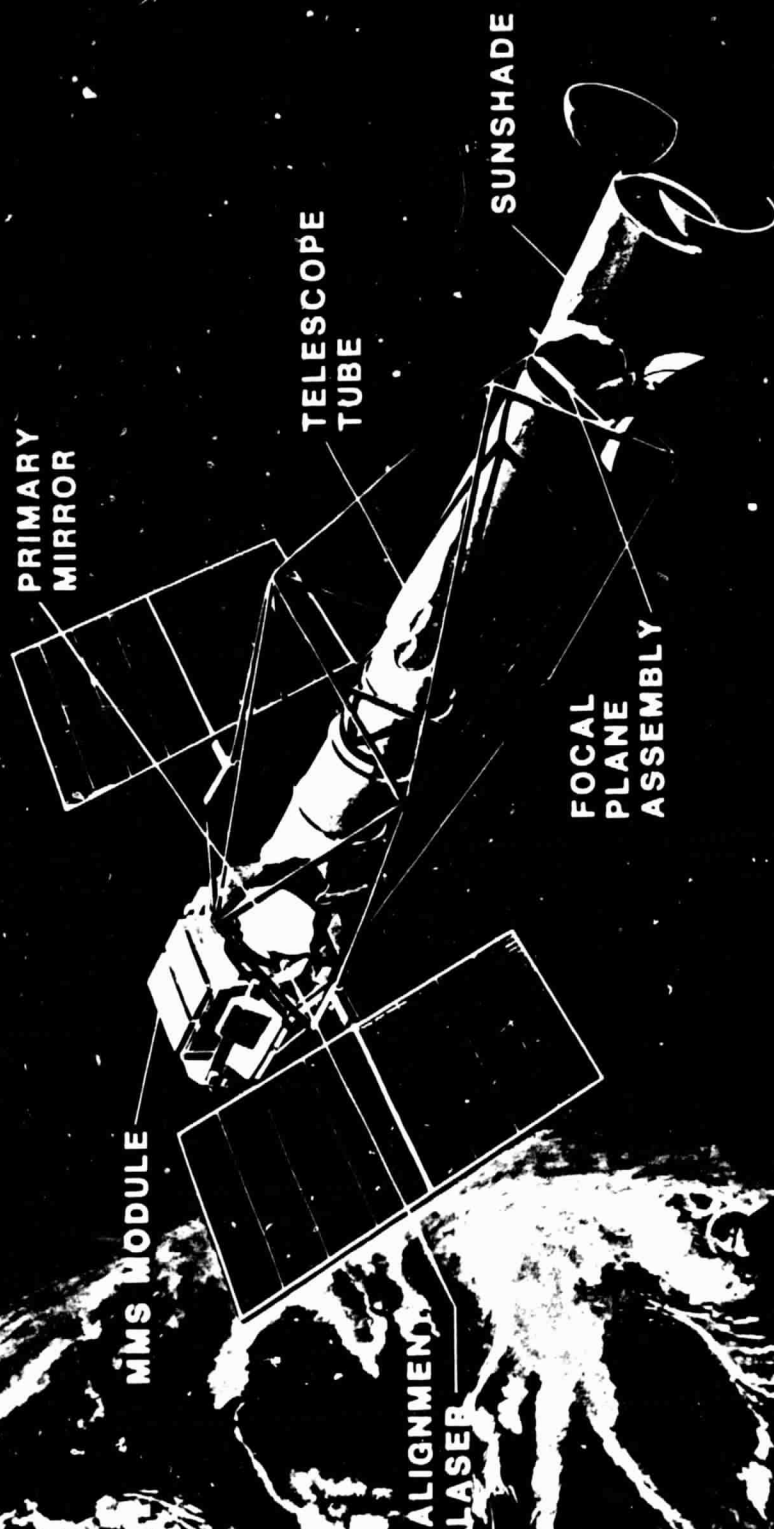
Because of the instrumental errors, the feasibility of the interferometer is questionable, and a conceptual breakthrough seems required. The principal difficulty lies with the metric stability of the gratings on the two end mirrors. These gratings are required (an acceptable alternative was not found) for measurement of the optical path difference between the two interferometer arms for each star sharing the aperture.

In contrast with the imaging telescope, the interferometer observes only a few stars simultaneously. For the initial analysis it has been assumed that four stars sharing the aperture are sufficient. The feasibility of the interferometer depends on that sufficiency, which needs to be established.

The number of monitored and actively controlled optical elements is large compared to the imaging telescope, implying a much more complex and therefore riskier system. Finally, the estimated cost of the interferometer is significantly higher, namely \$300M plus spacecraft and integration.

The question of scaling down the interferometer and adapting an existing spacecraft design (e.g. the MMS) requires further study. Many error sources identified in this report can be eliminated by calibrating all star channels simultaneously by observing the same bright star at frequent time intervals (star switching). For planetary detection a sufficiently bright star is always available. In other applications where no such star is in the FOV, the feasibility of this technique is uncertain. A larger baseline and larger end mirrors would ease the problem but increase the difficulty of manufacturing and maintaining the required optical tolerances, whereas the reverse would be true for a scaled-down system.

# ASTROMETRIC TELESCOPE



NASA  Lockheed

# CONTENTS

1. Introduction	1-1
1.1 Background	1-1
1.2 Ground versus Space	1-2
1.3 Other Space-based Systems	1-3
1.4 Science Potential	1-3
2. General Considerations	2-1
2.1 Summary	2-1
2.2 Orbit	2-1
2.3 Straylight	2-10
2.4 Stellar Image Motions	2-22
2.5 Structure	2-35
3. Interferometer	3-1
3.1 Summary	3-1
3.2 Operating Principles	3-3
3.3 Requirements and Design Implications	3-7
3.4 Alternate Optical Forms	3-12
3.5 Baseline	3-23
3.6 Subsystem Analysis	3-29
3.7 Overall System Design	3-50
3.8 Weight	3-57
3.9 Cost	3-57
4. Imaging Telescope	4-1
4.1 Summary	4-1
4.2 Principle of Operation	4-3
4.3 Algorithms for Signal Processing	4-14
4.4 Focal Plane Architecture and Detectors	4-18

4.5 Grating and Grating Drive	4-26
4.6 Optical Form	4-32
4.7 Focal Plane Assembly	4-37
4.8 Discussion of Measurement Error Sources	4-48
4.9 Telescope Baseline System	4-56
4.10 Weight	4-59
4.11 Cost	4-59
5. Interferometer-Telescope Comparison	5-1
5.1 Summary	5-1
5.2 Comparison of Speeds	5-4
5.3 Scaling	5-9
6. Scaled-down Imaging Telescope	6-1
6.1 Summary	6-1
6.2 Cost Considerations	6-1
6.3 Performance	6-15
6.4 8-m Focal Length System	6-16

## TABLES

1-1	Perturbation of Sun in $10^{-6}$ arcsec by the Planets	1-6
1-2	Selected Astrometry Missions	1-8
2-1	Orbit Inclination vs. Target Accessibility	2-6
2-2	Straylight	2-17
2-3	Motion of Stars in FOV	2-23
2-4	Stellar Aberration	2-25
3-1	Optical Forms	3-13
3-2	Image Plane Interferometer (FOV Implications)	3-18
3-3	Interferometer Weight Estimates	3-58
3-4	Interferometer Cost Estimates	3-59
4-1	Star Population and Photon Rates	4-19
4-2	PMT vs. CCD - an Example	4-23
4-3	Thermal Properties of Fused Silica and ULE	4-29
4-4	RMS Spot Size for a 1-m Diameter Parabola	4-38
4-5	Astrometric Telescope Weight Estimate	4-61
4-6	Astrometric Telescope Cost Estimate	4-62
5-1	Interferometer-Telescope Comparison	5-2/3
6-1	Spacecraft Requirements	6-7
6-2	MMS Baseline Specifications	6-8
6-3	Fuel Requirements	6-12
6-4	MMS Propulsion Systems	6-13
6-5	F/8 Telescope Weight Estimate	6-21
6-6	F/8 Telescope Cost Estimate	6-22
6-7	Dual Barrel f/8 Telescope Cost	6-25
A-1	Comparison of Instruments for Detection of Extra-Solar Planets	A-2



# ILLUSTRATIONS

1-1 Stars in 10'x10' FOV	1-4
2-1 Orbit Lifetime	2-3
2-2 Target Accessibility (example)	2-5
2-3 Shadow Time	2-7
2-4 Radiation Effects	2-8
2-5 Photon Rate to 1-m <sup>2</sup>	2-12
2-6 Zodiacal Light Brightness Contours	2-14
2-7 Photons to Airy Disk	2-18
2-8 Solar Straylight	2-20
2-9 Velocity Aberration	2-24
2-10 Projection of Stellar Motion	2-27
2-11 Gravitational Deflection of Starlight	2-28
2-12 Star Spots	2-30
2-13 Double Star	2-33
2-14 Structure Materials	2-36
3-1 Interferometer Measurement Technique	3-4
3-2 Optical System (schematic)	3-6
3-3 Interferometer Integration Time	3-10
3-4 Subaperture Geometry	3-11
3-5 Image Plane vs. Pupil Plane Interferometer	3-14
3-6 Modified Pupil Plane Interferometer	3-15
3-7 Image Plane Interferometer	3-17
3-8 Modified Image Plane Interferometer	3-20
3-9 Image Plane Intensity	3-22
3-10 Alignment System Overview	3-24
3-11 End Mirror and Beam Geometry	3-25
3-12 Trombone Optical Delay Line	3-27
3-13 Alternate Optical Configuration	3-30
3-14 Static Focus Error	3-32
3-15 Thermal Sag	3-34
3-16 Field Shift Error	3-36
3-17 Beamsplitter Errors	3-37

3-18 Mirror Tilt Errors	3-40
3-19 Mirror Translation Error	3-42
3-20 One Arm OPD System by Delay Line Measurement	3-43
3-21 two Arm OPD System	3-45
3-22 Interferometer End Mirror Layout	3-46
3-23 Grating Error	3-48
3-24 Interferometer System	3-51/52
3-25 Interferometer Deployment	3-53
3-26 Deployed Interferometer	3-55
3-56 Magnetic Bearing Assembly	3-56
4-1 Imaging Astrometric Telescope Schematic	4-4
4-2 The Function $\text{Comb}(x/d)$	4-11
4-3 Centroiding with Knife Edge	4-16
4-4 Counts/Pixel at which CCD is Better than PMT	4-22
4-5 Maximum Bandwidth for which CCD is Superior	4-24
4-6 Dark Current Generation	4-25
4-7 Temporal Resolution Obtained with Large Area CCD	4-27
4-8 Active Laser Position Sensor	4-33
4-9 Radial Energy Distribution	4-35
4-10 Radial Energy Distribution and RMS Spot Size	4-36
4-11 Split-Field Focal Plane	4-39
4-11 X-Y Measurement	4-42
4-12 Grating Misalignment	4-49
4-13 F/16.5 Imaging Telescope System	4-57/58
4-14 Structure Resonance Frequency	4-59
5-1 Speed of Instruments	5-7
6-1 Athermal Truss Concept	6-4
6-2 MMS Subsystems	6-9
6-3 Shuttle Payload Capacity	6-11
6-4 F/8 Astrometric Telescope System	6-17
6-5 Structure Resonance Frequency	6-18
6-6 Weight and Cost of Telescopes	6-24
6-7 Cost-Effectiveness	6-26

## ACRONYMS

ACS	Attitude Control System
BRDF	Bidirectional Reflection Distribution Function
CCD	Charge Coupled Device
CID	Charge Injected Device
FP	Focal Plane
FPA	Focal Plane Assembly
FOV	Field Of View
GFE	Government Furnished Equipment
GHE	Ground Handling Equipment
Gr/Ep	Graphite-Epoxy
GSE	Ground Support Equipment
LOS	Line Of Sight
LSF	Line Spread Function
L/V	Launch Vehicle
MLI	Multi-Layer Insulation
MMS	Multi-Mission Modular Spacecraft
OA	Optical Axis
OPD	Optical Path Difference
OTF	Optical Transfer Function
PSF	Point Spread Function
SNR	Signal-to-Noise-Ratio
S/C	Spacecraft
SSM	System Support Module (ST spacecraft)
ST	Space Telescope
ULE	Ultra-Low Expansion material
WF	Wavefront

## 1. INTRODUCTION

### 1.1 Background

The space environment offers major advantages for astronomy, due to the absence of gravity and of the atmosphere. Astronomy is concerned with basically two types of observations: (i) the energy distribution of the radiation of astronomical sources, as a function of wavelength, and (ii) the position of astronomical sources. In general, the larger the collecting area of a telescope, the greater its ability to provide better spectral as well as positional data. Therefore, there is a drive toward very large apertures in space (viz. Space Telescope (ST); Large Deployable Reflector (LDR)). However, for positional astronomy, large gains over ground based instruments can be obtained with space-based systems of relatively small apertures ( $\sim 1$ -m diameter) and operating in the visible.

This report gives the results of a comparative feasibility study conducted on the concept level for two visual, space-based astrometric systems: an imaging telescope and an interferometer, both with collecting apertures of about 1-m diameter. A number of fundamental problems can be addressed with the proposed systems, foremost among them being the existence and statistics of other planetary systems. The systems can also provide a better calibration of certain fundamental astrophysical quantities. The expense of a rather specialized instrument is therefore far outweighed by the potential of major advances in astronomy and astrophysics.

## 1.2 Ground versus Space

Theoretically, there is a gain of several orders of magnitude in astrometric accuracy by going from ground to space. For a perfect detector the error in position determination after an integration time of  $t$  seconds for ground-based observations is

$$\sigma_g \approx \sigma_A t^{-1/2} \text{ arcsec} \quad (1-1)$$

where the value of  $\sigma_A$  depends on the seeing at the observation site. For the Allegheny Observatory  $\sigma_A = 0.065$ . For observations from space, the photon-noise limit for measurements of the position accuracy is

$$\sigma_s = \frac{\text{Resolution}}{\text{SNR}} \quad (1-2)$$

where SNR is the signal-to-noise ratio given by

$$\text{SNR} = \sqrt{A \eta N t} \quad (1-3)$$

and  $A$  is the collecting area,  $\eta$  the photon efficiency,  $N$  the photon rate from the target object. For an imaging telescope of 1 m diameter and efficiency 0.2 we find for an eleventh magnitude star  $\sigma_s = 10^{-4} / \sqrt{t}$  arcsec - a factor of 600 better than (1-1). A further gain can be obtained by using two apertures with a large baseline separation,  $L \gg D$ , i.e. using interferometry, since the resolution is proportional to  $L^{-1}$  rather than  $D^{-1}$ .

### 1.3 Other Space-Based Systems

There are currently two space-based systems with astrometric capabilities: the Space Telescope (ST), now under construction, and HIPPARCHOS, currently in design. The ST will have an accuracy of about 2 milli-arcseconds, comparable to present ground-based systems. The ST was not specifically designed for astrometry. By contrast, HIPPARCHOS is an astrometric survey instrument which will conduct parallax measurements for a large number of stars ( $10^4$ ) in a relatively short time (2 years). Its expected accuracy is only 1 milli-arcsecond on average. Consequently, there are no current or planned space-based systems with the accuracy proposed for the concepts discussed in this report, namely one micro-arcsecond.

### 1.4 Science Potential

The science utility of the instrument will depend on the number and type of programs carried out, as measured against the total cost. Scoping this utility, we considered (i) the available time budget; (ii) the kind of observations possible for a given level of performance (e.g. relative position accuracy in a standard integration time); and (iii) instrumental and mission-related limitations.

#### 1.4.1 Time Budget

The baseline task is to detect an earth-mass planet in a 5-year orbit around a K5 star 10 parsecs (32 light-years) from the earth. This task requires a stellar reference frame stable to  $10^{-6}$  arcsec. Fig. 1-1 shows the number of stars of magnitude  $m$  in the nominal  $10 \times 10$  arcmin field-of-view (FOV), as a function of galactic latitude. If we assume 5-10 stars are required to establish such a reference frame (this is probably a minimum number), then such stars are typically fainter than 15th magnitude. If in fact all

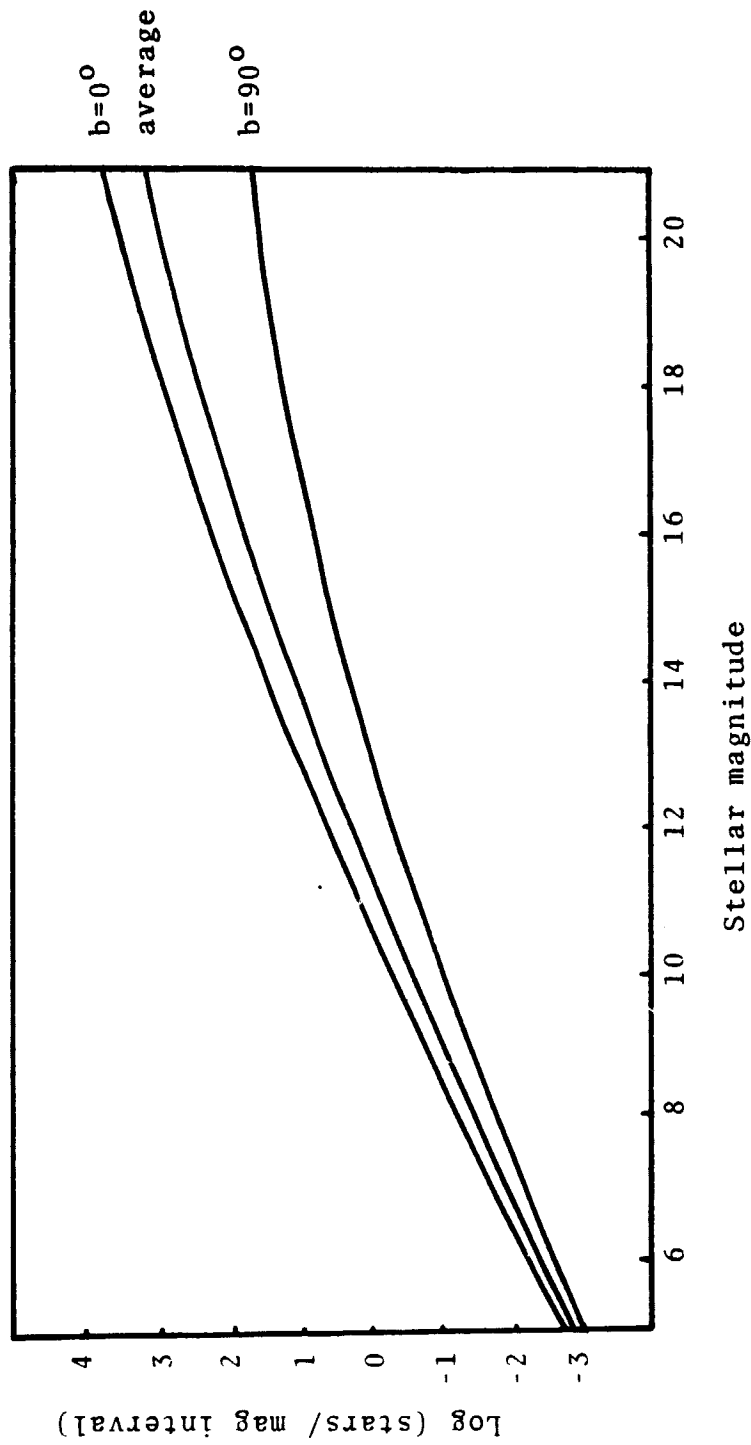


Fig. 1-1 Stars in 10'x10' FOV

stars with  $m \geq 15$  in the FOV are used, then the photon-noise limited integration time for the generally slower of the two instrument concepts, the imaging telescope, is less than  $1/\eta$  hours, where  $\eta$  is the total photon efficiency. It seems unlikely that  $\eta < 0.1$ ; therefore the integration time is 10 hours or less. If we assume that the time during which the FOV of the sensor is eclipsed by the earth is lost (some recovery of that time by retargeting for other programs will be possible) the number of usable hours in 5 years is about 26,000. If we further assume that 50 data points on the orbit of the star are required for measurement of the planetary perturbation, each star will require 500 hours. Thus 50 stars could be surveyed in 5 years for the presence of earth-mass companions. For a double-barrel telescope (a concept proposed in Sec. 3) the number would be 100. Thus a relatively large number of stars could be surveyed for the existence of such planets.

Considerably more stars could be surveyed for the presence of massive planets since the required accuracy is much less: the perturbation of the parent star by a planet is

$$\sigma \approx \mu \delta / \Delta \quad (1-4)$$

where  $\mu$  is the planet/star mass ratio,  $\delta$  the star-planet separation (orbit radius), and  $\Delta$  the distance to the star. Table 1-1 shows that at 10 pc the perturbation of a solar-mass star by giant planets is several hundred micro-arcsec. The required reference frame accuracy is therefore only hundreds of micro-arcsec, and the corresponding observation time less than  $10^{-4}$  of that required for detection of earth-mass planets. Thus a vast number of stars can be surveyed for massive planets or other dark companions. This implies that significant statistics on planetary systems can be



TABLE 1-1

PERTURBATION OF SUN IN  $10^{-6}$ ARCSEC BY THE PLANETS  
(as seen from a distance of 10 pc)

Mercury	0.062	Jupiter	500
Venus	0.17	Saturn	274
Earth	0.30	Uranus	83
Mars	0.049	Neptune	160

obtained in 5 years and, in addition, other important programs may also be carried out.

#### 1.4.2 Astrometry Programs

Significant problems in astronomy are addressed by accurate star position measurements. Several candidate programs listed in Table 1-2 show that an important result could be the more precise calibration of key astrophysical parameters. Some of the programs may require a QSO as reference object. About  $10^3$  QSOs are presently catalogued. Assuming a random distribution on the sky there is a chance 1:1000 of having one in a  $10 \times 10$  arcmin FOV. This number is small; however, the number of known QSOs will undoubtedly increase rapidly in the future due to better instrumentation.

Important astrophysical problems which could be addressed with these instruments include the period-luminosity relation and the cluster HR diagram. More speculative endeavours are the more precise measurement of the orbit of Pluto (search for a tenth planet?), parallaxes and secular parallaxes of QSOs, search for black holes by the study of a visible companion, and perhaps gravitational lens objects.

Few of the programs listed in Table 1-2 require a measurement accuracy of  $10^{-6}$  arcsec but a factor 1-100 less, and they are therefore feasible with significantly reduced instrument accuracy.

#### 1.4.3 Limitations

Program limitations arise from the limited spatial resolution of an instrument and from excessively long integration times for a given accuracy.

TABLE 1-2

## SELECTED ASTROMETRY MISSIONS

<u>OBJECT</u>	<u>PARAMETER</u>	<u>ACCURACY</u> ( $10^{-6}$ arcsec)	<u>MAGNITUDE</u>	<u>SCIENCE RETURN</u>
Extrasolar planets Dark companions	Non-linear star motion	1 (terrestrial) 100 (giant)	5-10	Solar system origin Star formation
Stars to 1 kpc	Parallax to 10% Motion to 1 km/s	100 1000	5-20	Milky Way kinematics, dynamics
Close Binaries	Parallax, orbits	100	10	Mass-radius relation, Mass-spectral type relation
Red dwarf, flare stars, Red giants	Light centroid shifts	1-?	?	Star spots, flares, rotation Atmospheric structure
Cepheids, RR Lyrae	Parallax to 5%	?	?	Period-luminosity relation Absolute distance scale
Galactic clusters, 1 kpc	Internal motion, .05 km/s	50	10-20	
Globular clusters, 10 kpc	Parallax to 10% Internal motion to .5 km/s Absolute motion to 10 km/s	10 50 1000	15-20	Evolutionary dispersion near main sequence
Magellanic clouds	Motion to 10 km/s	200	18-20	Kinematics
Dwarf spheroidals	Internal motion to 1 km/s Absolute motion to 10 km/s	5-15 50-150	19	
M31	Motion to 10 km/s Rotation to 10 km/s	15 15	20-25	Kinematics

The resolution of the imaging system is basically limited to the angle  $\lambda/D$ , which is about 0.1 arcsec ( $D=1$  m,  $\lambda=5500$  Å). For an interferometer with baseline  $L$ , the resolution is typically  $\lambda/L$ . Thus where high resolution is required, the interferometer has a significant advantage, e.g. for the study of close binaries for which the telescope resolution may be marginal.

The observation time for a given program depends on the the time required to establish a sufficiently precise reference frame, formed by say  $N$  field stars, and on the precision with which a target star is to be measured against the frame. Typically, the relative precision in the target position is equal to or better than that for the reference frame. Suppose we have a bright target star of magnitude  $M$ , and  $N_m$  (faint) reference stars of magnitude  $m$  each. Establishing the reference frame to an accuracy  $\sigma$  requires the time  $t = t_m/N_m$ , where  $t_m$  is the centroiding time for a star of magnitude  $m$ . Similarly, establishing the target star with the same precision requires the integration time  $t_M$ . The ratio is

$$\frac{\text{time, reference}}{\text{time, target}} = 10^{0.4(m-M)} / N_m \quad (1-5)$$

If, for example,  $m=15$ ,  $M=7$ ,  $N_m=25$  then the ratio is about 70, i.e. it takes much longer to establish the reference frame than measure the target against it. If, on the other hand,  $m \leq M$ , the opposite is true. Consequently, the program time for targets as faint as 18-20 magnitude may be many hours. As an example, for  $M=20$ , the integration time for  $10^{-5}$  arcsec accuracy is 360 hours for the astrometric telescope. A serious question to be asked is whether during such long integration times systematic errors could creep into the measurement which invalidate the (theoretical) assumed basis for calculating the instrument accuracy in the first place.

## 2. BASIC CONSIDERATIONS

### 2.1 Summary

In this chapter we discuss basic issues applicable to both instruments, namely the orbit (Sec. 2.2), straylight (Sec. 2.3), image motions (Sec. 2.4) and structure (Sec. 2.5).

A circular orbit of 325 m.mi. altitude and  $28.5^{\circ}$  inclination is proposed on the basis of orbit life time. Optimization of the orbit requires further study. The discussion of straylight centers on the contamination of weak star images (e.g. reference stars) by a bright FOV star, and on straylight from the sun. As structural material we consider metal-matrix composites now under development optimal. The major effect of star motion is due to velocity aberration and must be taken into account in the data processing since the motion is much larger than the relative position accuracy sought.

### 2.2 Orbit

#### 2.2.1 Selection Considerations

The selection of an appropriate orbit considers

1. the life of the mission
2. the target accessibility
3. communication and data transfer capability
4. the radiation hazard (component life)
5. the thermal/dynamical environment

as well as cost of deployment, service, retrieval and rescue.

The lifetime and decay history of the orbit depends on the ballistic coefficient of the satellite, the initial orbital parameters and on the launch date. The ballistic coefficient is

$$B = 0.5 C_D A/M \quad (2-1)$$

where  $C_D \approx 2$  for most configurations, A the cross-sectional area and M the mass of the satellite. For a given initial altitude, the orbit lifetime is proportional to  $1/B$ . For the two baseline sensors,

$$\begin{aligned} B &= 0.018 \text{ m}^2/\text{kg} \text{ (telescope)} \\ &= 0.021 \text{ m}^2/\text{kg} \text{ (interferometer)} \end{aligned}$$

if the maximum cross-sectional area faces the flight direction. To calculate a minimum orbit altitude, we assume a random orientation of the sensor relative to the orbit direction over the lifetime of the mission. The effective B-values are then smaller by about  $\pi/4$ . Fig. 2-1 shows the anticipated variation of orbit life with launch data and orbit altitude. The variation with launch date reflects the changes in atmospheric conditions over a 11-year solar cycle. The ballistic coefficient for Fig. 2-1 is  $0.01 \text{ m}^2/\text{kg}$ . The orbit life varies by several years, depending on initial altitude. In choosing a minimum altitude, a certain safety factor should be considered. However, as Fig. 2-1 shows the orbit life increases rapidly with altitude above about 300 n.mi. Thus the incremental altitude (to allow for that safety factor) may be rather small.

For a ballistic coefficient of  $0.015 \text{ m}^2/\text{kg}$  characteristic for the astrometric sensors, a 5-year orbit life can be obtained with an initial altitude of about 325 n.mi.

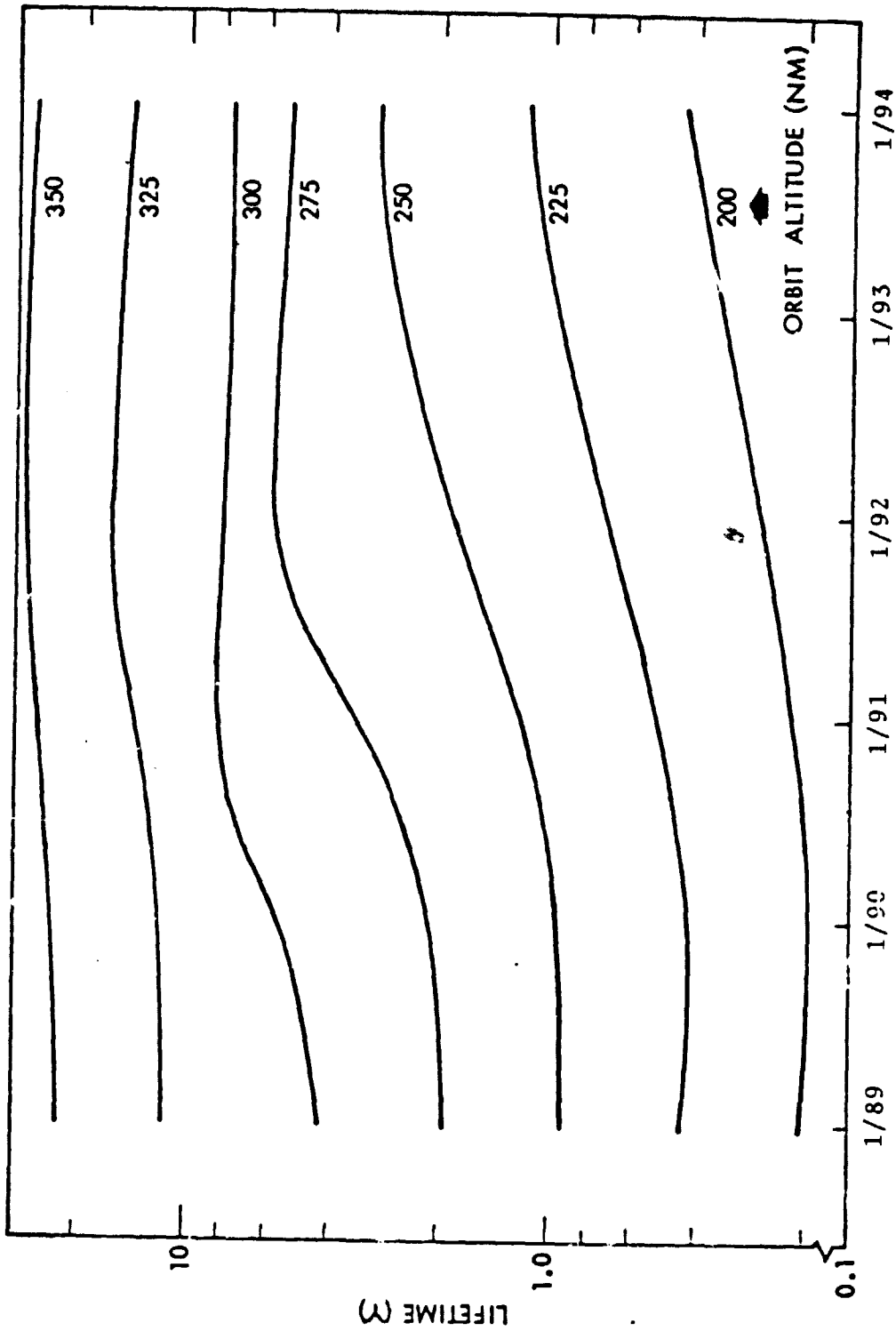


Fig. 2-1 Orbit Lifetime

The target viewing capability depends on orbit properties, time of year, and on requirements for minimum straylight (from sun, earth, moon and other bright objects outside the FOV). The task of determining the accessibility of a target and of scheduling various program missions is complex and outside the scope of this study. Fig 2-2 shows that severe viewing constraints can reduce the accessibility drastically. If no viewing constraints exist then, on average, the target accessibility is 60-70% of the orbit time (typically the fraction of time during which the FOV is not eclipsed by the earth's disk). The fraction will be somewhat larger, if retargeting during FOV eclipse by the earth is carried out. If the sensor is constrained to viewing within the earth's shadow, the target accessibility is only 20-30% (cf. Table 2-1).

The average fractional time of shadow viewing varies with altitude and inclination of the orbit in the manner shown in Fig. 2-3. Decreasing the orbit altitude (from the nominal 325 n.mi.) increases the shadow time slightly. A lower inclination than  $28.5^{\circ}$  would also have more shadow viewing. But the gain in time is rather small, and inclination change is an expensive orbit maneuver (requiring a tug) not recommended here.

Requirements for communication and data transfer to the ground are compatible with the proposed orbit.

The component life is shortened by exposure to high-energy radiation in space. The exposure generally increases with increasing inclination and altitude (Fig. 2-4). At the proposed altitude, some effects can be expected in 5 years, such as glass darkening. Since orbit life increases with increasing altitude, some compromise orbit can be found minimizing radiation damage and maximizing lifetime.



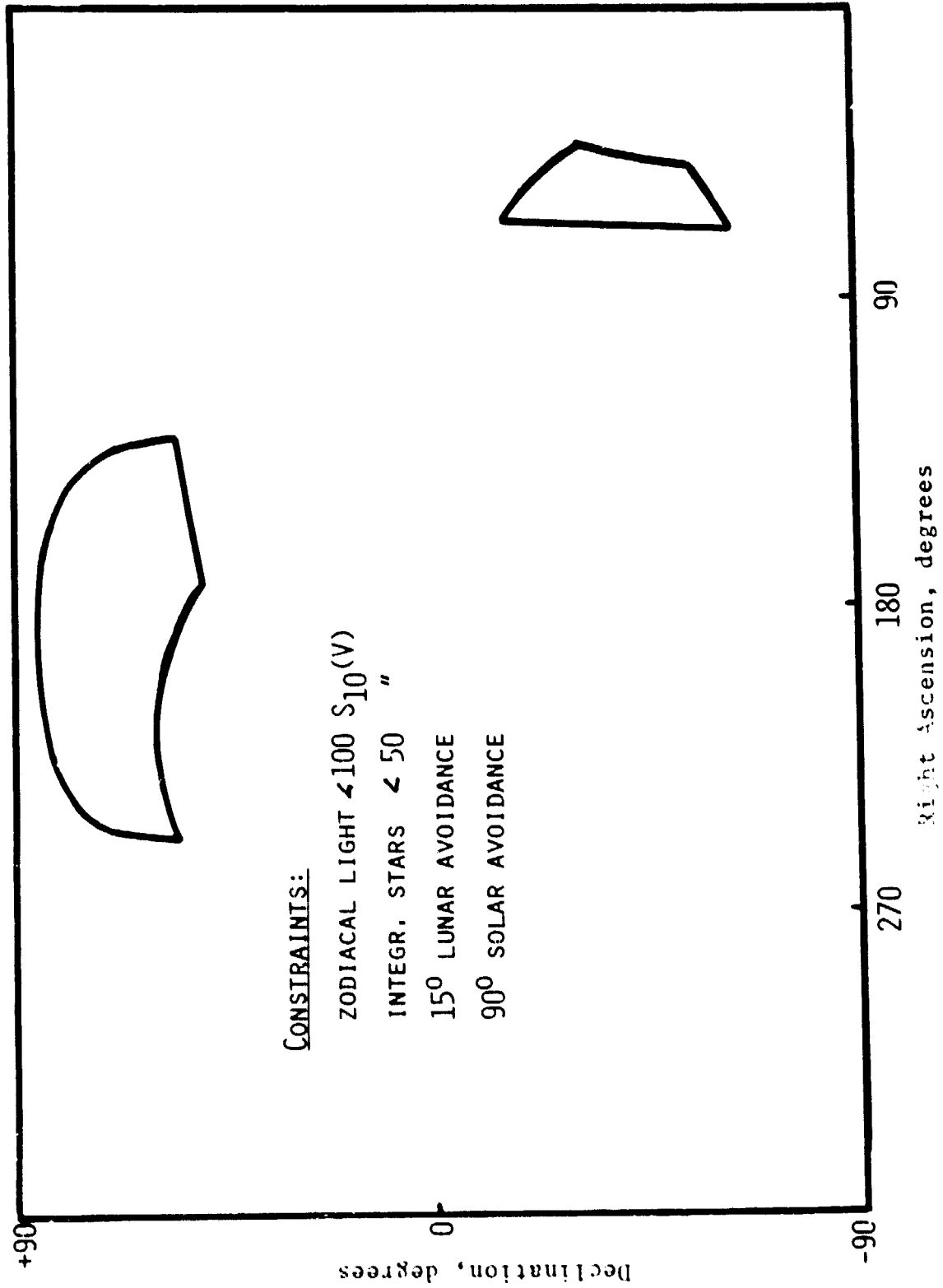


Fig. 2-2 Target accessibility (example)

TABLE 2-1  
ORBIT INCLINATION VS. TARGET ACCESSIBILITY

<u>Target Region</u>	<u>Percent Viewing Time During Year</u>			
	unconstrained (shadow)			<u>i=90</u>
	<u>i=0</u>	<u>i=28.5</u>	<u>i=62.5</u>	
Galactic poles	63 (22)	64 (22)	69 (19)	61-72 (17-22)
Central Milky Way	63 (22)	64 (22)	69 (19)	61-72 (17-22)
Planets	62 (22)	63 (22)	68 (19)	61-99 (15-28)
LMC, SMC	100 (36)	77 (27)	63 (19)	62 (18)

ORIGINAL PAGE IS  
OF POOR QUALITY

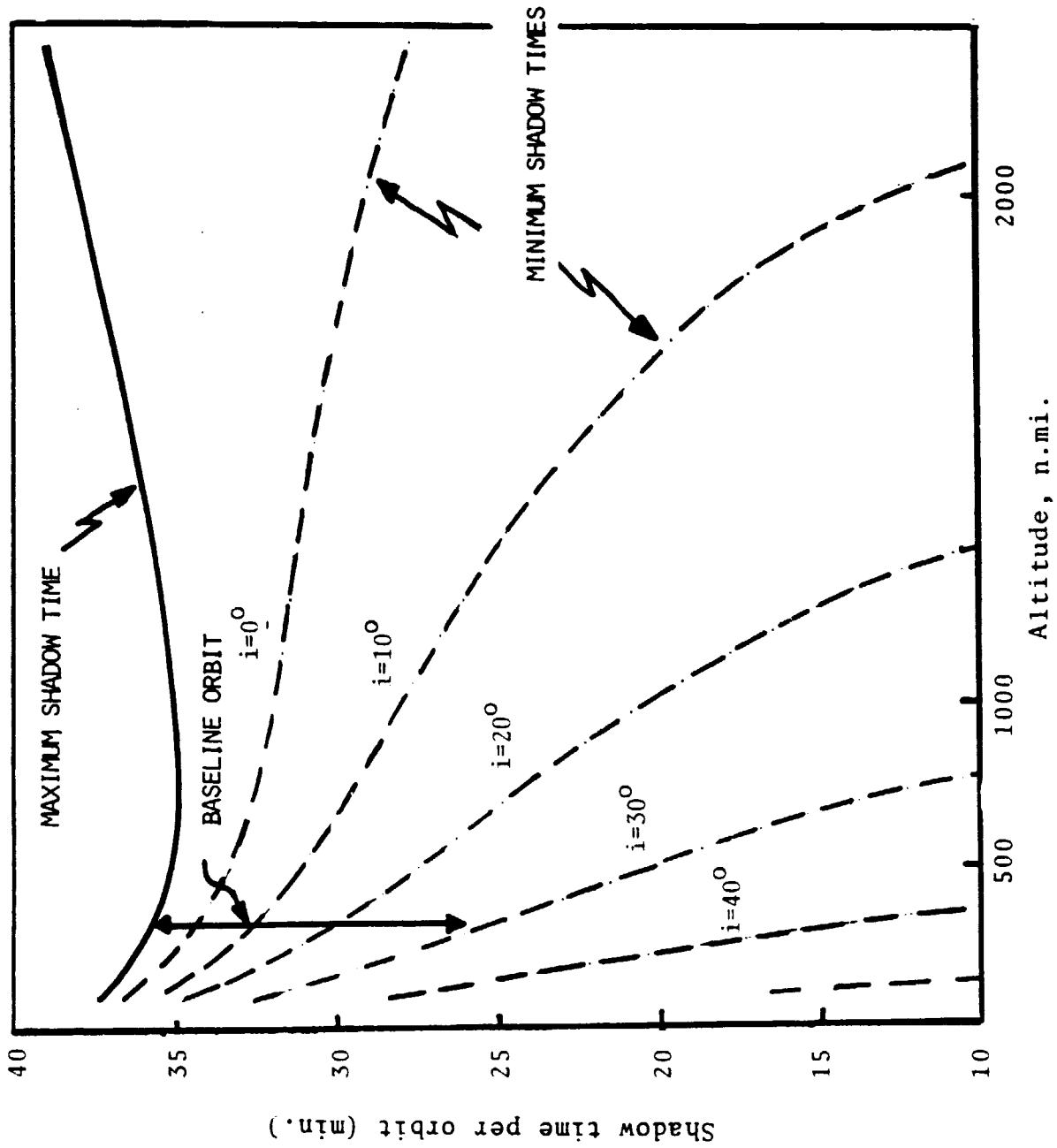


Fig. 2-3 Shadow Time

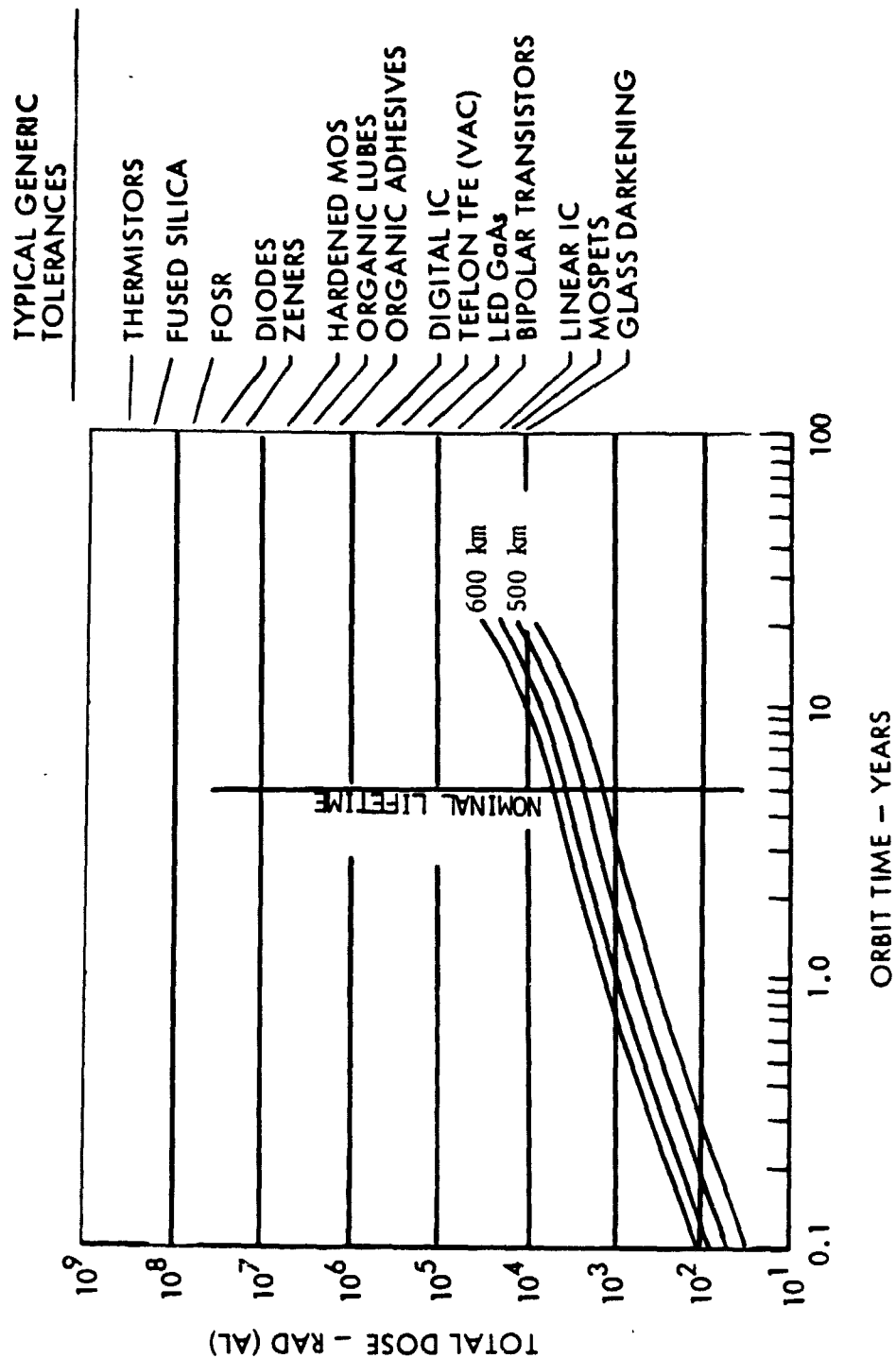


Fig. 2-4 Radiation Effects

The thermal and dynamical environment of a low-altitude orbit is characterized by large spatial and temporal gradients. The thermal gradients can be reduced by shielding (multilayer insulation) and selective heating. The gravity gradient torques can be reduced by designing the satellite's inertia ellipsoid to be either nearly spherical or with the major axis pointed vertically. Both solutions in general incur weight penalties. The alternative, suggested here, is to live with the gradients and provide sufficient torquing capability from the spacecraft.

### 2.2.2 On-Orbit Torques

Solar radiation pressure, aerodynamic drag, and gravity-gradient and cross-orbit torques tend to rotate the sensor system about its center of mass. By far the largest effect is due to gravity-gradient and cross-orbit torques.

(i) An upper limit to the solar radiation pressure torque is  $2rAE/c$ , where  $r$  the torque arm (CG offset),  $A$  the cross-sectional area of the satellite,  $E=1.4 \text{ kW/m}^2$ , and  $c$  the speed of light. Setting  $A=100 \text{ m}^2$  (solar arrays  $45 \text{ m}^2$ , telescope  $30 \text{ m}^2$ , spacecraft  $25 \text{ m}^2$ ), and  $r=1 \text{ m}$ , we find the torque to be  $5 \times 10^{-4} \text{ N.m}$ .

(ii) At 325 n.mi., the aerodynamic drag is about  $7 \times 10^{-6} \text{ N.m}^{-2}$ ; using similar values for  $A$  and  $r$  we obtain a torque similar to that of radiation pressure.

(iii) Gravity-gradient and cross-orbit torques are substantial on large space systems. The torque is

$$\tau = \frac{3}{2} (I_{11} - I_{33}) \Omega^2 \quad (2-3)$$

where  $I_{11}$  and  $I_{33}$  are the largest and smallest moments of inertia,

$\Omega$  is the orbital angular rate. For the baseline systems,  $(I_{11}-I_{33})$  is of the order of  $5 \times 10^4 \text{ kg.m}^2$ , and  $\Omega = 10^{-3} \text{ rad/s}$ ; hence this torque is of order 0.1 N.m - more than 3 orders of magnitude larger than the other two torques. As a result of the torque, after a time  $t$ , the rotation rate of the vehicle would be

$$\omega \approx \Omega^2 t \text{ [rad/s]} \quad (2-4)$$

and the field (10 arcmin diameter) would drift by in about 1 min. Consequently, the instrument must be guided.

### 2.3 Straylight

Straylight from bright objects in and outside the FOV decrease the SNR and, depending on how non-uniform the distribution is, affect the apparent position of the stars. An exact treatment of this problem awaits a more precise definition of the optical trains and mission scenarios.

#### 2.3.1 Bright Star in FOV

Light from a bright star in the FOV is diffracted and scattered to the image location of faint stars. For simplicity we assume the star to be at the FOV center, of magnitude  $M$ , and a faint reference star of magnitude  $m$  at an angular distance  $\theta$  from the center. We shall compare the photon rates, from the reference star, from the sky background, and the scattered and diffracted light of the bright star, at  $\theta$ .

(i) Photons from field star

The spectral flux from a star of visual magnitude  $m$  is

$$f_{\lambda} = 10^{-0.4m-8.43} [\text{ergs.cm}^{-2}\text{\AA}^{-1}\text{s}^{-1}] \quad (2-6)$$

near 5500  $\text{\AA}$ . For an optical bandpass of 3000  $\text{\AA}$ , the photon rate is

$$\nu_m = 3.1 \times 10^{10-0.4m} [\text{s}^{-1}] \quad (2-7)$$

onto a  $1\text{-m}^2$  aperture. The rate is plotted in Fig. 2-5 against  $m$ . The photon rate onto an Airy disk is approximately

$$R_m = 0.84 \nu_m \quad (2-8)$$

(ii) Sky Background

The diffuse sky background consists of zodiacal light, integrated starlight, and diffuse galactic light. The sky brightness is commonly expressed in units of equivalent brightness of 10th (vis) magnitude stars per square degree,  $S_{10}(\text{V})$

$$1 S_{10}(\text{V}) = 3 \times 10^6 \text{ photons.m}^{-2}\text{s}^{-1}\text{deg}^{-2} \quad (2-9)$$

for an optical bandpass 4000-7000  $\text{\AA}$ . The photon rate on an Airy disk is

$$\begin{aligned} \nu_b &= 3 \times 10^6 \left( \frac{2.44 \lambda}{D} \right)^2 \frac{\pi}{4} \left( \frac{180}{\pi} \right)^2 [\text{s}^{-1}] \\ &= 0.014 D^{-2} [\text{s}^{-1}] \end{aligned} \quad (2-10)$$

where  $D$  is in meters.

The zodiacal light is sunlight scattered by interplanetary dust;

ORIGINAL PAGE IS  
OF POOR QUALITY

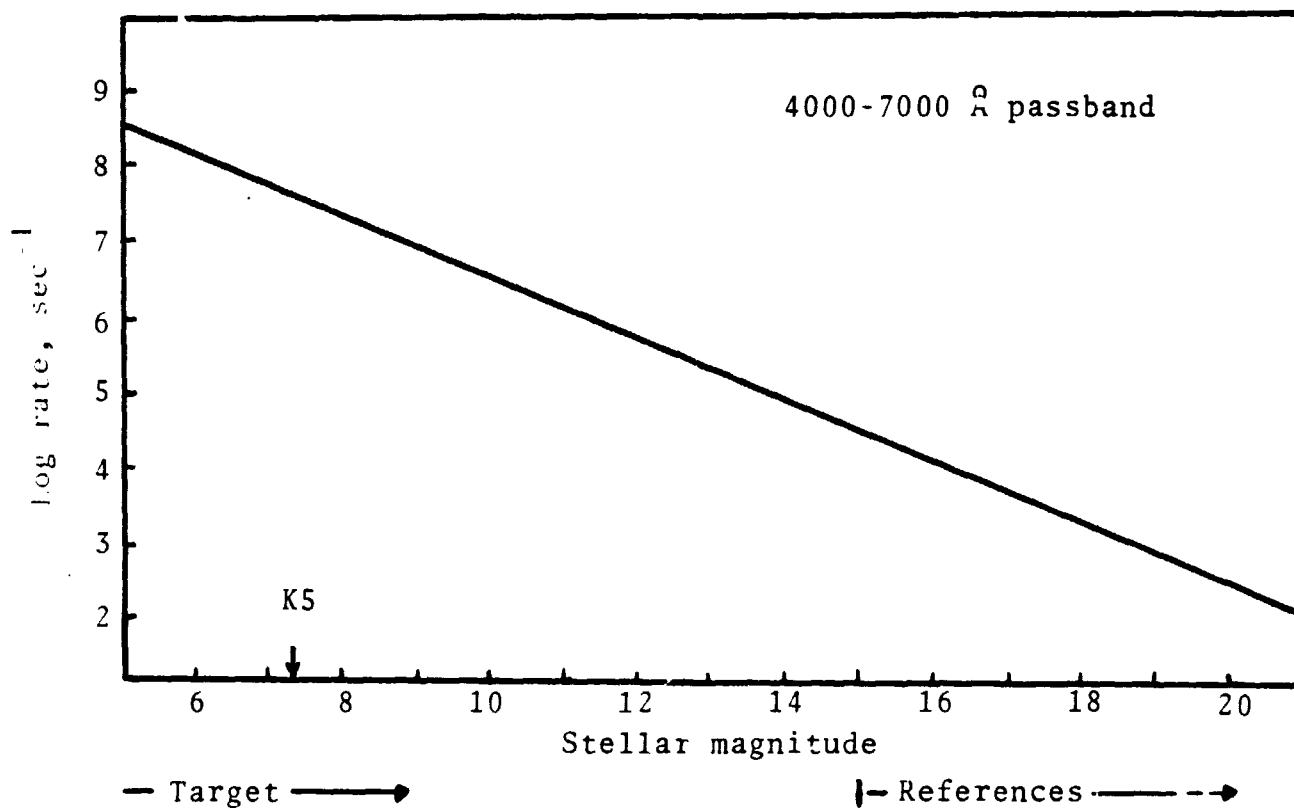


Fig. 2-5 Photon rate to 1 m<sup>2</sup>



which is minimum in the anti-solar direction, about  $80 S_{10}(V)$  and increases with decreasing solar elongation in a manner shown in Fig. 2-6. The integrated starlight is light of unresolved stars. Usually all stars dimmer than 6th magnitude are included, whereas we shall include only stars dimmer than 15th magnitude, since we assume that 15th magnitude stars may serve as reference frame stars. The total brightness of stars with  $m > 15$  is about  $24 S_{10}(V)$ ; if only 21st magnitude stars and fainter are included in the integrated starlight, the brightness is only  $2 S_{10}(V)$ . The diffuse galactic light is starlight scattered by interstellar dust and amounts to about  $20 S_{10}(V)$  in the galactic plane.

The sum of the three backgrounds is thus about  $100 S_{10}(V)$  or greater, depending mainly on solar elongation angle. Therefore

$$R_{\text{sky}} = 1.4 D^{-2} [s^{-1}] \quad (2-11)$$

where the aperture diameter  $D$  is in meters.

(iii) Diffraction of bright star by aperture.

For a circular aperture of diameter  $D$ , the rate of photons to an Airy disk at a distance  $\theta$  is

$$\begin{aligned} R_M &= \nu_M \frac{D^2}{\lambda^2} \left( \frac{\lambda}{\pi D \theta} \right)^3 \left( \frac{2.4 \lambda}{D} \right)^2 \frac{\pi}{4} \\ &= 3.2 \times 10^{-10-0.4M} D^{-3} \theta^{-3} [s^{-1}] \end{aligned} \quad (2-12)$$

(iv) Scattering by Mirror Surface

Microstructure of the mirror surface scatters light of the bright star to the field star at  $\theta$ . The rate is

$$R_S = \nu_M \text{BRDF}(\theta) [s^{-1}] \quad (2-13)$$

where

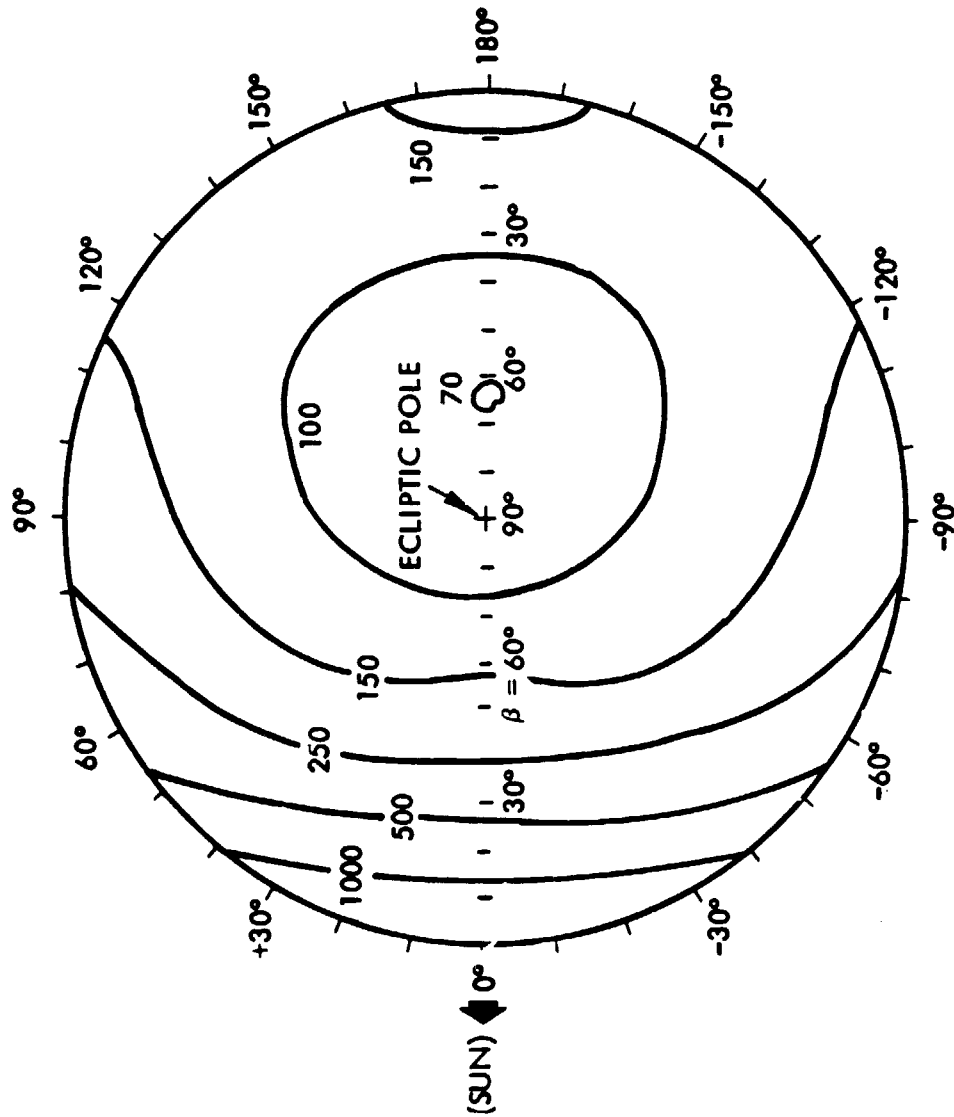


Fig. 2-6 Zodiacal Light brightness contours

$$\text{BRDF}(\theta) = \frac{3 \times 10^{-18}}{\lambda^2} \cdot \frac{\cos^2 \theta}{3.8 \lambda^2 + \sin^2 \theta} \quad [\text{std}^{-1}] \quad (2-14)^*$$

and  $\lambda$  is in meters. Since  $\lambda \ll \theta \ll 1$ , we have  $\text{BRDF}(\theta) \approx 5 \times 10^{-18} / \lambda^2 \theta^2$ .  
Therefore

$$R_S = 4.3 \times 10^{-7-0.4M_D^{-2}\theta^{-2}} \quad [s^{-1}] \quad (2-15)$$

#### (v) Ripple diffraction

Small undulations of the mirror surface, of a coherence length much smaller than the mirror diameter but much larger than for surface roughness, act much like a diffraction grating. If  $a$  is the ripple amplitude,  $\ell$  the coherence length, then the angular position of the first diffraction maximum is at  $\theta = \lambda / \ell$ , and the photon rate, per  $m^2$  aperture area, onto an Airy disk is\*

$$\begin{aligned} R_r &= \nu_M \pi \left( \frac{2.4\pi}{4} \right)^2 \frac{a^2 \ell}{\lambda^2 D} \quad (2-16) \\ &= 6.5 \times 10^{-17-0.4M_a^2\theta^{-1}D^{-1}} \quad [s^{-1}] \end{aligned}$$

#### (vi) Diffraction by FOV obstruction

Obstruction of the FOV by the focal plane and its support causes photon diffraction. Assume a simple rectangular obstruction of length  $D$  and width  $W$ . The diffraction is greatest perpendicular to the orientation of the obstruction, and the photon rate is

---

\* Large Deployable Reflector (LDR), LMSC Final Report, NASA CR-152402 (1980).

$$R_o = v_M \frac{4}{\pi 3 \theta^2} \frac{2.4 \lambda}{D}^2 \frac{\pi}{4} \quad (2-17)$$

$$= 5.7 \times 10^{-3-0.4M} D^{-2} \theta^{-2} \quad [s^{-1}]$$

(vii) Scattering by Dust

If  $dN(a)$  is the number of dust particles per unit area on the primary mirror, with radii between  $a$  and  $(a+da)$ , then

$$R_D = v_M (\pi/\lambda)^2 \int a^4 dN(a) \left( \frac{2.4 \lambda}{D} \right)^2 \frac{\pi}{4} \quad (2-18)$$

Assuming  $dN(a)$  corresponds to a Class 100,000 clean room, the integral in (2-18) is equal to  $7.5 \times 10^{-14} m^2$ . Hence

$$R_D = 0.11 \times 10^{-0.4M} D^{-2} \quad [s^{-1}] \quad (2-19)$$

Table (2-2) summarizes the results from (i)-(vii) and gives the rates in units of the rate from a 21st magnitude star which may be considered a faint reference star, and for  $M=7$  (K5 star at 10 pc). Table 2-2 shows the dependence on  $M$  and on the angle  $\theta$ . Mirror ripple and diffraction by the focal plane are the two largest effects. Suppose that a stellar reference frame is to be established using a all 21st magnitude reference stars in the nominal  $10 \times 10$  arcmin FOV.\* Then there will be several within 1 arcmin distance from the bright star. Fig. 2-7 indicates that straylight from that star can be a serious contaminant for such faint stars.

\* Fig. 1-1 indicates there are about  $10^3$  such stars.

TABLE 2-2

STRAYLIGHT

(Photon rate on Airy disk, units:photons/s)

	Rate	Normalized <sup>*</sup> Rate
Star of magnitude m	$0.88 \times 3.1 \times 10^{10-0.4m}$	1
Minimum Sky	$1.4 D^{-2}$	0.014
Diffraction of star M	$3.2 \times 10^{10-0.4M} D^{-3} \theta^{-3}$	$2.0 \times 10^{-4}$
Mirror scattering "	$4.3 \times 10^{-7-0.4M} D^{-2} \theta^{-2}$	$7.8 \times 10^{-5}$
Mirror ripple "	$6.5 \times 10^{17-0.4M} a^2 \theta^{-1} D^{-1}$	0.31
FOV obstruction "	$5.3 \times 10^{-3-0.4M} D^{-2} \theta^{-2}$	0.96
Dust on Mirror "	$1.1 \times 10^{-0.1-0.4M} D^{-2}$	$1.7 \times 10^{-6}$

<sup>\*</sup> M=7, m=21,  $\theta=1'$ , D=1, a=30Å

ORIGINAL PAGE IS  
OF POOR QUALITY

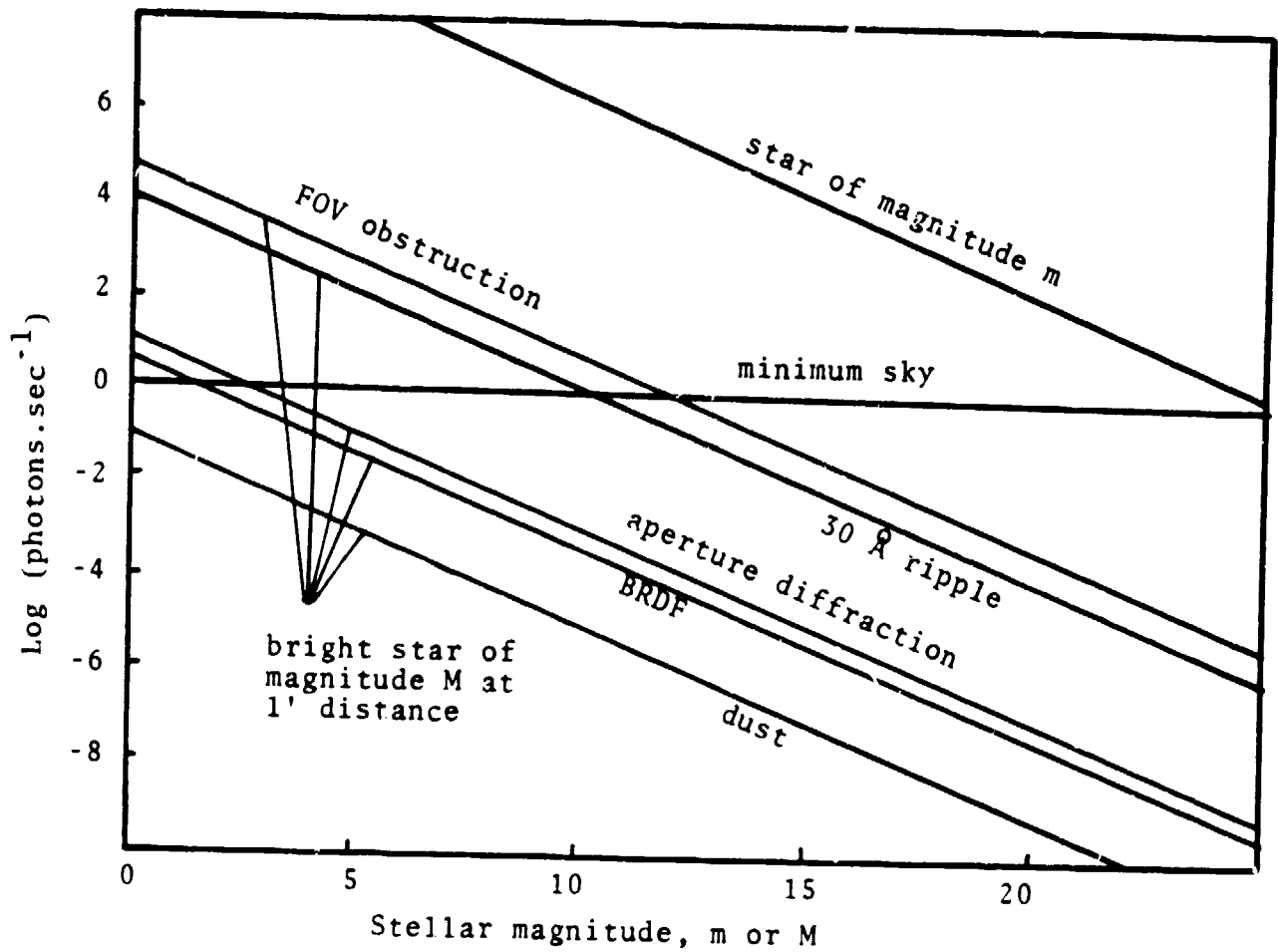


Fig. 2-7 Photons to Airy Disk

ORIGINAL LENSES  
OF POOR QUALITY

### 2.3.1 Straylight from Sun

If the sun is at an elongation less than  $90^\circ$  it partially illuminates the inside of the telescope barrel. Some photons are scattered onto the primary mirror and then to the focal plane. We estimate the effective absorption of photons by the baffles, which is required to keep the solar straylight below the minimum sky brightness. The geometry is shown in Fig. 2-8. The sun-illuminated spot inside the barrel is small compared with the barrel length,  $L$ . The rate of photons to the spot is

$$F_0 = 3.1 \times 10^{10-0.4m_0} (\pi D^2/4) \cos \theta \left[ s^{-1} \right] \quad (2-20)$$

and  $m_0 = -26.74$ , the visual magnitude of the Sun. If the effective photon absorption at the inside of the barrel is  $\beta$ , then  $(\beta F_0 \Omega)$  photons reach the mirror, where  $\Omega$  is solid angle subtended by the mirror at the spot. Since  $D \ll L$ ,  $\Omega = D^2/8L^2$ . To simplify the calculation, assume that the mirror is illuminated uniformly by the solar photons scattered to it. Photons are scattered by the mirror into a unit solar angle at the rate

$$r_0 = \beta F_0 \Omega \bar{S} \quad (2-21)$$

where  $\bar{S}$  is the mirror scattering function (BRDF) averaged over the surface (i.e. over scattering angles  $\phi$ ). Now

$$\bar{S} = \frac{3 \times 10^{-18}}{\lambda^2} \left\langle \frac{\cos^2 \phi}{3.8 \lambda^2 + \sin^2 \phi} \right\rangle_{av} \quad (2-22)$$

$$\approx \frac{4L^2}{D^2} \ln \frac{D/L}{2\sqrt{3.8}\lambda} \quad (2-23)$$

Inserting the result into (2-21) gives

ORIGINAL FILE IS  
OF POOR QUALITY

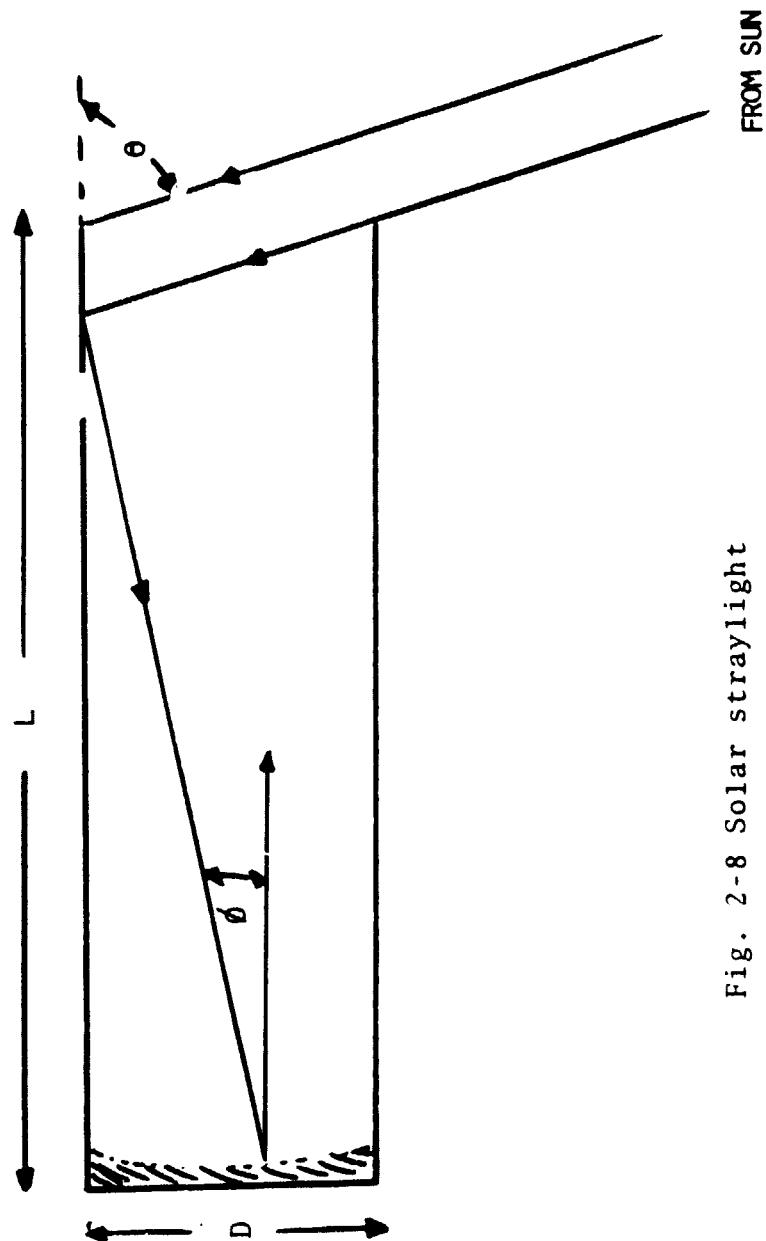


Fig. 2-8 Solar straylight



$$r_o = 0.58 F_o \frac{3 \times 10^{-18}}{\lambda^2} \ln \frac{D/L}{2\sqrt{3.8\lambda}} \quad (2-24)$$

and for the radiance

$$R_o = 7.6 \times 10^{15} \beta \ln \left[ \frac{D/L}{2 \times 10^{-6}} \right] \cos \theta \left[ m^{-2} s^{-1} std^{-1} \right] \quad (2-25)$$

For  $\theta = 60^\circ$  we find  $R_o \approx 5 \times 10^{16} \beta$ . By comparison, the minimum sky is (cf. Sec. 2.3.1(ii)) about  $10^{12} (m^{-2} s^{-1} std^{-1})$ . Thus the effective absorption by the baffles inside the telescope barrel must be better than  $2 \times 10^{-5}$ .

## 2.4 Stellar Image Motions

### 2.4.1 Summary

Stars in the FOV show relative motion because of motion either relative to distant stars or between star and the orbiting satellite. The motion is in some cases much greater than the accuracy of relative star position desired, as Table 2-3 shows.

### 2.4.2 Velocity aberration

Because of the motion of the satellite around the earth (and the earth around the sun) the light from any star is aberrated - a well-known relativistic effect. If the satellite moves toward a field of stars, their angular separation is larger, and if it moves away, smaller than if there were no relative motion. The situation is illustrated in Fig.2-9 with two stars, 1 and 2, and three satellite positions in the orbit, A, B and C. At A, star 2 is shifted toward 1, at C away from 1 by the same amount as at A. At B both images are shifted in the direction of the satellite motion (transverse Doppler effect). If  $\theta$  is the actual angular position of star 1 (measured relative to the direction of satellite motion), then the apparent position is  $\theta'$  where

$$\tan \theta' = \sqrt{1-v^2/c^2} \frac{\sin \theta}{v/c + \cos \theta} \quad (2-26)$$

If  $v=7.5 \text{ km.s}^{-1}$  and the angular separation of the two stars is 10 arcmin, then the shift in position as function of orbit angle is as given in Table 2-4. The maximum relative aberration of the two stars is at  $\theta=0^\circ$  and  $180^\circ$ , about 15,000 micro-arcsec. Therefore, during half an orbit, the relative position of two stars in the FOV can change by as much as 30,000 micro-arcsec.

ORIGINAL PAGE IS  
OF POOR QUALITY

TABLE 2-3  
MOTION OF STARS IN FOV

Cause	Period	Absolute ( $10^{-6}$ s)	Relative
Velocity Aberration	1.5 hr		
Satellite		$1 \times 10^7$	$3 \times 10^4$
Earth	1 yr	$4 \times 10^7$	$1 \times 10^5$
Parallax *			
Satellite	1.5 hr	86/d	similar
Earth	1 yr	$2 \times 10^6$ /d	"
Projection	-	several 100	"
General Relativity			
Earth	1.5 hr	500	$2 \times 10^{-3}$
Sun ( $90^\circ$ El.)	1 yr	8000	$4 \times 10^{-2}$
Star spots	any	cf. Sec. 2.4.6	
Proper motion	-	cf. Sec. 2.4.7	
Multiple systems	any	cf. Sec. 2.4.8	

\*  $d$  = distance in parsecs

ORIGINAL PAGE IS  
OF POOR QUALITY

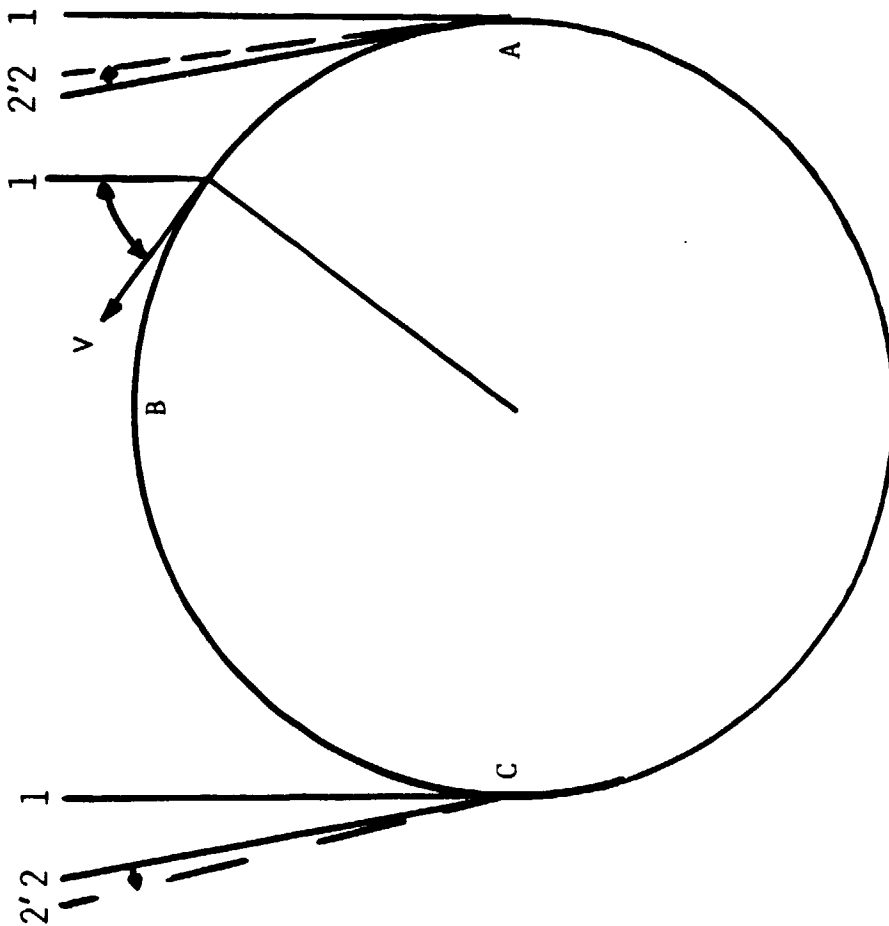


Fig. 2-1. Velocity Aberration

ORIGINAL PAGE IS  
OF POOR QUALITY

LMSC-D870885

TABLE 2-4  
STELLAR ABERRATION  
( $10^{-3}$  deg)

ORBIT POSITION	Star 1	Star 2	Difference
0	0.	-0.004167	0.004167
10	0.238727	0.244622	0.004105
30	0.716182	0.712571	0.003611
50	1.097260	1.094578	0.002682
70	1.345999	1.344568	0.001431
90	1.432390	1.432389	0.000001
110	1.346021	1.347441	-0.001420
130	1.097295	1.099969	-0.002674
150	0.716213	0.719818	-0.003605
170	0.248739	0.252841	-0.004102
180	0.	0.004167	-0.004167

### 2.4.3 Parallax

Because of the motion of the earth about the sun, the position of a star relative to a fixed point (say the direction of the sun's motion) varies by  $2p$  in a year, where  $p$  is the parallax of the star in arcsec. If the star lies in the earth's orbit plane the star's motion is along a straight line, to-and-fro; in general the motion is an ellipse. If one star is 10 pc distant, another  $10^3$  pc, the differential motion between the stars during a year is 0.2 arcsec.

The parallax due to the satellite motion is smaller by the ratio (satellite orbit radius/earth orbit radius)  $= 5 \times 10^{-5}$ .

### 2.4.4 Projection Effect

Although the actual motion of a star (relative to distant stars) may be a straight line, the motion appears accelerated since it is seen by us in projection. Fig. 2-10 shows the star-observer geometry. The angles  $\phi_1$  and  $\phi_2$  are not the same; in fact, using trigonometric relations between the various parameters defined in Fig. 2-10 and the fact that  $\phi_1, \phi_2 \ll 1$ , we find the difference to be approximately equal to  $2\phi_1^2$ . For nearby stars, the annual proper motion is typically a few arcsec. If we let  $\phi_1 = 5$  arcsec, then  $\phi_1 - \phi_2 = 250$  micro-arcsec. For very distant stars such as may be used for a reference frame, say 21st mag stars at 5 kpc, the effect is negligible.

### 2.4.5 Bending of Starlight

Starlight is bent toward the observer by the gravitating earth (and sun as well). Consider Fig. 2-11: If the impact parameter of a star ray is  $r$  and  $M$  the mass of the earth, then the angle is

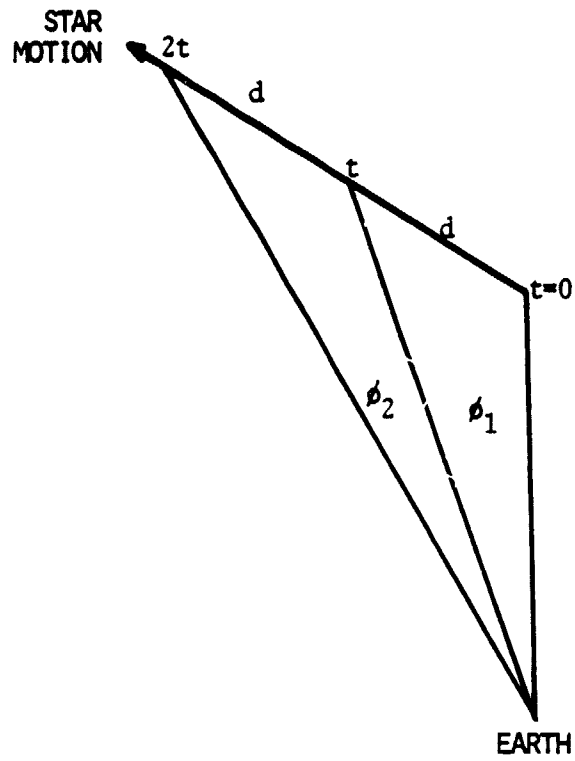


Fig. 2-10 Projection of stellar motion

ORIGINAL PAGE IS  
OF POOR QUALITY

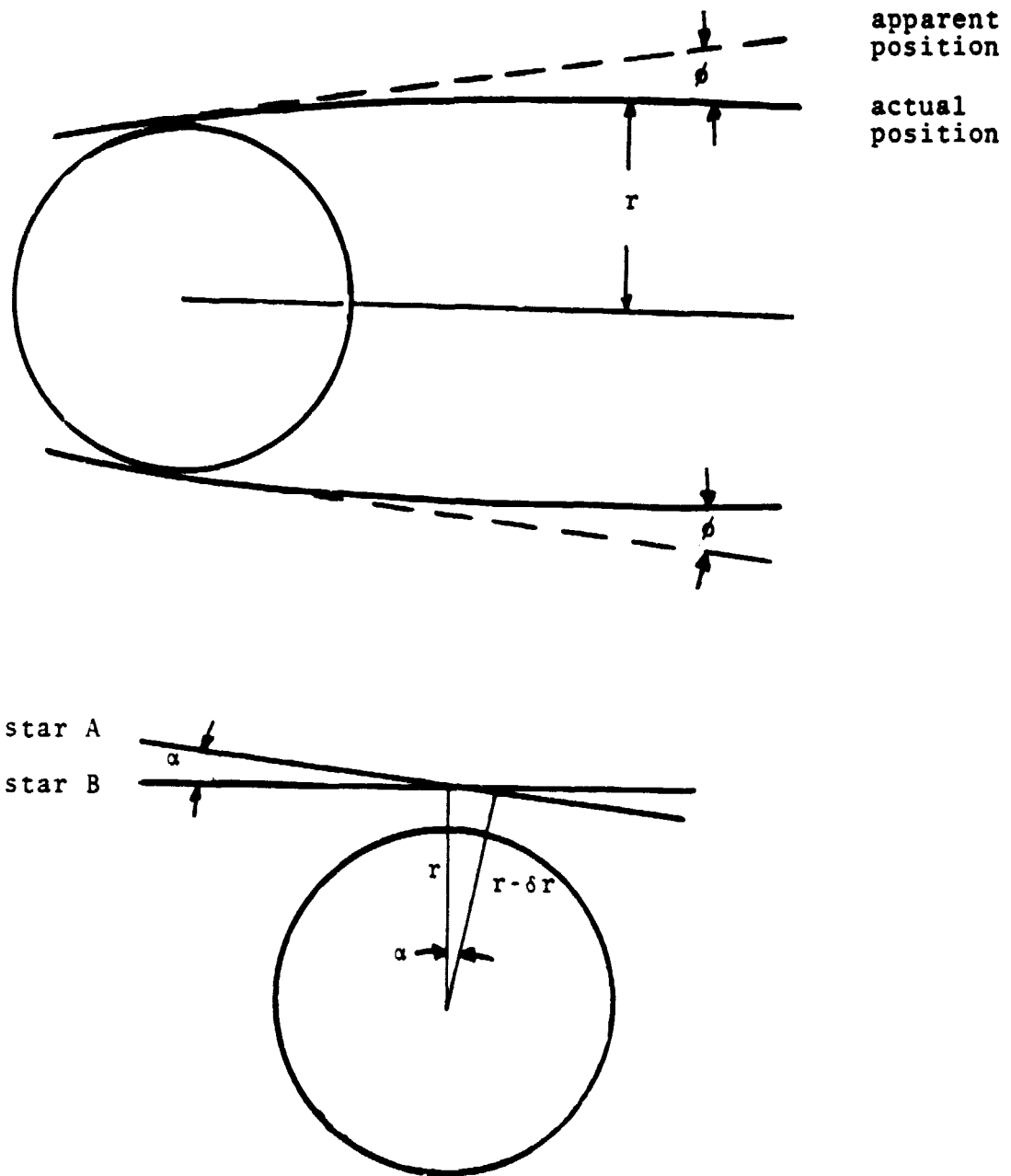


Fig. 2-11 Gravitation deflection of starlight



$$\phi = \frac{2GM}{rc^2} \quad (2-28)$$

Since  $r=R$ ,  $\phi=250 \times 10^{-6}$  arcsec. Therefore, over one satellite orbit, the star position will shift by about  $500 \times 10^{-6}$  arcsec. The shift will be nearly the same for all stars in the FOV, the difference is

$$\delta\phi = \phi \frac{\delta r}{r} \quad (2-28)$$

If two stars are 10' apart, then

$$\frac{r-\delta r}{r} = \cos 10' \quad (2-29)$$

Thus  $\delta r/r=4.2 \times 10^{-6}$ ; this gives

$$\delta\phi=10^{-9} \text{ arcsec} \quad (2-30)$$

The effect by the Sun is about 16 times larger for stars at elongation angles  $90^\circ$ .

#### 2.4.6 Star Spots

Dark regions on a stellar disk will cause a shift in the photometric center. These regions are of a temporary nature and they rotate with the star also. Therefore there will be a continual shifting of the photometric center as the regions wax and wane and the star rotates. Fig. 2-12 represents a stellar disk a dark spot at a distance  $a$  from the center and of diameter  $(2\rho)$ . The photometric center is at a distance  $r$  from the center of the disk, where

ORIGINAL PAGE IS  
OF POOR QUALITY

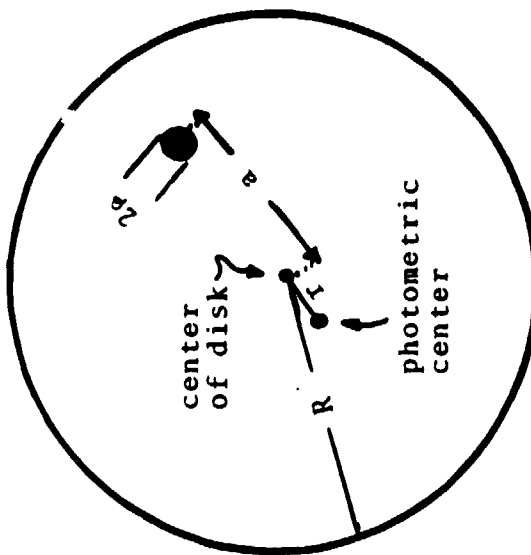


Fig. 2-12 Star Spots

$$r = a_0^2/R^2 \quad (2-31)$$

The barycenter of the earth-sun system is at a distance  $dm/M$  from the center of the sun where  $d=1$  AU,  $m/M$  the earth/sun mass ratio. If this distance were to be equal to  $r$ , then

$$\rho^2/R^2 = (d/a) (m/M) \quad (2-32)$$

If  $a=R$ , then  $\rho/R=1/40$ , and the area of the dark region would be about  $10^{-3}$  of the solar disk. Clearly, dark regions can produce significant shifts of the photometric center - comparable to the gravitational perturbation of a star by a small planet.

#### 2.4.7 Proper Motion

For the first 25 stars in the solar neighborhood, listed by Allen, A.Q.,\* we find the following:

average absolute magnitude 10  
average apparent magnitude 8  
average distance 4.5 pc  
average proper motion  $10/d$ ,  $d$ =distance in pc

If a star with these parameters were at a distance of  $d$  pc, its magnitude would be (disregarding interstellar extinction)

$$m_V = 10 + 5 \log(d_{pc}/10) \quad (2-33)$$

and the proper motion

---

\* Allen, C. W., "Astrophysical Quantities," 3rd Ed., The Athlone Press, 1973

$$\mu = 10^{2-0.2m_v} \text{ arcsec.yr}^{-1} \quad (2-34)$$

Thus an "average" neighborhood star moved to a distance where its apparent magnitude is 15 would have a proper motion of 0.1 arcsec/yr. or  $10^{-5}$  arcsec/hr. The relative motion of stars would be of the same order. Since the integration time calculated for establishing a reference frame to  $10^{-6}$  arcsec from all 15th magnitude stars in the FOV of the astrometric telescope is 10 hours, depending on the total photon efficiency, we see that the relative motion of these stars (due to their proper motion) in the same time is much larger.

#### 2.4.8 Unresolved Double Star

Consider the double star system, Fig. 2-13. The masses of the components are  $M$  and  $m$ , and their respective luminosities  $B$  and  $b$ . The location of the photometric center is at a distance

$$r = (-BQ + bq) / (B + b) \quad (2-35)$$

from the center of mass (C.M.). Since

$$\begin{aligned} q &= aM / (M + m) \\ Q &= am / (M + m) \end{aligned} \quad (2-36)$$

we find

$$r = \left( \frac{M}{M+m} - \frac{B}{B+b} \right) a \quad (2-37)$$

For the example  $\alpha$ Cen,  $M/m=1.24$ ,  $B/b=3.44$ , and  $r/a=0.22$ . Consider now the non-linear component of the motion of the photometric center as the system rotates (Fig. 2-13b). Suppose the center moves over an arclength ( $r\theta$ ) in a certain time  $t$  during which several position measurements are made by the astrometric sensor (probably at equal time intervals). The deviation from a straight

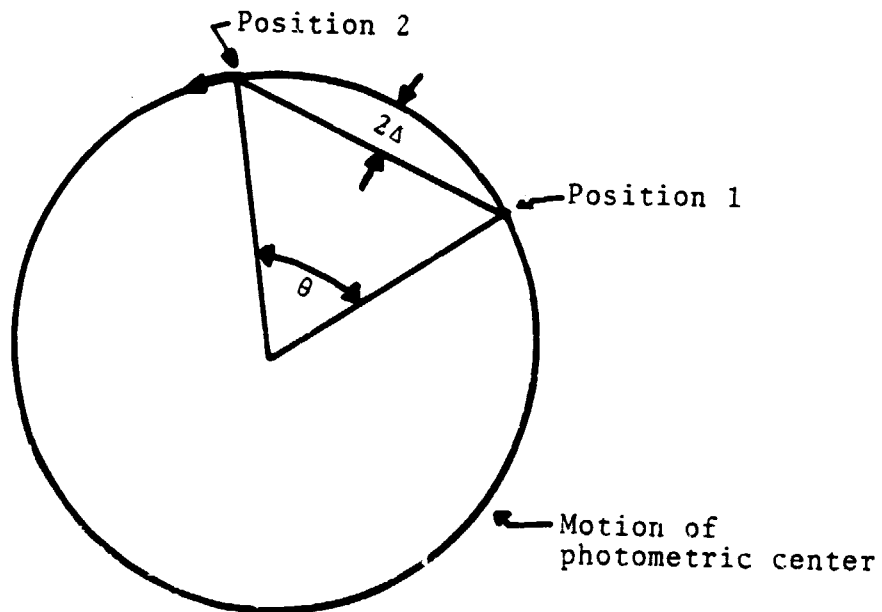
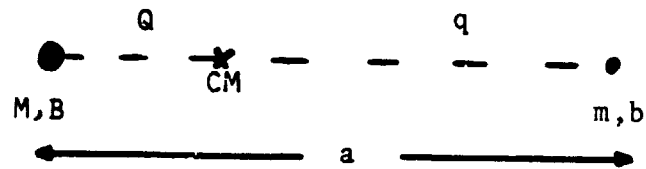


Fig. 2-13 Double Star

line drawn between the first and last position is

$$\Delta = 0.5r (1 - \cos \frac{\theta}{2}) \quad (2-38)$$

Inserting the value of  $r$  from (2-37) and also assuming a random orientation of the orbit relative to us, we have

$$\Delta/a = (\frac{M}{M+m} - \frac{B}{B+b}) \frac{\pi}{8} (1 - \cos \theta) \quad (2-39)$$

Suppose  $\alpha$ Cen were move to a distance where it became a 21st mag system, namely 4700 pc (actual distance 1.34 pc), and suppose that  $\theta$  corresponds to the angle of rotation for a time period of 5 years (orbital period of  $\alpha$ Cen 80 yrs); then  $\theta=0.39$  rad and since  $a=17.6$  arcsec, we find for the deviation of the motion of the photometric center from a straight line the value

$$\begin{aligned} \Delta &= \frac{1.34}{4700} \times 17.6 \times 0.22 \times \frac{\pi}{8} \times 0.019 \text{ arcsec} \quad (2-40) \\ &= 8.2 \times 10^{-6} \text{ arcsec} \end{aligned}$$

The deviation is therefore larger than the nominal reference frame accuracy sought ( $10^{-6}$  arcsec).

#### 2.4.9 Summary

The absolute and relative motion of stars in the FOV exceeds the position accuracy goal of the instruments by orders of magnitude. In trying to determine a star's position relative to others from a limited set of observation over a limited time, it will be challenging in data reduction to account for these motions properly, even linear motions: Black and Scargle\*, for example, recently showed that the period and amplitude of a star's periodic motion can be seriously underestimated by mistakenly absorbing the linear component of the star's motion into its proper motion.

\*"On the Detection of Other Planetary Systems," D.C. Black and J.D. Scargle, NASA/Ames Research Center Astronomy and Astrophysics Preprint (1980)

## 2.5 Structure

### 2.5.1 Deployment

The proposed baseline systems have the maximum dimensions (16.5-m focal length of telescope; 15 m baseline of interferometer) chosen to be near the practical limit for undeployed systems storable in the STS payload bay. The typical diameter of the systems is, by contrast, relatively small compared to the STS payload bay diameter. For greater volume efficiency and for reduction of launch costs, we suggest that both systems have deployable structures. If then only 1/2 or 2/3 of the STS payload bay were used, the launch costs could be shared with other payloads. In fact, our baseline concept designs reflect that intention: the telescope structure is a set of nested cylindrical barrels while the interferometer has a truss design which folds once in the middle. The mechanisms can be so designed that the fully deployed structures, when locked in place, are as rigid as non-deployed ones. A weight and cost penalty is, however, incurred due to additional mechanisms, design complexity and testing requirements.

### 2.5.2 Materials

Requirements for structure materials are high stiffness, low weight, low thermal expansion, known and stable material properties, simple manufacturing techniques and low cost.

Metal matrix composites, like Gr/Al, Gr/Mg, now under development have superior thermal and mechanical properties (Fig. 2-15) but are costly in terms of both, raw material and design and manufacture of structure components. They are generally non-isotropic and it is not yet well known how the properties change with time in a space environment.

Graphite-epoxy is further developed than Gr/metal, is less expensive but also non-isotropic. Furthermore, it suffers from moisture absorption and outgassing.

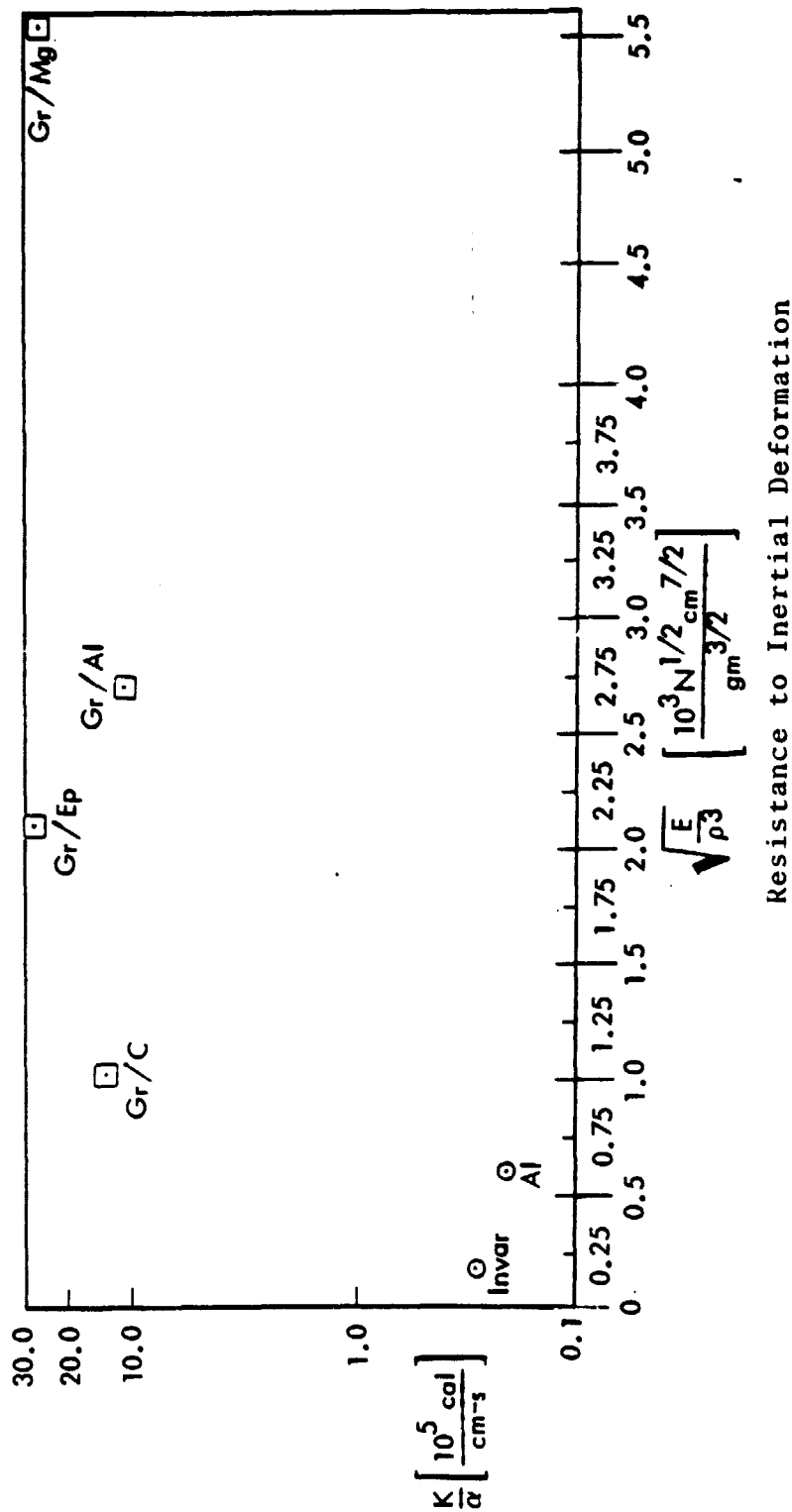


Fig. 2-14 Structure Materials



Metals (aluminum, steel, titanium) are isotropic, with well known characteristics and known long term behavior, having been used in space structures for some time. They are least expensive but the bulk thermal/mechanical properties are poorer than those of the Gr/metals or Gr/Ep (Fig. 2-15). However, moderate size structures can be designed to be stiff and thermally inert.

For the full baseline systems (>15 m overall length) we suggest Gr/AL or Gr/Mg for optimal passive inertial/thermal performance assuming that the manufacturing and design challenges are met in the (yet unspecified) timeframe of the sensors. As a compromise, to save cost, Gr/Ep is suggested. The savings are in the neighborhood of \$10-20M but do not reflect a possible cost penalty deriving from a greater need for more active vibration or thermal control. The cost estimates given for the baseline systems (in Secs. 3 and 4) assume Gr/Ep structures.

### 2.5.3 Vibration Control

Vibration of the structure can introduce random and systematic errors in stellar position measurements. Therefore the vibration sources must be identified and the frequency spectrum and amplitudes characterized. This task requires a rather detailed definition of the sensor system and of the operational scenario, which is not available at this conceptual stage of the system. Potential sources of vibration are

- focal plane motion (i.e. motion of Ronchi ruling in case of the telescope)
- station-keeping devices (e.g. wheels)
- actuators
- any fluid motion (e.g. slushing of propellants)
- microcracks and battery "burbs"

Vibration control methods and devices can be tailored to specific frequency and amplitude domains. Recent studies at Lockheed (ACOSS) indicate that even for very large, flexible and heavy structures active control methods are capable of reducing, for example, line-of-sight excursions (jitter) by many orders of magnitude: One paper study of a 28 m long, 9000 kg, multi-mirror system showed LOS excursion reductions to  $10^{-5}$  arcsec. Laboratory verifications of this capability are, however, quite far from this goal.

#### 2.5.4 Thermal Control

Variations in the thermal load on the structure can cause deformation and result in tilt and piston errors in the optical path. They can be minimized by using materials with high thermal conductivity as well as low coefficient of expansion, i.e. high ratio  $\kappa/\alpha$ . In addition, variations in the thermal soak of structure members can be reduced by wrapping them in multilayer insulation (MLI), silvered on the outside to reflect solar and terrestrial radiation. Spatial temperature gradients can be reduced actively by application of small heat loads along truss members (closed-loop control) and using radiators to transfer excess heat to space. As an example of a combination of passive and active means, the steel and aluminum truss members of the scaled-down telescope concept (Sec. 6) are individually wrapped in MLI and have heaters. The focal plane is assumed radiatively cooled. No need for cryogenics has been identified.

### 3. INTERFEROMETER

#### 3.1 Summary

This chapter describes the principles of operation of the interferometer and the considerations leading to a conceptual baseline design. The baseline system considered here is the 15 meter version of the shearing interferometer suggested and described by Shao<sup>\*</sup> based on his work on earth-based astrometric interferometers. We have used his analysis freely. Three alternate interferometers were also considered by us. One, the modified image plane interferometer, could be important if the beam splitter of the proposed baseline system were to become more troublesome than it presently appears.

The baseline concept has two 0.9-m diameter end mirrors. Four stars are observed simultaneously and share the aperture spatially. Each has its own delay line measuring the relative angular distance between the stars. The system was evaluated for feasibility and technology requirements. The system requires three separate measurement systems: for fringe tracking, for active sampling of the optical path difference (OPD), and for system alignment. There is a trade-off between the optical tolerances required and the OPD sampling fidelity. An optimal, consistent system was not found. The main difficulty lies with the use of gratings on the end mirrors as a metric for the OPD measurement system, and an acceptable alternative to these gratings was not found. A conceptual breakthrough seems required, and the ideas of Reasenberg<sup>\*\*</sup> in this regard should be investigated in future studies. The optical tolerances are tight.

<sup>\*</sup> Shao, M. and Staelin, D. H. "Long-Baseline Optical Interferometer for Astrometry", J. Opt. Soc. Am. 67, 81, 1977, and

Shao, M. and Staelin, D. H. "First Fringe Measurements with a Phase-Tracking Stellar Interferometer", Appl. Opt. 19, 1519, 1980.

<sup>\*\*</sup> Reasenberg, R. D. "Astrometric Instruments in Space", Memorandum to D. C. Black, 9 December 1981

Analysis of the major error sources shows that many errors can be eliminated by star switching i.e. calibration of all four star channels by simultaneous observation of a common bright star. In applications such as planetary detection the target star itself is very bright, and calibration can be accomplished in a few seconds. However, in applications for which all stars in the FOV are dim, the calibration would require a significant period of time (~hours). A larger baseline separation or larger end mirrors are desirable to reduce the integration time. Otherwise, switching must occur within the integration time faster than temporal changes.

The photon-noise limited integration time for the baseline task can be substantially less, or more, than for the astrometric telescope, depending on the required number and magnitude of the reference stars. The proposed concept design assumes sufficiency of four stars, and this sufficiency needs to be established.

An overall system concept design of the satellite was made, and it has the following characteristics. The interferometer structure is a truss design with a rectangular overall shape. The truss folds in the middle on the interferometer optical axis and is hinged from the spacecraft. The structural material is Gr/Ep or Gr/Metal for best thermal/mechanical stability. The required slow rotation about the optical axis can be implemented by either rotation of the satellite as a unit or rotating the interferometer relative to the spacecraft on a spin table with magnetic bearings.

The spacecraft is assumed to be a new design. For a smaller system (scaled-down interferometer) an existing spacecraft such as the MMS may be considered. However, the scaling properties of the interferometer, in terms of feasibility and cost, require more study. Total system weight is 4800 kg, about half of which represents the payload (interferometer). ROM cost in constant 1982 dollars is \$296M for the payload.

### 3.2 Operating Principles

The basic shearing interferometer concept is illustrated in Fig. 3-1. In the top figure the star is on-axis. Two pieces of the wave front, A-A' and B-B', separated by the baseline L are sampled by the interferometer and are overlapped (i.e. sheared) at the lens. If the interferometer is aligned perfectly, the optical path through each arm is equal, and the two overlapped wavefront pieces have the same optical phase at the lens. They interfere constructively and the resulting intensity is measured at the detector in the lens focal plane.

The wavefront from an off-axis star is shown incident on the interferometer in the bottom figure of Fig. 3-1. The star direction is at an angle  $\theta$  with respect to the interferometer axis. Hence, the wavefront piece C-C' is retarded by an amount  $\delta$  at the entrance of the interferometer with respect to the wavefront piece D-D'. Since the interferometer is assumed to be perfectly aligned and the optical path in each arm is the same, the two wavefront pieces are out of phase by the same amount at the lens aperture. The resulting intensity read by the detector is reduced by the factor

$$\frac{1}{2}(1 + \cos \frac{2\pi\delta}{\lambda})$$

where

$$\delta = L \sin \theta \quad (3-1)$$

The intensity at the detector is an indirect measure of the path difference  $\delta$  and hence a measure of the angular position  $\theta$  of the off-axis star. Intensity measurement is, however, not very accurate in practice.

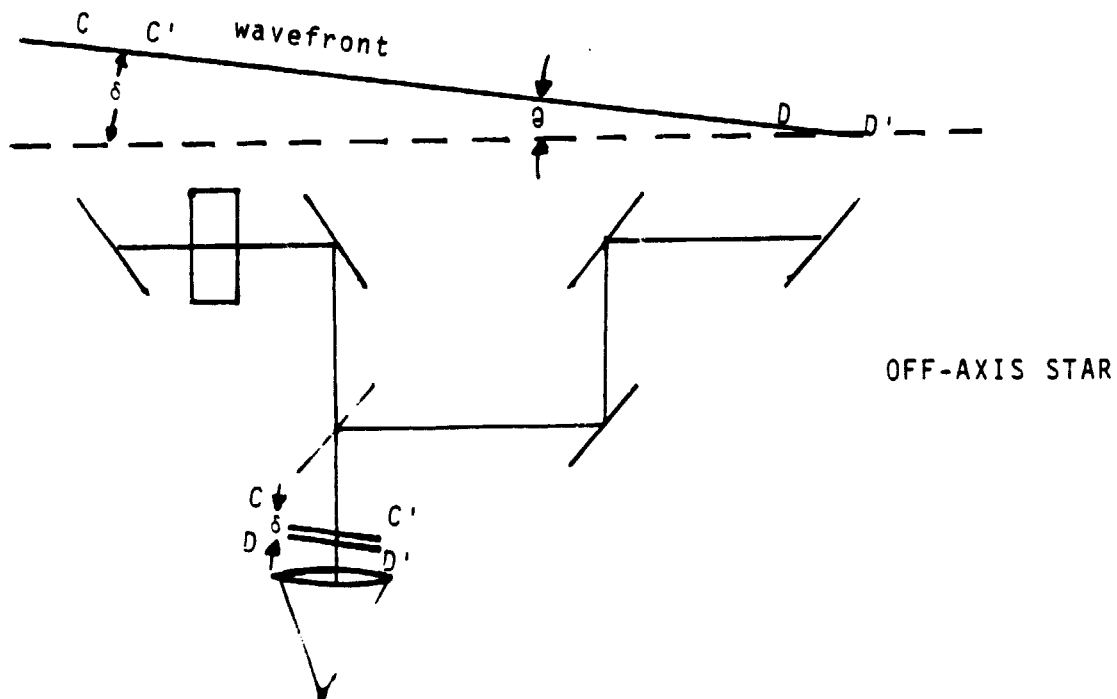
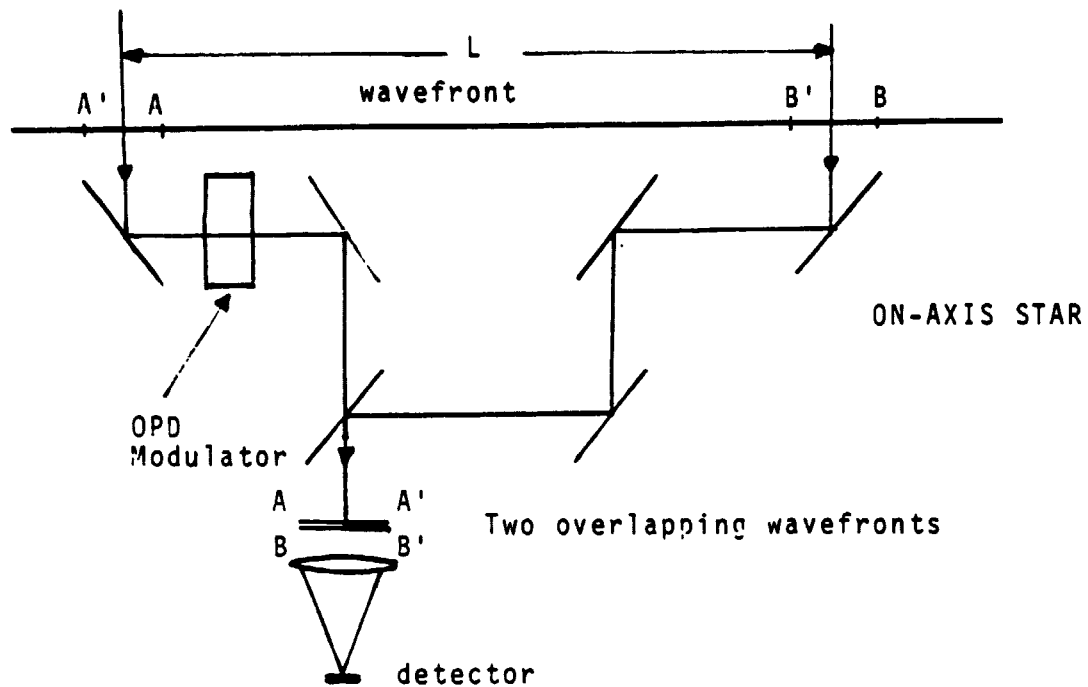


Fig. 3-1 Measurement Technique

The addition of an optical path modulator in one arm of the interferometer, as shown in Fig. 3-1, enables a more direct and more accurate measurement. The modulator changes the optical path by an amount  $M(t)$ , a function of time. Then the intensity from the star at  $\theta$  is

$$I = \frac{1}{2} I_{\max} \left[ 1 + \cos \left( M(t) + \frac{2\pi}{\lambda} L \sin \theta \right) \right] \quad (3-2)$$

Demodulating the cosine term gives the phase  $\frac{2\pi}{\lambda} L \sin \theta$ . Phase measurements are very accurate in practice. The difference in phase between a target star and a reference star gives their relative angular separation in the direction of the shear. Rotating the interferometer can be used to measure separation in several directions.

The system described here has a  $2\pi$  ambiguity. However, after a few  $2\pi$ 's the visibility of the fringes drops due to the limited coherence length of the star light. This depends, of course, on the spectral band pass. Thus there is a trade-off between field of view and number of photons in the chosen pass band. The modulator can have sufficient dynamic range to bring the wavefronts to within the coherence length as Shao and Staelin have done with their fringe acquisition system. Then the modulator, or delay line, position can be measured to give the star position if the fringe phase is nulled. To look at several stars simultaneously requires several delay lines sharing the aperture

Figure 3-2 shows the essential pupil plane astrometric interferometer selected as a baseline. A fringe tracking system closes the loop on the variable delay line setting to keep the central fringe in visible at the detector. A separated delay line is required for each star. A delay line or OPD sensing system monitors the relative delay.

ORIGINAL PAGE IS  
OF POOR QUALITY

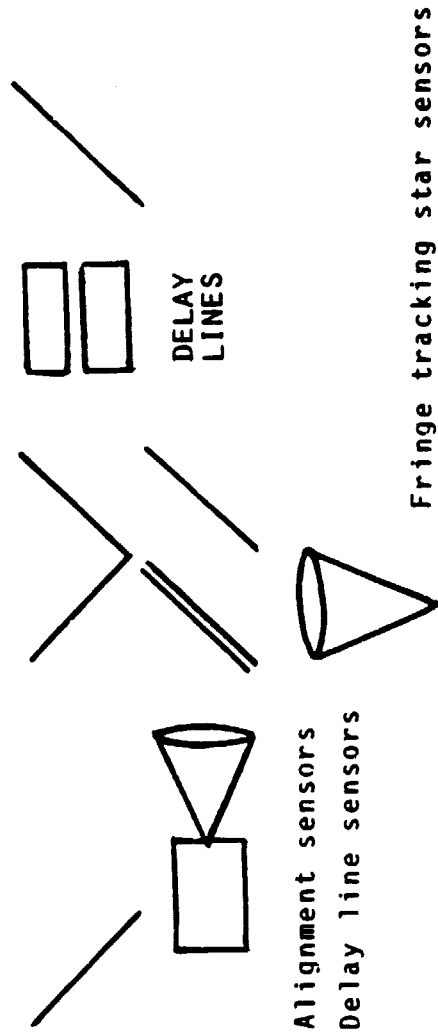


Fig. 3-2 Optical System (schematic)



An alignment system monitors and controls the position and tilt of the interferometer elements.

### 3.3 Requirements and Design Implications

The design goal for the interferometer is 1 micro-arcsec in star position measurement with respect to two or three reference stars. An OPD measurement accuracy of  $0.72 \text{ \AA}$ , or  $\lambda/7600$  ( $\lambda=5500 \text{ \AA}$  central bandpass), is required according to Eq.(3-1). The desired FOV is 10 arcmin, but the size is intimately connected with the alignment errors, and it may be more reasonable to consider a 1' FOV.

A 10' FOV implies that a star might be measured at +5' from the interferometer axis; it will rotate to a position of -5' in one-half rotation period. The OPD will vary from about +2.1 cm to -2.1 cm during the same time. The delay line must track the star over a 4.2 cm total change in OPD. The fringe tracking system must close the loop on the delay line with a resultant accuracy of  $\lambda/10$  within the fringe tracking bandwidth. The error signal is integrated for minutes to hours to achieve  $\lambda/7600$ .

Moving the delay line must produce interference from the star over at least a wave of OPD change in order for the fringe tracking system to lock on. This implies a coherence field of view of

$$\begin{aligned}\theta_c &= \frac{\lambda}{L} = 3.7 \times 10^{-8} \text{ rad} \\ &= 8 \times 10^{-3} \text{ arcsec}\end{aligned}\tag{3-3}$$

Each of the 3 or 4 stars observed over the 10' field will be outside the coherence field of view of the others. This implies that the delay line for each star must be separate, spatially sharing the mirror aperture, or must share the output. We have chosen the spatial

sharing concept in order to maintain simultaneous viewing of at least 3-4 stars. Separate delay lines imply also that separate detectors and optical systems be used for each star. Otherwise the light forming the image of one star could pass through all the delay lines. Then the fringe visibility of each star would be diminished by the non-coherent light passing through delay lines set for other stars.

The coherence FOV of about one wave also limits the spectral bandwidth to about 3000 Å. Thus most of the useful photons from a visible star are imaged on the detector. Note however that this spectral band is not as wide as it can be for the imaging astrometric telescope.

The signal-to-noise ratio (SNR) of unity implies that the phase accuracy of the fringe tracking system is given by

$$\Delta\phi = \frac{1}{V} \frac{\pi}{2} N^{-1/2} \quad [\text{rad rms}] \quad (3-4)$$

where V is the fringe visibility and N the number of photons collected. Since

$$\Delta\theta = \frac{\Delta\phi}{L} \frac{\lambda}{2\pi} \quad (3-5)$$

the angular accuracy in the star position is

$$\theta = 1.1 \times 10^{-6} \frac{1}{LVD} 10^{0.2\pi} \left[ \frac{\lambda}{t n_o n_d} \right]^{1/2} \quad (3-6)$$

where L is the baseline length (separation of the two end mirrors)

$m$  the stellar magnitude,  $\eta_o$  the optical efficiency,  $\eta_d$  the detector quantum efficiency. Here we assumed a spectral bandwidth 4000-7000 Å in calculating the approximate photon flux at earth due to a star of (visible) magnitude  $m$ , the flux being

$$F_m = 3.1 \times 10^{10-0.4m} \text{ [photons/m}^2\text{.s]} \quad (3-7)$$

The integration time  $t$  as a function of star magnitude is shown in Fig. 3-3. For this figure we chose values which we considered reasonable for a  $L=15$  m baseline system, using two large (0.4 m diameter) and two small (0.1 m diameter) subapertures of a full aperture of 0.9-m (Viz. Fig. 3-4); optical efficiency 0.8 and quantum efficiency 0.2 and a fringe visibility of 0.6. One of the subapertures is used by the target star, the other three by reference stars. We assume first that three reference stars are sufficient to establish a stable stellar reference frame against which the motion of the target star is tracked (e.g., the nominal K5, 7th magnitude star suspected for having a terrestrial planet in a 5 year orbit - this requires a reference frame stable to  $10^{-6}$  arcsec). To have at least 3 reference stars in a  $10 \times 10$  arcmin FOV requires (cf. Fig. 1-1) using 13th mag stars. We assume that the target star uses one of the small (0.1 m diameter) subapertures, and the references the other three apertures. Then the required integration time is  $1.3 \times 10^3$  sec. With a bright star in the FOV, as assumed, the star switching for calibration takes very much less time (100 sec). This valuable - perhaps necessary! - technique will not be available if, due to a different mission scenario, there is not such a bright star in the FOV.

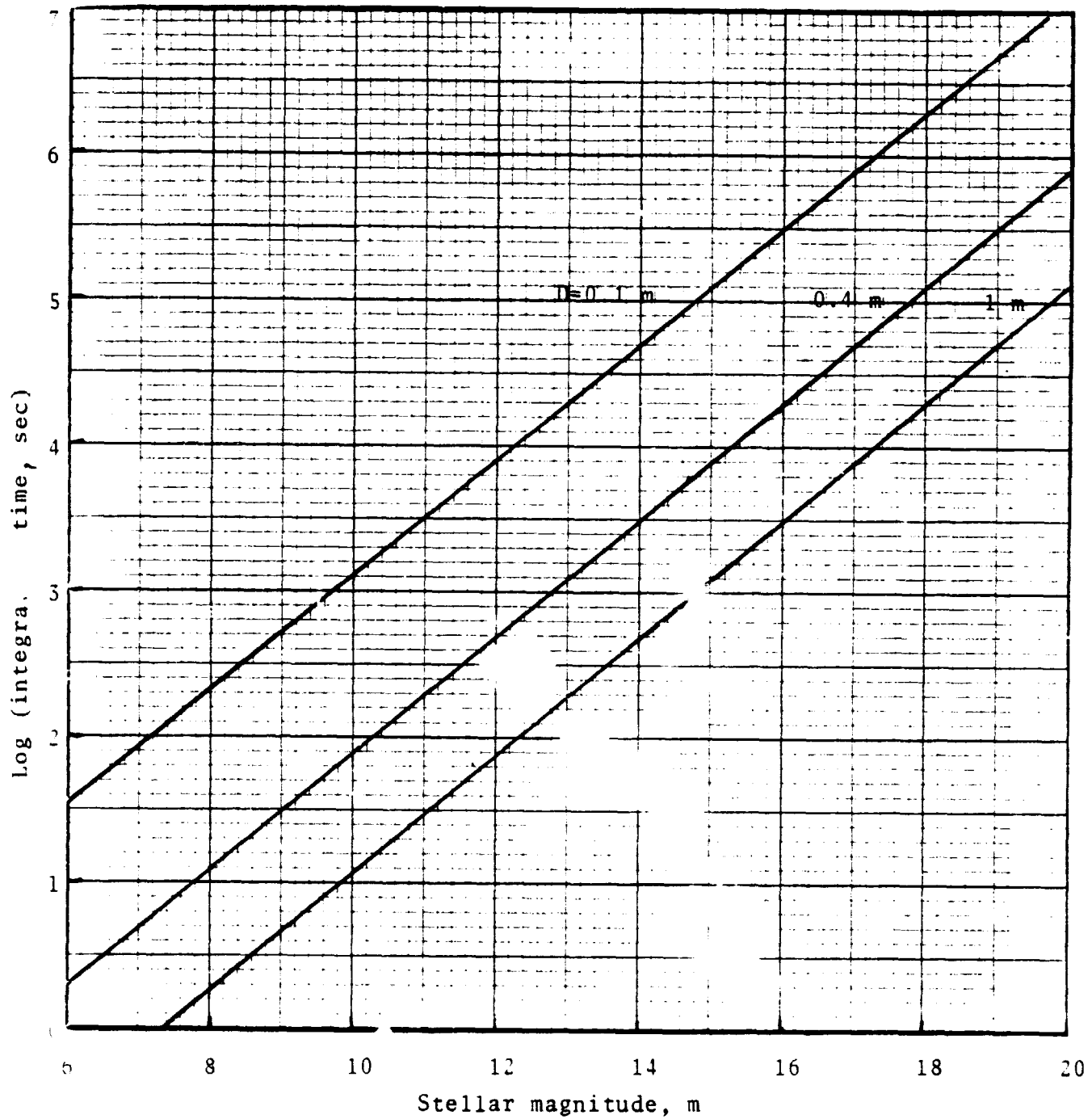


Fig. 3-3 Interferometer integration time

ORIGINAL PAGE IS  
OF POOR QUALITY

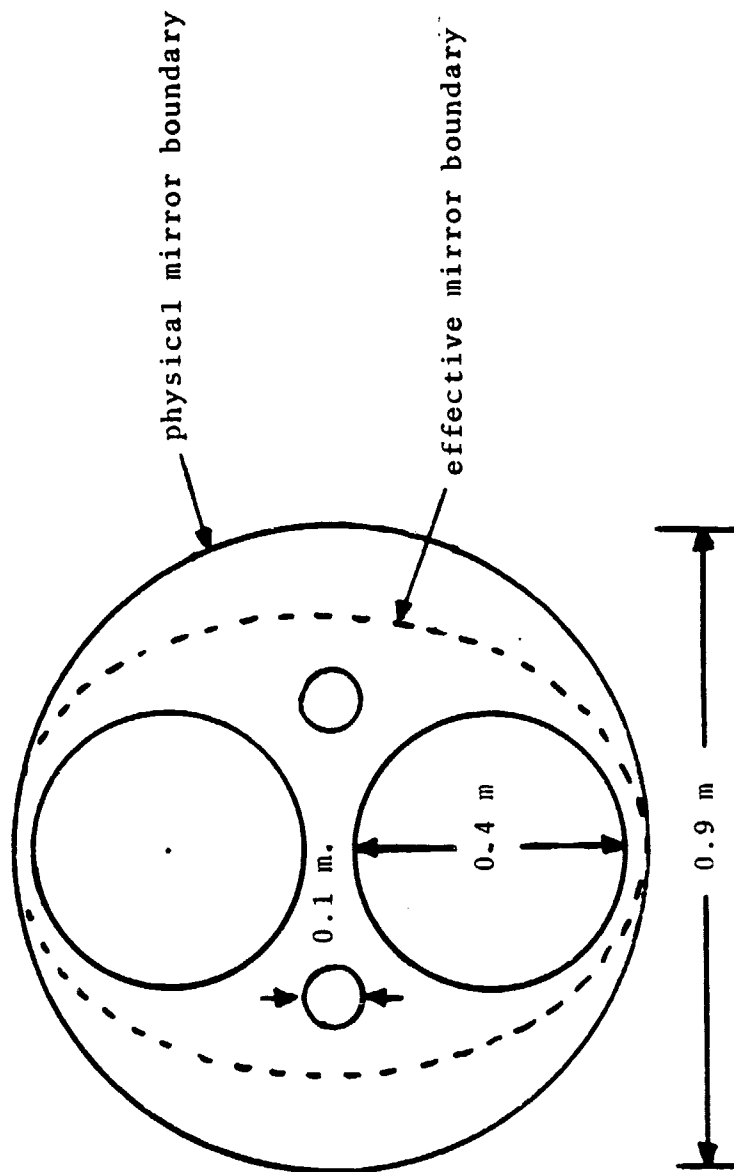


Fig. 3-4 Subaperture Geometry

### 3.4 Alternate Optical Forms

The two types of shearing interferometer which are appropriate for astronomical use have been called pupil plane interferometer and image plane interferometer, respectively. The differences between them are illustrated by Fig. 3-5: For the image plane interferometer, in contrast with the pupil plane interferometer, the interference of the two wavefront pieces occurs in the image plane i.e. the two pupil plane samples are brought together at an angle. This produces tilt fringes in addition to incident angle OPD. The pupil plane interferometer has no tilt fringes, which carry no information on the position of the star. Two versions of each type of interferometer were considered, as listed in Table 3-1. The pupil plane interferometer is the chosen baseline system and is described in Sec. 3.5.

#### Modified Pupil Plane Interferometer

This version uses two afocal telescopes separated by the distance  $L$ . Each telescope acts as a beam expander and demagnifies the pupil samples, relays them to a central beam splitter and then focusses the superimposed beams. The fact that the beams are smaller when they leave the beam expander reduces the fabrication problems for the beam relay and combining optics. The beam splitter in particular is a critical component in terms of size.

This interferometer concept is of particular interest since it was the recommended concept for the Lockheed study of an infrared interferometer for direct detection of extra-solar planets\* (see also Appendix A). A drawing of the system concept involved is shown in Fig. 3-6. The demagnification,  $m$ , of the IRIS beam expander is in the 10-30 range. Now the field of IRIS was very small (a few arcsec). If the FOV were to be expanded to 10 arcmin, as required for the astrometric system, the beam splitter and relay

\*"Systems Level Feasibility Study for the Detection of Extra-Solar Planets, Vol. 1, Infrared Interferometer (IRIS), LMSC-D676424, June 1979.

TABLE 3-1  
OPTICAL FORMS

FORM	PROPERTIES
Pupil Plane Interferometer	Aperture sharing for FOV coverage Fringe track by phase modulation Delay line OPD measurement
Modified Pupil Plane Interferometer	Include beam expander
Image Plane Interferometer	No beam splitter Measure fringe centroid Extended instantaneous FOV
Modified Image Plane Interferometer	Aperture sharing for FOV coverage Fringe track by phase modulation Delay line OPD measurement No beam splitter

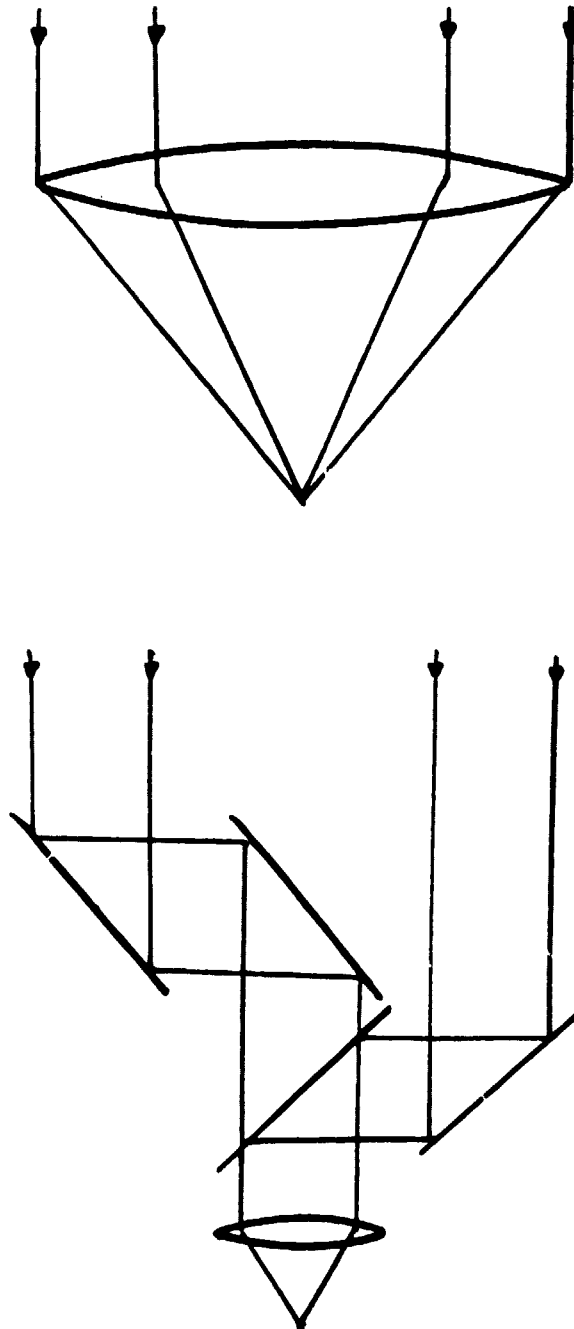
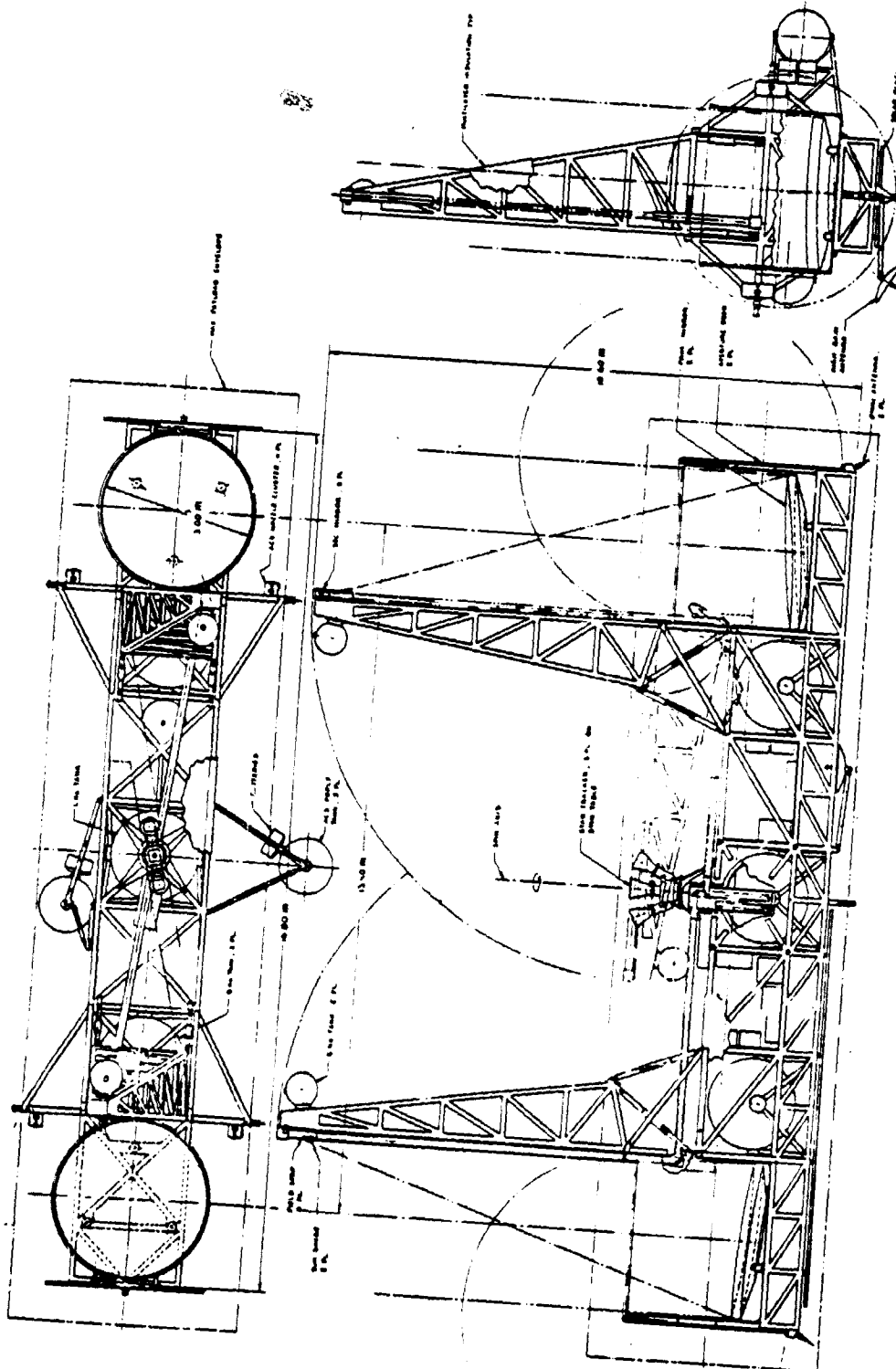


Fig. 3-5 Image Plane Interferometer (top)  
Pupil Plane Interferometer (bottom)



LMSC-D870885



mirror sizes would be compromised as a consequence of the Lagrange invariant; i.e., the apparent field angle is  $m$  times the object space field angle while the exit pupil diameter is reduced by  $m^{-1}$  times the entrance pupil diameter. The clear aperture of the beam splitter required (with no field lens) is approximately as follows:

$$B = (L/2 + F_p D)m \theta + D/m \quad (3-8)$$

$$= .39 \text{ m}$$

where  $D=0.9 \text{ m}$ ,  $m=10$ ,  $F_p=3$  the primary focal ratio, and  $L=15 \text{ m}$ . The result is a reduction in beam splitter size by a factor of about 2, but the price for this advantage is paid in terms of a significant increase in beam expander alignment and in beam walk across the beam splitter as the interferometer rotates.

#### Image Plane Interferometer

The image plane interferometer considered for astrometry is shown in Fig. 3-7. Two mirrors of diameter  $d$ , separated by a distance  $L$ , focus light onto a single focal plane. The image size is assumed to be the diffraction limit of an aperture  $d$ , with fringes separated by an amount which depends only on the angle between the two beams. The position of the central fringe gives the angular position of the star.

The advantage of the image plane interferometer is that the coherence FOV is much larger than for the pupil plane interferometer.

Black showed\* that the coherence FOV is  $8F^2\lambda/d$  and is limited by coma. The disadvantage of this concept is that the SNR is reduced by the factor  $(2d/L)^{1/2}$  compared to a pupil plane interferometer. The integration time is therefore increased by the factor of about  $L/D$ .

\*Black, D. C. "Long-Baseline Interferometers in Space," Informal Document, 1981.

ORIGINAL PAGE IS  
OF POOR QUALITY

LMSC-D870885

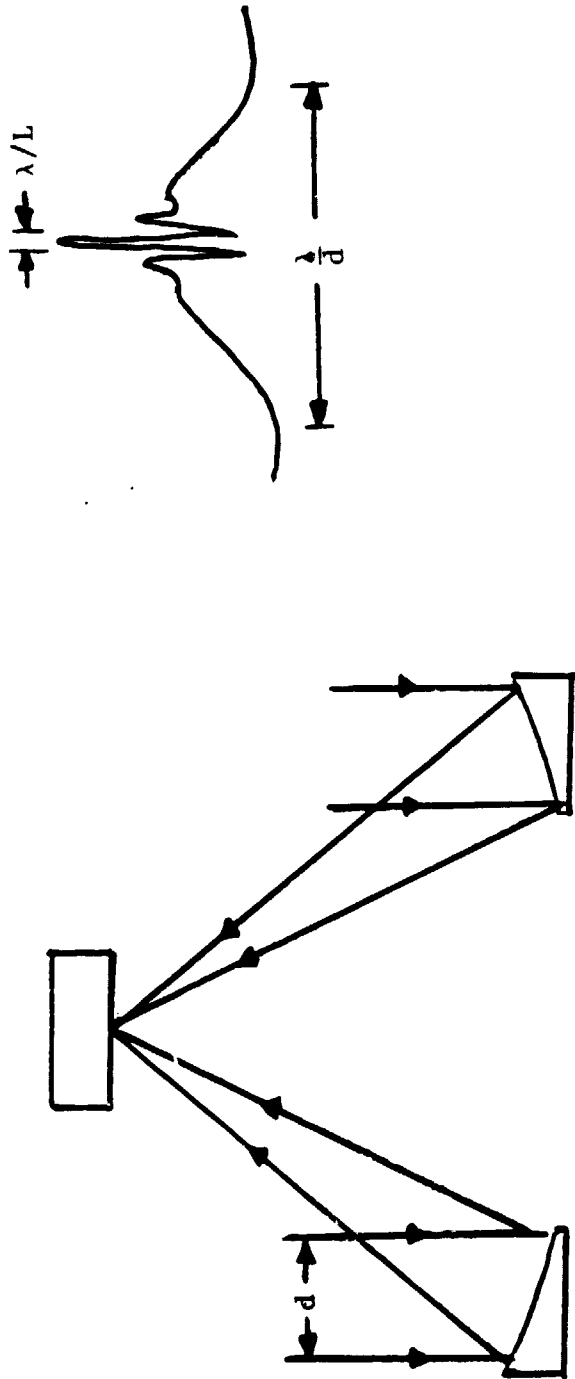


Fig. 3-7 Image Plane Interferometer

TABLE 3-2  
 IMAGE PLANE INTERFEROMETER  
 FOV Implications

f/No.	1	6	19
FOV diameter	1 $\hat{S}$	1 $\widehat{\text{min}}$	10 $\widehat{\text{min}}$
Focal length	15 m	90 m	285 m
Image plane width	0.04 m	0.27 m	0.86 m
Magnification	1	6	19

Table 3-2 shows the FOV implications. For an f/1 system the FOV is only about 1 arcsec, clearly useless for astrometry. The only feasible way of extending the equivalent focal ratio without making the system too big is to use a Cassegrain system. For a 10 arcmin field the equivalent focal length is 285 m; this can be folded with a Cassegrain system but the resulting image plane is too large. The Cassegrain introduces alignment and pupil problems.

It is worth remarking that the image plane interferometer can be regarded as a dilute aperture imaging telescope. In that sense, the distinction between an interferometer and an imaging system is just a matter of semantics.

#### Modified Image Plane Interferometer

The modified image plane interferometer is shown in Fig. 3-8. The two pupil plane samples are separated by a distance  $L$  as before but they are folded before imaging so that the beams are combined with a much smaller angle than for the previous system. Thus the increase in coherence field of view is negligible; this nullifies the advantage of the image plane interferometer as originally conceived, but the advantage seems impractical to achieve. The modified version is much more like a variation of the pupil plane interferometer. It must use a separate delay line for each star and has similar fringe tracking and alignment problems. It does have one considerable potential advantage over the pupil plane interferometer: It requires no beam splitter. The beam splitter is a critical technology item for the pupil plane interferometer. Thus the modified image plane interferometer could be used if the beam splitter requirements prove too demanding. The SNR is reduced by a factor  $(d/2\ell)^{1/2}$  as before but, unlike for the previous image plane interferometer, it is a very small factor.

The image plane analysis is illustrated in Fig. 3-9. The two pupil

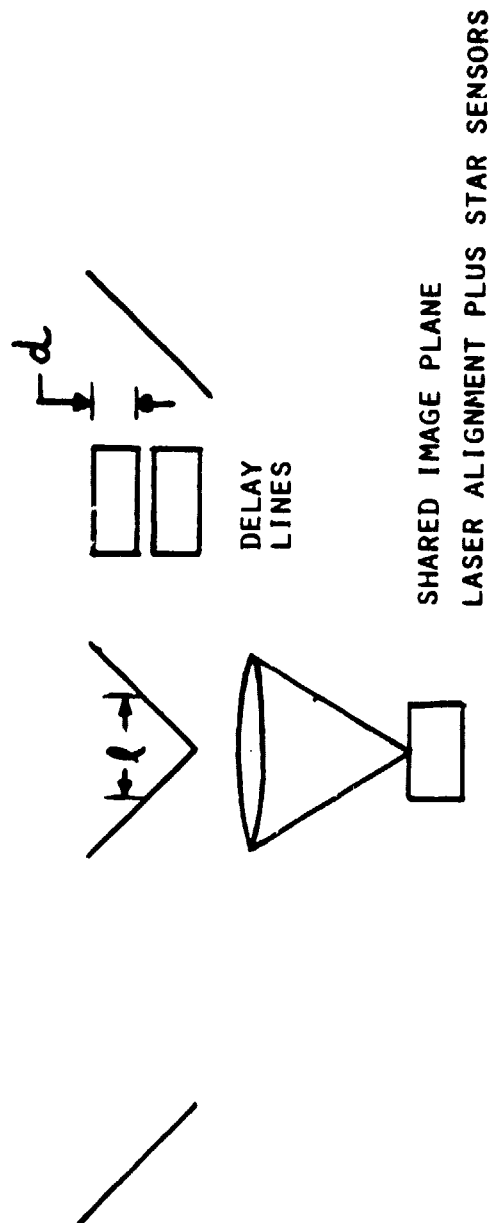


Fig. 3-8 Modified Image Plane Interferometer

plane samples are shown incident at the lens. One is retarded by  $\delta$  in phase with respect to the other, where  $\delta$  is determined by the angular position of the star exactly like the pupil plane interferometer. The pupil function is described as follows:

$$P(x) = A \exp(i \frac{2\pi}{\lambda} \theta x) \exp[i\delta \text{STEP}(x)] \text{rect}(x/2d) \quad (3-9)$$

where  $A$  is the wave amplitude,  $\theta$  the field angle,  $\delta$  the phase step between the two wavefront samples. The special functions are as follows

$$\text{STEP}(x) = \begin{cases} 0, & x < 0 \\ .5, & x = 0 \\ 1, & x > 0 \end{cases} \quad (3-10)$$

and

$$\text{rect}(x) = \begin{cases} 0, & x/2d > 1/2 \\ .5, & x/2d = 1/2 \\ 1, & x/2d < 1/2 \end{cases} \quad (3-11)$$

Note that the linear phase factor  $\exp(i \frac{2\pi}{\lambda} \theta x)$  is too small to be of use in determining  $\theta$ . The useful term is, of course, the step function in the phase.

The image intensity is the modulus squared of the pupil function Fourier transform evaluated at  $\xi = x/\lambda f$ :

$$I(x) = \text{FT} \left\{ P(x) \right\}_{\xi} \quad (3-12)$$

It is easily shown that

$$I(\xi) = \left( \frac{Ad}{\pi \xi} \right)^2 \left[ \sin^2(\delta/2) + 2 \sin(\delta/2) \cdot \sin(2\pi d \xi) + \sin^2(2\pi d \xi - \delta/2) \right] \quad (3-13)$$

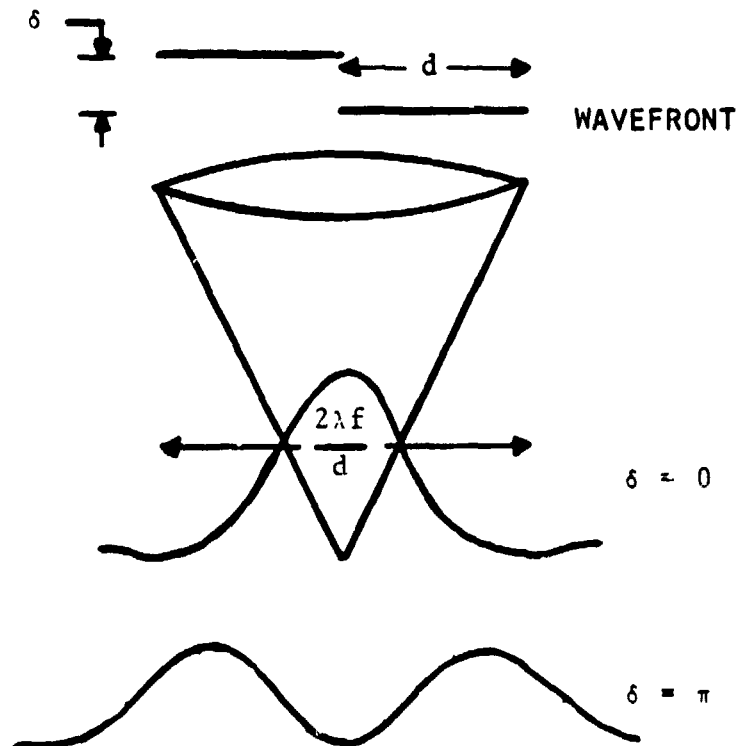


Fig. 3-9 Modified Image Plane Interferometer  
Image Plane Intensity



The image intensity for  $\delta=0$  and  $\delta=\pi$  are shown in Fig. 3-9. When  $\delta=0$ , the star is at  $0^\circ$  with respect to the interferometer axis and the image is essentially diffraction limited:

$$\delta=0 \quad I(\xi) = (4dA)^2 \text{sinc}(2d\xi) \quad (3-14)$$

When the step is a maximum of  $\pi$  then the intensity on the axis is zero:

$$\delta=\pi \quad I(\xi) = \left(\frac{Ad}{\pi\xi}\right)^2 \left[1 + 2 \sin(2\pi d\xi) + \sin^2(2\pi d\xi - \delta/2)\right] \quad (3-15)$$

Fringe tracking can be accomplished by comparing the on-axis intensity with the intensity in the wings.

### 3.5 Baseline

The chosen baseline design is the pupil plane interferometer, with a 15 meter baseline and with the capability of observing 4 stars simultaneously, sharing the aperture. The elements of the system are outlined in this section, including the optical, alignment and OPD measurement systems, the fringe tracking system, and the spacecraft.

Fig. 3-10 shows the overall system schematically. The optical system consists entirely of plane mirrors and refractive elements, from the end mirrors through to the interference plane. These elements have circular symmetry. The end mirrors, shown on the left in Fig. 3-10, are 0.9 m in diameter and ULE flats. The end mirror clear aperture is divided into four subapertures: two dim star 0.4 m diameter circular beams, and two bright star 0.1 m diameter beams. The beam geometry is shown on the right of Fig. 3-11. Note that the end mirrors are tilted  $45^\circ$  with respect to the input beams so that the projected mirror outline and actual beam geometry is as shown on the right of Fig. 3-11. The subapertures are elliptical in their projection on the end mirrors as shown on the left of Fig. 3-10.

ORIGINAL PAGE IS  
OF POOR QUALITY

LASER  
L MEASURE

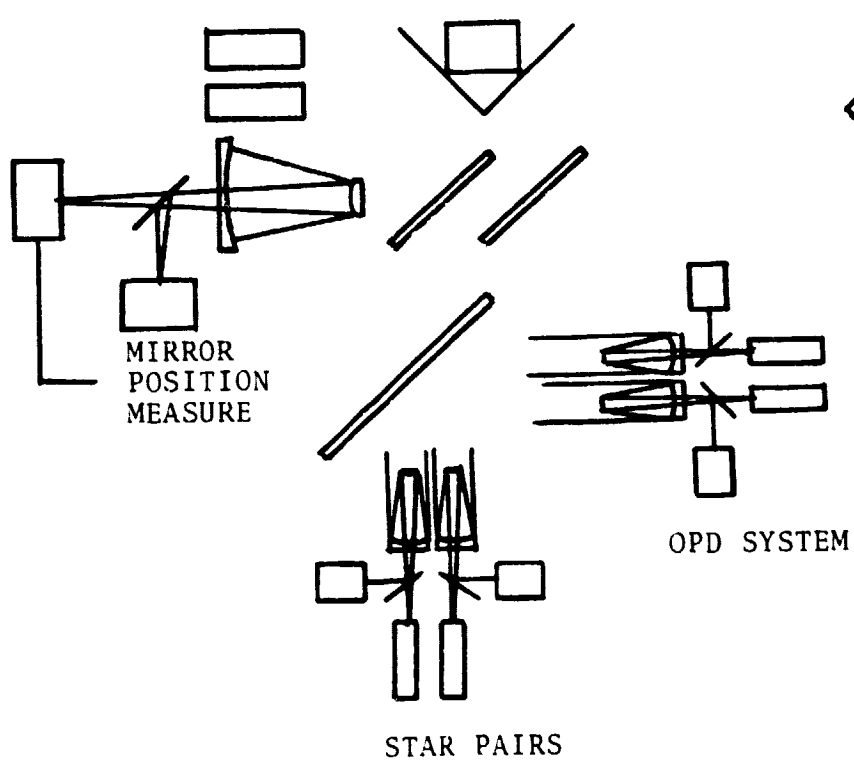


Fig 3-10 Alignment System Overview

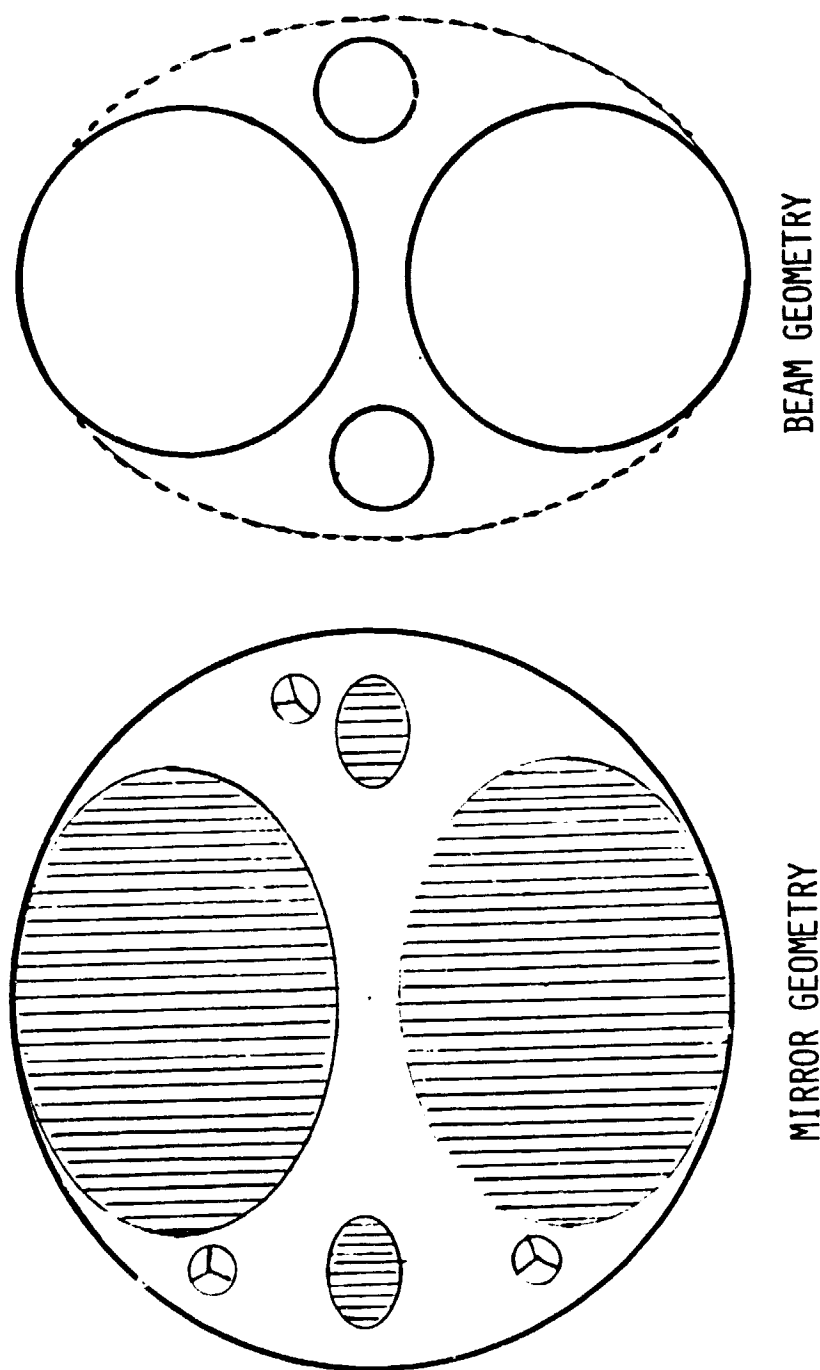


Fig. 3-11 End Mirrors and Beam Geometry

The subaperture areas of the mirrors are overlaid with weak ion etched gratings which are used in the OPD measurement system. The end mirrors also contain inset corner cubes which are used in the end mirror alignment and baseline length measurements.

The optical delay lines are trombone systems as shown in Figure 3-12. There are four independent delay lines, one for each subaperture. The delay line moves on Invar rails driven by a stepper motor, and the alignment system is monitored with an active autocollimator with 1 arcsec accuracy. It is not necessary to measure the delay since the fringe tracking servo is providing the drive signals.

The central "Vee" mirrors match the characteristics of the end mirrors but without the gratings. These two mirrors have a hole in the center through which the end mirrors are monitored. An Optical Position Measuring system (OPS) such as developed by Lockheed\* measures the absolute separation and the relative tilt of the two end mirrors with  $100 \text{ \AA}$  accuracy in  $L$  and better than  $0.1 \text{ \mu rad}$  in angle. The positions of the other elements are monitored from one exit port of the interferometer following the beam splitter.

The other exit port is used by both the fringe tracking star sensors and the OPD measurement system. They must use the same port in order to assure that the path through the beam splitter is the same for both systems. The second beam splitter is dichroic to eliminate photon loss to the star sensors. Note that the fact that this second beam splitter introduces a change in path for the two systems, is not important since it occurs after the interference plane. That is to say, the beams from the two interferometer arms pass through common elements to reach the OPD measurement system

---

\* Gillard, C. W. "Optical Position Sensor Development" Final Report LMSC-D793153, Aug. 1981

ORIGINAL PAGE IS  
OF POOR QUALITY

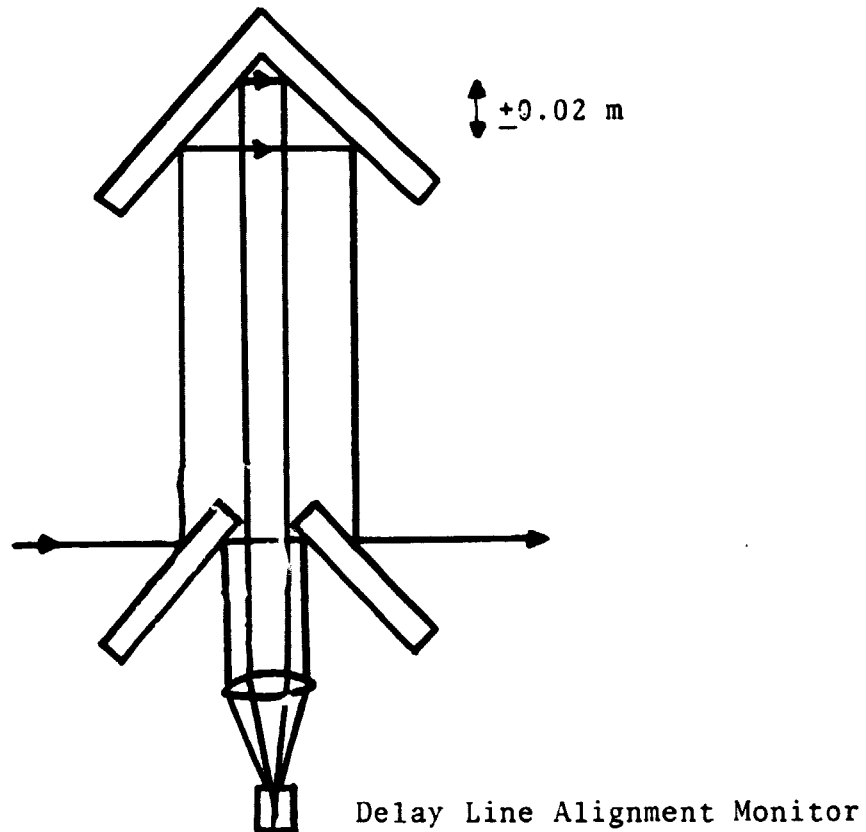


Fig. 3-12 Trombone Optical Delay Line

(after the interference plane) and also pass through different common elements to reach the fringe tracking system. Consequently, the interference of the two systems is both, a function of the OPD between the two arms, and independent of the difference in path a after the interference plane.

The OPD measurement system consists of four independent interferometers. Each interferometer sends a beam through the entire system, including the delay lines, to the gratings on the end mirrors. The gratings reflect the beams back to the interferometers. The two return beams interfere to give the relative OPD between the two arms. The delay lines are dithered to provide an AC signal. The OPD is calibrated by tracking the same bright star with all sensors, and then counting fringes as the sensors are moved to different stars.

The fringe tracking system works as Shao and Staelin have demonstrated (Ref. 2). The sensors each have separate optical systems and separate image dissector tubes. The image dissector tubes track the star, excluding the rest of the field of view. As the delay line sweeps through its range the white light fringe is detected, acquired and tracked with feedback to the delay line.

The procedure for operating the baseline system is as follows:

1. All channels acquire and track the same (brightest) star in the FOV. The OPD is now calibrated.
2. The channels switch to the target and reference stars and
  - search for star fringes with the fringe tracking system;
  - count laser fringes with the OPD system;

- acquire and track star fringes;
- read OPD data and process them for star position.

3. All channels switch to brightest star for re-calibration at various points of a rotation.

### 3.6 Subsystem Analysis

#### 3.6.1 Optical System

The plane mirror system chosen for the baseline design is relatively free from alignment tilt, decenter and z-axis errors that are present in focussing systems. The only powered optics in the system are after the interference plane where the optical path is common to both interfering beams. Reasenberg has suggested an alternative configuration which eliminates two of the mirrors in one arm (Fig. 3-13). There is, without a doubt, a consistent alignment scheme which could be derived from this modified concept, but it would be different from the proposed baseline system.

The optical figure tolerance on the mirrors required for the interferometer and beam splitter are beyond our experience for apertures of this size. Thus the calibration technique is a critical factor. If the OPD system were to sample exactly the same path through the interferometer as the star in question, then optical figure tolerances could be greatly relaxed. That is, if the OPD sample beam were to move and track the star and move accordingly in angle as the instruments rotates, then errors would be quite small. The baseline system, however, uses gratings on the primary to reflect the beam back; with this concept, tracking the star as it moves is not possible and thus the star beam walks across the mirrors as the interferometer rotates while the sample beam remains fixed.

The figure errors on the mirrors can cause both OPD errors and errors

ORIGINAL PAGE IS  
OF POOR QUALITY

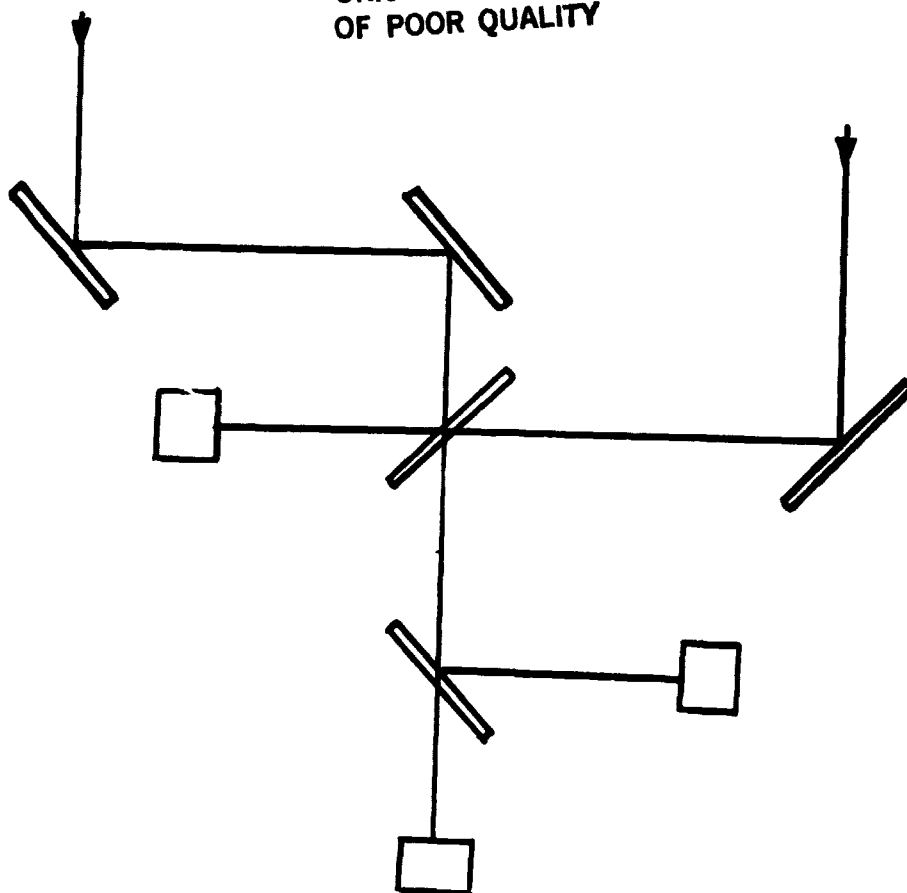


Fig. 3-13 Alternate Optical Configuration



in baseline length,  $L$ . Both can lead to errors in the measured star position but with far different weights. Thus

$$\delta = L \sin \theta \quad (3-1)$$

implies

$$\Delta \theta = \frac{\Delta \delta}{L \cos \theta} - \frac{\delta \Delta L}{L^2 \cos \theta} \quad (3-16)$$

A 1 Å error in  $\delta$  produces a  $10^{-6}$  arcsec error in  $\theta$ ; but it takes 0.06 μm error in  $L$  to produce the same effect at the edge of the FOV.

A static figure error can reduce the fringe visibility but this is negligible for small errors.

The effect on  $\delta$  is given by the average piston error over a subaperture and not by an rms error:

$$\Delta \delta = \frac{\int_0^1 \int_0^{2\pi} w \rho \, d\theta \, d\rho}{\int_0^1 \int_0^{2\pi} \rho \, d\theta \, d\rho} \quad (3-17)$$

where  $w$  = wavefront error is approximately twice the mirror surface error. Fig.3-14 shows a focus error on the wavefront - the most likely error which will occur across a flat. The sag of the wavefront is twice the sag of the mirror. With 4 subapertures it is possible to place all the subaperture centers at the distance  $h_1$  from the vertex. This should tend to minimize the first order piston error due to focus. The residual error is probably too great for an uncalibrated system unless the OPD measurement uses both interferometer arms, as in the baseline system. This is the reason why it is not appropriate to use the OPS in one arm only.

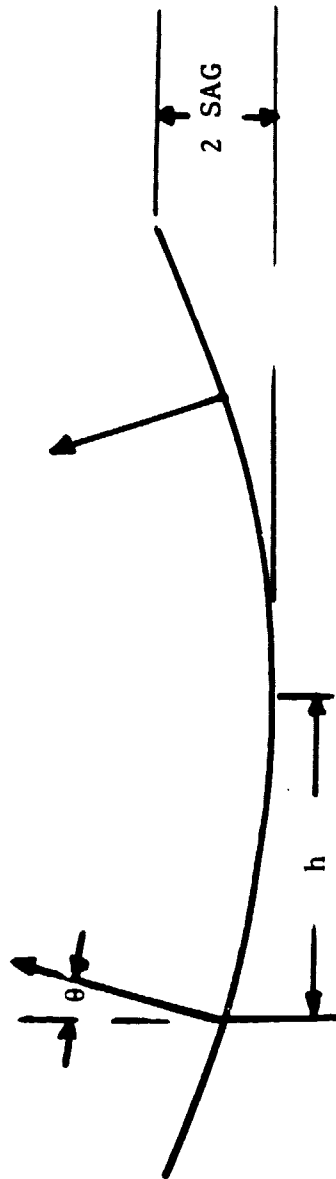


Fig. 3-14 Static Focus Error

The different subapertures using the mirror will have a different tilt given by

$$\theta = \frac{h}{R} = \frac{4 \text{ SAG}}{h} \quad (3-18)$$

where  $h$  is the vertex to the center of the subaperture distance, and  $R$  the radius of the mirror, and

$$2 \text{ SAG} = h^2/2R \quad (3-19)$$

Thus a sag of  $\lambda/100$  will produce a tilt error of  $0.08 \mu\text{rad}$  for a subaperture center  $0.25 \mu\text{m}$  from the vertex. This will produce an error in  $L$  of  $0.6 \mu\text{m}$  (see the alignment system discussion of tilt). This is about 10 times the tolerance on  $L$  for a 10 arcmin FOV. Calibrating the OPD error does not correct for this error in  $L$ . Consequently, the alignment system must give a measure of the focus of the end mirror or the focus tolerance on the end mirror must be better than  $\lambda/100$ , or the FOV of the interferometer must be reduced. We assume that the alignment system will measure the focus.

A  $\lambda/100$  tolerance on focus sag is difficult to achieve on a 0.9-m diameter mirror. In addition, thermal changes could produce a change in SAG: If the differential heat load on the mirror (front minus back) is  $q$ , the central sag of the mirror is  $w$  (Fig. 3-15)

$$w = \frac{q d^2 (\alpha/\kappa)}{24} \quad (3-20)$$

where  $d$  the mirror diameter,  $\alpha$  the thermal expansion coefficient,  $\kappa$  the thermal conductivity. For a worst case calculation, assume a ULE mirror for which  $(\alpha/\kappa) = 2 \times 10^{-8} \text{ m/w}$ ,  $q = 10 \text{ w/m}^2$  (input from 300 K baffle tubes to front of mirror, back free to radiate, mirror front emissivity 0.02). Then we find a sag of  $w = 100 \lambda = \lambda/50$ .

ORIGINAL PAGE IS  
OF POOR QUALITY

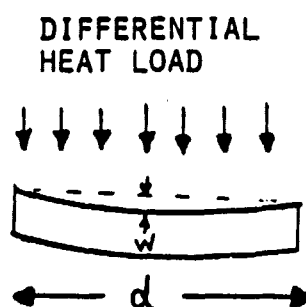


Fig. 3-15 Thermal Sag

A beam walk error is an error caused by the field shift of a star as the interferometer rotates. Fig. 3-16 illustrates this effect. The beam is considered rectangular here for simplicity. As the field angle changes, the beam footprint on the end mirror shifts from the solid rectangle to the dashed rectangle. The maximum possible shift is

$$\Delta x = \frac{L}{2} \text{FOV} \quad (3-21)$$

The corresponding error in  $\delta$  is equal to the average piston of the solid rectangle minus the average piston of the dashed rectangle. Thus the worst case is for maximum shift to occur over a region which coincides with the largest possible wavefront error introduced by the mirror:

$$\Delta \delta \leq \frac{\Delta x}{d} (\text{Max WFE}) \quad (3-22)$$

where  $d$  is the beam diameter, The maximum WFE is twice the peak-to-valley error on the mirror. Thus, assuming that a  $\lambda/100$  rms mirror has about a  $\lambda/20$  peak-to-valley error;

$$\begin{aligned} \Delta \delta &\leq \frac{\Delta x}{d} 10 \text{ (rms surface error)} \quad (3-23) \\ &= 2.8 \times 10^{-10} \text{ m (worst case)} \end{aligned}$$

This exceeds the allowed error by nearly a factor of 3; but is unlikely that this error would actually be observed. On the other hand, a  $\lambda/100$  rms mirror may be equally unlikely to obtain.

The beam splitter is the most difficult optical element in the system. Fig. 3-17 illustrates the baseline system beam splitter. Fused silica is used in order to minimize radiation damage during the long life of the mission. Unfortunately, fused silica has a high temperature coefficient of its refractive index, and the subsequent thermally induced changes are of great concern.

ORIGINAL PAGE IS  
OF POOR QUALITY

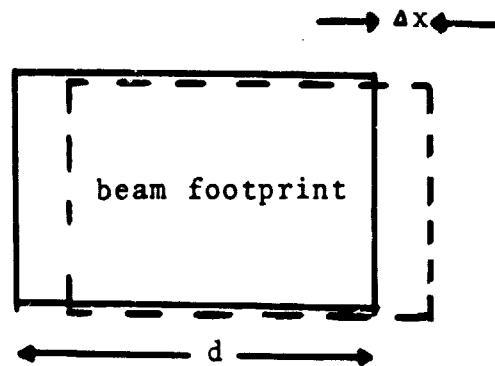


Fig. 3-1b Field Shift Error

ORIGINAL PAGE IS  
OF POOR QUALITY

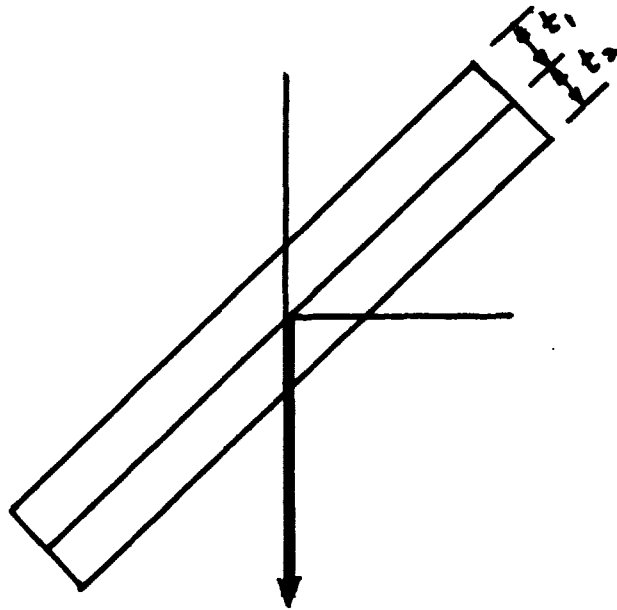


Fig. 3-17 Beamsplitter Errors

C-2

Discussions with optical fabrication houses has given indication that a 1.25 m fused silica beam splitter can be fabricated with surface accuracy sufficient for the interferometer. There will be some "average peal" effect but this, as well as residual surface errors, will be detected by the OPS sampling system and will not cause an error.

It is not possible to produce a 1 m beam splitter with good optical surface characteristics and also one which has plane parallel surfaces. That is,  $t_1 - t_2$  will vary across the surface. This will produce varying amounts of relative dispersion in the two beams. This could seriously degrade the visibility of the white light fringes. We assume here that some solution to this problem will be found. Techniques using channel spectra have been suggested. At worst, the beam splitter can be subdivided into separate pieces which are plane parallel; i.e. a 4-channel beam splitter can be used. This would require a separate monitoring system to align the four elements, but this is not much more difficult than the current alignment scheme already postulated for the baseline.

There will be no beam walk errors for the beam splitter since it is the pupil. The various subapertures will be masked on the beam splitter to assure this fact.

### 3.6.2 Alignment system

The alignment system consists of an active system which adjusts the tilt and separation of the end mirrors, and a monitoring system which monitors the tilt and translation of the remaining elements. The major error which is introduced by tilt and translation is an error in  $L$ , not  $\delta$ , which has relatively loose tolerances.

Fig. 3-18 shows the effect of tilting one of the end mirrors. Since the entrance pupil is at the beam splitter, the effect of tilting the



ORIGINAL PAGE 19  
OF POOR QUALITY

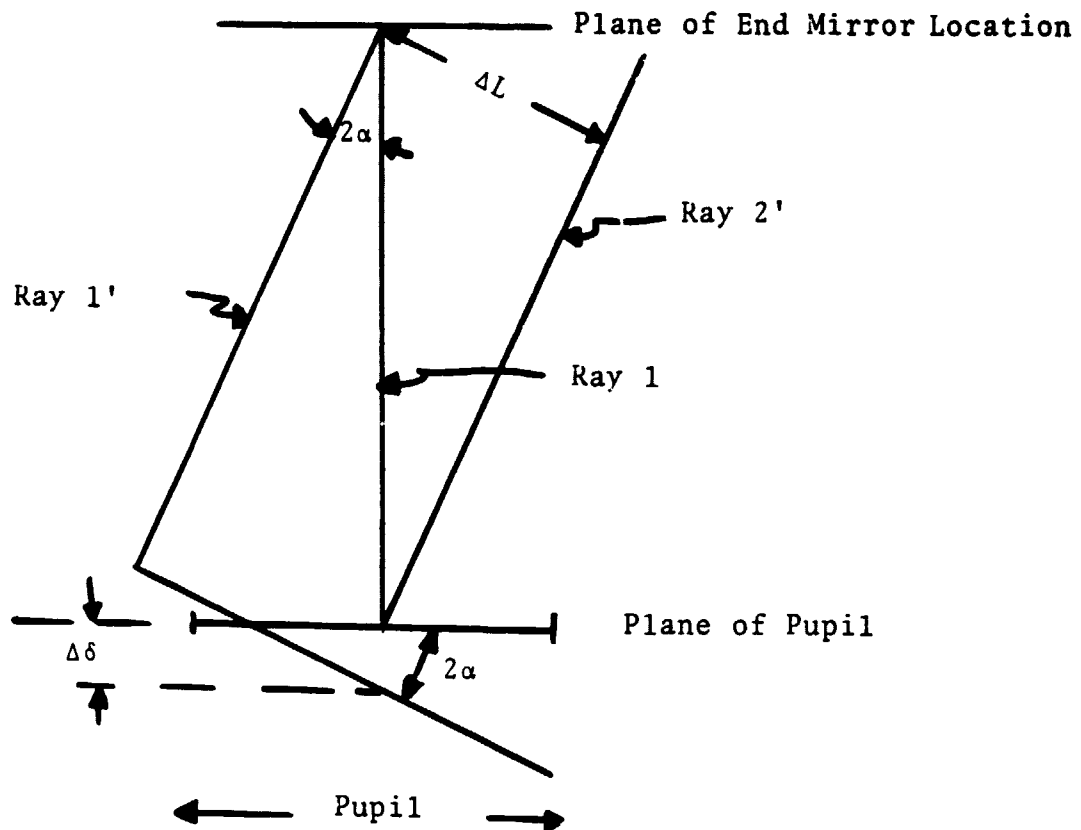


Fig. 3-18 Mirror Tilt Errors

the end mirror is much greater than any other element. In Fig. 3-18 if the end mirror has no tilt error, the ray which hits the center of the entrance pupil is Ray 1. If the mirror is tilted by an angle  $\alpha$ , the ray is tilted by an angle  $2\alpha$ , shown on the figure as Ray 1'. Keeping the optical path length constant, the ray has swung along the dashed arc at the pupil plane and, as drawn, misses the pupil entirely. The wavefront that hits the pupil is the straight line tangent to the dashed arc at the Ray 1' position. It is, of course, tilted with respect to the old wavefront by the angle  $2\alpha$ . The ray which now hits the center of the pupil is Ray 2'. The several effects of the mirror tilt can now be seen:

1. The visibility of the fringes changes. For, assuming that the wavefront from the other arm is unchanged, the two interfering wavefronts are now incident with an angle of  $2\alpha$  between them. However, a tilt of  $0.01 \mu\text{rad}$  will produce a phase change across the pupil of about  $\lambda/60$  - negligible.
2. The piston is changed by the amount  $\Delta\delta$ ; but this change is the same for all stars and hence there is no net error.
3. The footprint on the mirror is shifted; but this shift is much smaller than the field shift beam walk.
4. The baseline is changed by

$$\Delta L = \alpha L/2 \approx 0.08 \mu\text{m} \quad (3-24)$$

This change is marginal for a  $10'$  FOV since the required accuracy is

$$\Delta L = \frac{L^2}{\delta} \cos \theta d\theta = \frac{L}{\cos \theta} d\theta \quad (3-25)$$

$$\approx 0.05 \mu\text{m}$$

The translation of the other elements also produces an error  $\Delta\delta$  on a one-to-one basis as shown in Fig. 3-19. There is also a  $\delta$  change but since it is the same for all stars, there is no net error. It is not necessary to correct this translation error, but it must be monitored and used in the data reduction. Tilt of the elements has less effect on  $\Delta L$  than the end mirrors since the lever arm is much smaller.

### 3.6.3 OPD Measurement System

The simplest OPD system for the interferometer is one which measures the relative delay line position and nothing more. One such technique is illustrated in Fig. 3-20. It uses simple z-axis driver mirrors for the delay with a figure sensor to measure average piston of one mirror relative to another. Even this system is a challenge over a 0.9-m aperture, but it places a great burden on the rest of the system with respect to alignment tolerances. However, this technique, or some variation of it, is the only one which does not require weak gratings or some retro-reflecting element on the end mirrors.

Once a more complicated system is used, there is a choice between one arm and two arm interferometers. A one arm system would require gratings on only one end mirror and interfere the return beam with a reference wave. However, this scheme is really little better than the figure sensor since it does not sample the errors in the other arm.

The two arm system used in the baseline design has the advantage that it samples both arms, and by interfering the return from one arm with the other, it automatically reads the desired OPD directly. Furthermore, the interferometer can be broken into 4 systems, since it is located in the common path region, thereby reducing the

ORIGINAL PAGE IS  
OF POOR QUALITY

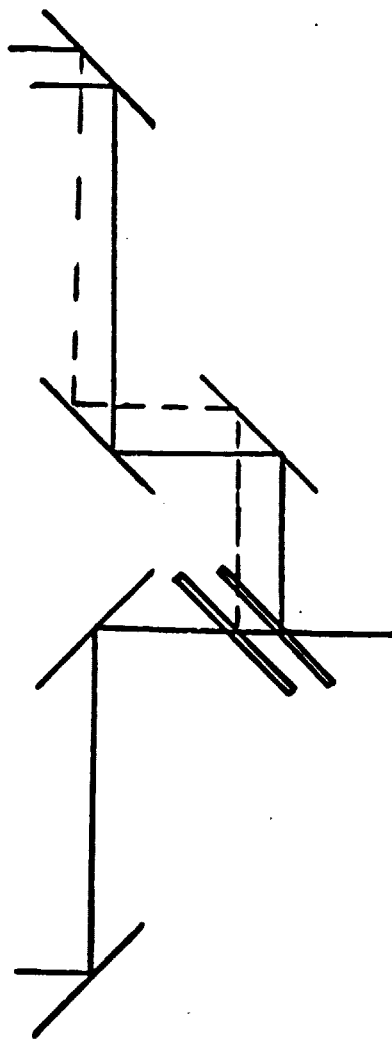


Fig. 3-19 Mirror Translation Error

ORIGINAL PAGE IS  
OF POOR QUALITY

LMSC-D870835

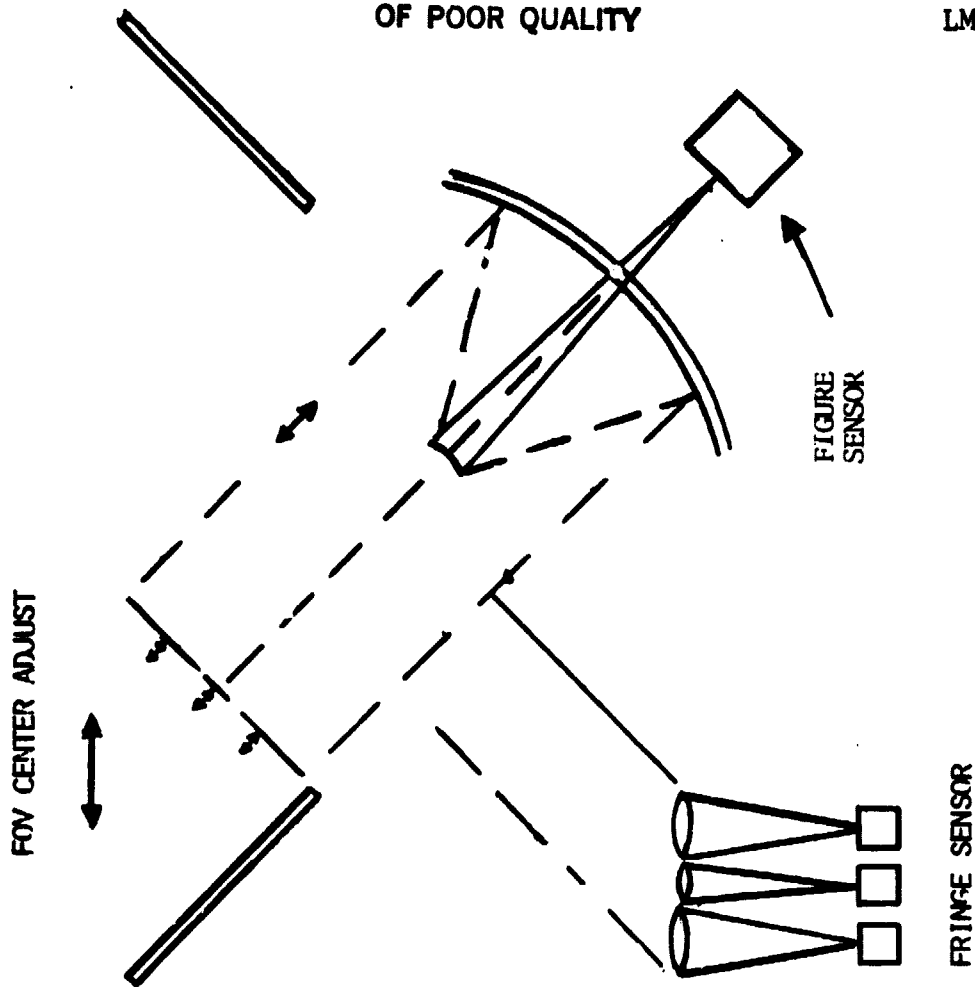


Fig. 3-20 One Arm OPD System by Delay Line Measurement

required sub-aperture to 0.4 meters. The interferometer errors are negligible.

Fig. 3-21 shows the two arm system with gratings on both end mirrors to return the beams in this figure the delay lines are again z-driven simple mirrors, simpler than trombones, but they produce additional beam walk on the end mirrors. Fig. 3-22 shows the beam walk due to the delay line mirrors. The trombone was chosen as the baseline in order to minimize the beam walk.

The beam splitter is segmented in Fig. 3-21, greatly relaxing the fabrication difficulties. The four beam splitter segments need not be phased in piston with respect to one another (since that is monitored), but they must be held parallel to one another. It might be tempting to break the system into four separate interferometers, but the temptation should probably be avoided: Maintaining a common axis for four separate interferometers would be critical to micro-arcsecond accuracy; this is beyond the proposed alignment system accuracy.

Fig. 3-22 shows a side view of the gratings on the end mirrors. The grating equation shows that a grating spacing of  $0.447 \mu\text{m}$  is required for  $6328 \text{ \AA}$ . At this angle the grating acts exactly like a mirror in that a change in the angle of incidence implies a corresponding change in the angle of refraction:

$$\frac{d\theta_n}{di} = 1 \quad (3-26)$$

It would be more convenient if the grating acted as a retro-reflector since off-axis rays out to the end mirror will not return on the same path.

Thermal expansion of the grating will change the return angle:

ORIGINAL PAGE IS  
OF POOR QUALITY

LMSC-D870885

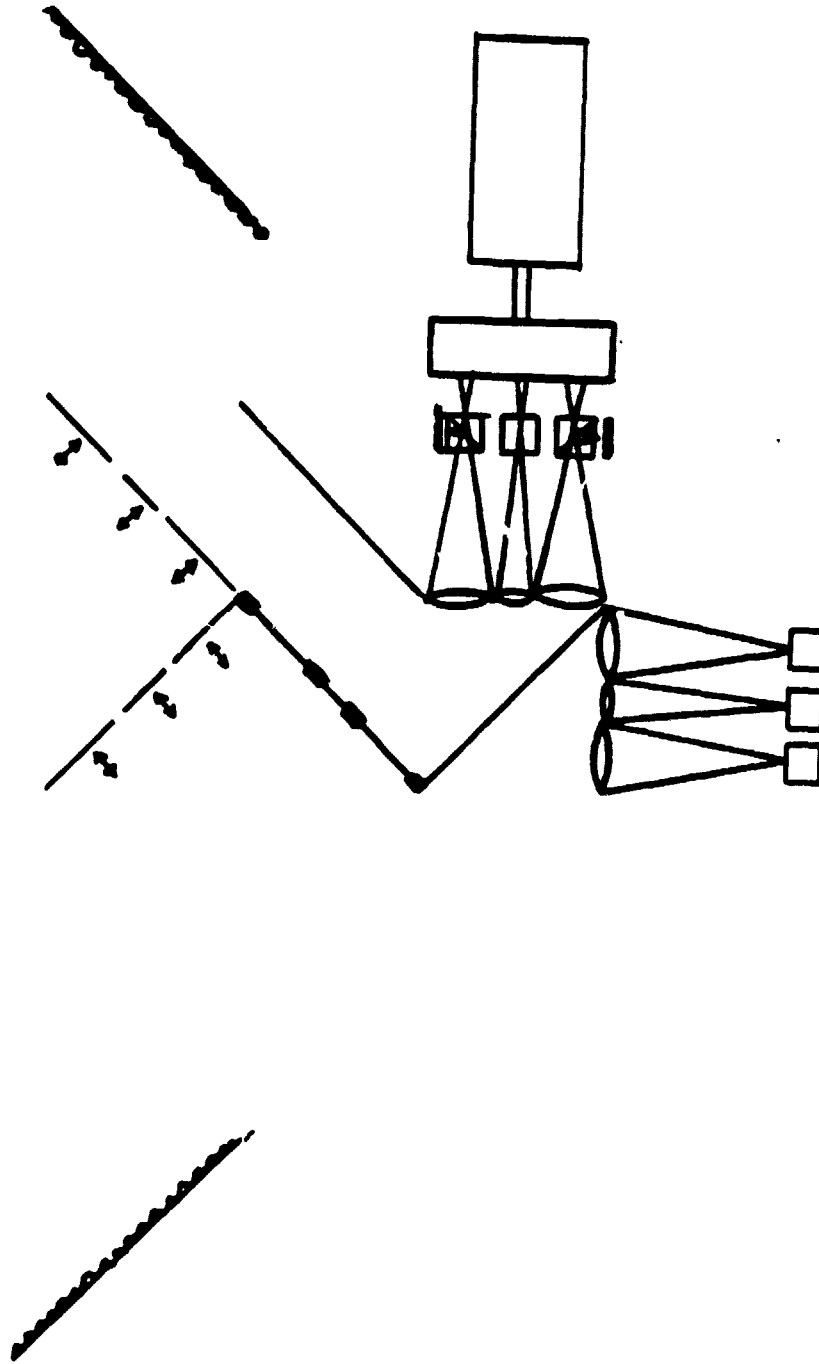


Fig. 3-21 Two Arm OPD System

ORIGINAL PAGE 13  
OF POOR QUALITY

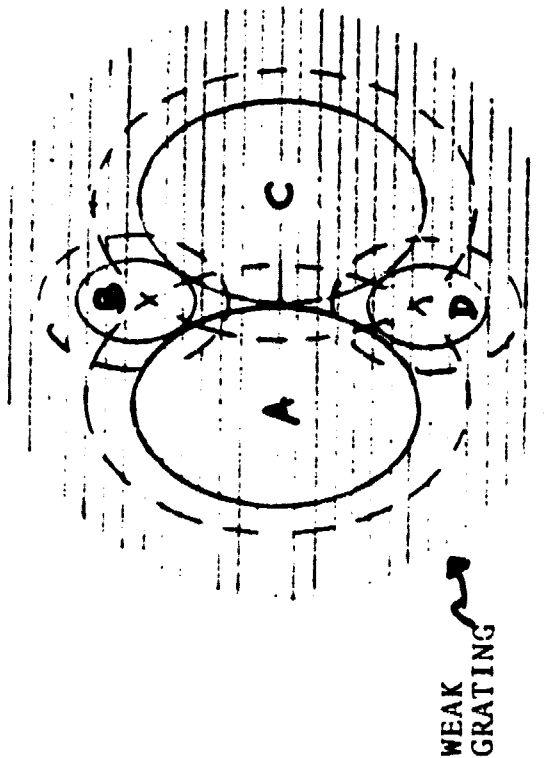
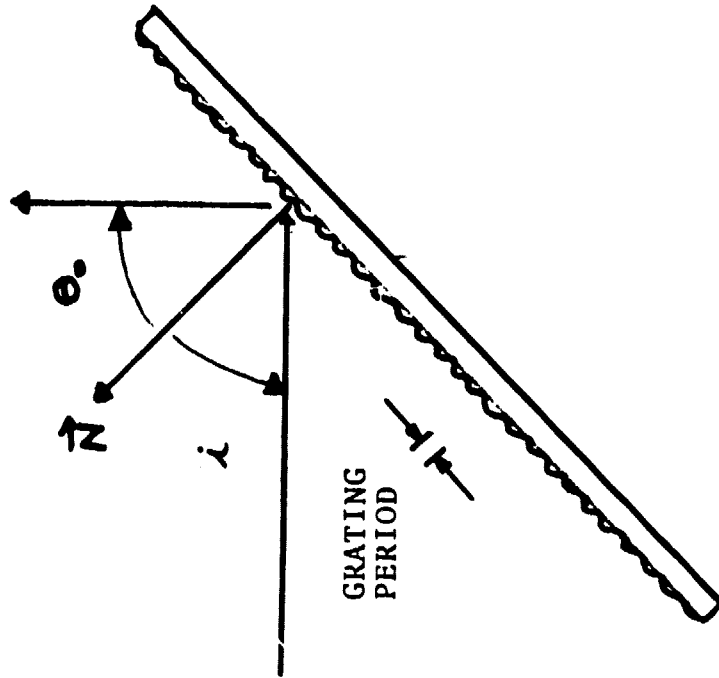


Fig. 3-22 Interferometer End Mirror Layout (Grating Sampler)



$$d\theta_n = \frac{-\lambda}{p^2} \frac{dp}{\cos i} = 2 \cdot \alpha \cdot \Delta T \quad (3-27)$$

where  $\alpha = 10^{-8}/^\circ\text{K}$ . Thus  $\Delta T < 0.5^\circ\text{K}$  is required for  $\Delta\theta_n < 10^{-8}$  rad. There are no diffracted star light orders which hit the receiver.

A shift in the beam across the grating, caused by a mirror tilt, for example, at first sight appears to be fatal. That is, a translation of one period (i.e.  $0.4 \mu\text{m}$ ) will produce a  $\lambda$  error in the  $\delta$  measurement. However, it will shift equally for all the stars, and thus there is no net error.

A true error will be produced by a differential shift of the grating due to perhaps a thermal excursion. (Fig. 3-23). A differential shift of only  $0.71 \text{ \AA}$  would produce a  $10^{-6}$  arcsec error in star position. The only way a grating can be used with confidence is if calibration by star switching is frequently used.

#### 3.6.4 Fringe Tracking System

The fringe tracking system, like the OPD interferometer, is relatively free from introducing new errors since it is in the common path region. The technique used successfully by Shao and Staelin are appropriate here. The detector itself may be an image dissector tube. Despite poor quantum efficiency it is superior to the alternatives for this application.

#### 3.6.5 Conclusions

The feasibility of the 15-m baseline interferometer appears questionable. The greatest problem lies with the use of gratings as a metric; but also the fabrication and temperature stability of the optics have extremely tight tolerances. The number of monitored and controlled elements is quite high so that the overall control system is very complex.

A conceptual breakthrough in the OPD measurement system could change this assessment. For example, Peasenberg has suggested that a small relector could be placed several meters in front of each end mirror for the OPD sampling beam. In this case, the gratings on the end

ORIGINAL PAGE IS  
OF POOR QUALITY

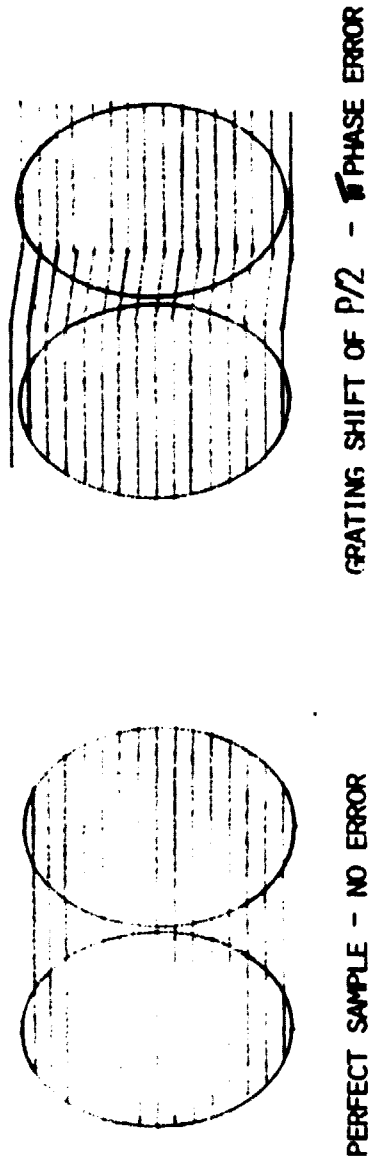


Fig. 3-23 Grating Error

mirrors could focus on those reflectors instead of going straight back through the system. This scheme gives an easier grating configuration and has less potential for errors. Of course, it has its own problems, and the gratings themselves are still an issue for it.

In view of the several error sources, the issue of calibration by star switching - with all channels looking at the same star at one time - is central to the interferometer feasibility. Due to beam walk errors and potential time-varying errors multiple calibrations are required. For some scenarios (e.g. all stars are dim) this calibration seems not possible. If a bright star is available (i.e. in the FOV), then calibration can be important. Scaling the system up (larger end mirrors, longer baseline) may actually improve the accuracy by making more frequent calibration possible. Scaling the system down in size could be effective in reducing error sources. The issue of scaling, then, deserves critical attention in the future study of the system.

### 3.7 Overall System Design

Figs. 3-24 to 3-26 show on a concept level an overall systems design of the baseline spaceborne astrometric interferometer.

Fig. 3-24 shows the payload (i.e. the instrument itself) structure and rough optical layout. The structure is a truss design, with an overall rectangular (box) appearance. The structural elements are cylindrical tubes made of especially rigid and thermally inert material such as Gr/Ep or Gr/metal. Gr/Mg is best from a materials properties point of view (cf. Sec. 2.5) but is most expensive. The less expensive Gr/Ep was actually costed in this study, the cost savings being in the range of 10 to 20 M dollars. The smallest structural unit are triangles for maximum rigidity.

The structure as shown is deployable, for increased STS payload volume efficiency. The structure folds once at the center line (optical axis of the interferometer) and is stored in the Shuttle bay as shown on the RHS of Fig. 2-24. The deployment following ejection of the satellite from the Shuttle is illustrated in Fig. 2-25. Overall dimensions of the interferometer structure are 16.5m X 3.1m X 1.6 m.

Fig. 2-24 shows the location of the end mirrors and of one of the trombone -design delay lines plus focussing optics and focal plane location. Not shown are possible sunshades (extensions of the baffle tubes of each end mirror) and the possibly complete wrapping of the structure (except for the optics ports) in heat-insulating multilayer insulation blankets (MLI). The optical paths are individually baffled and insulated. Individual wrapping of structural members in MLI may be preferred to wrapping the structure as a

LMSC-D870885

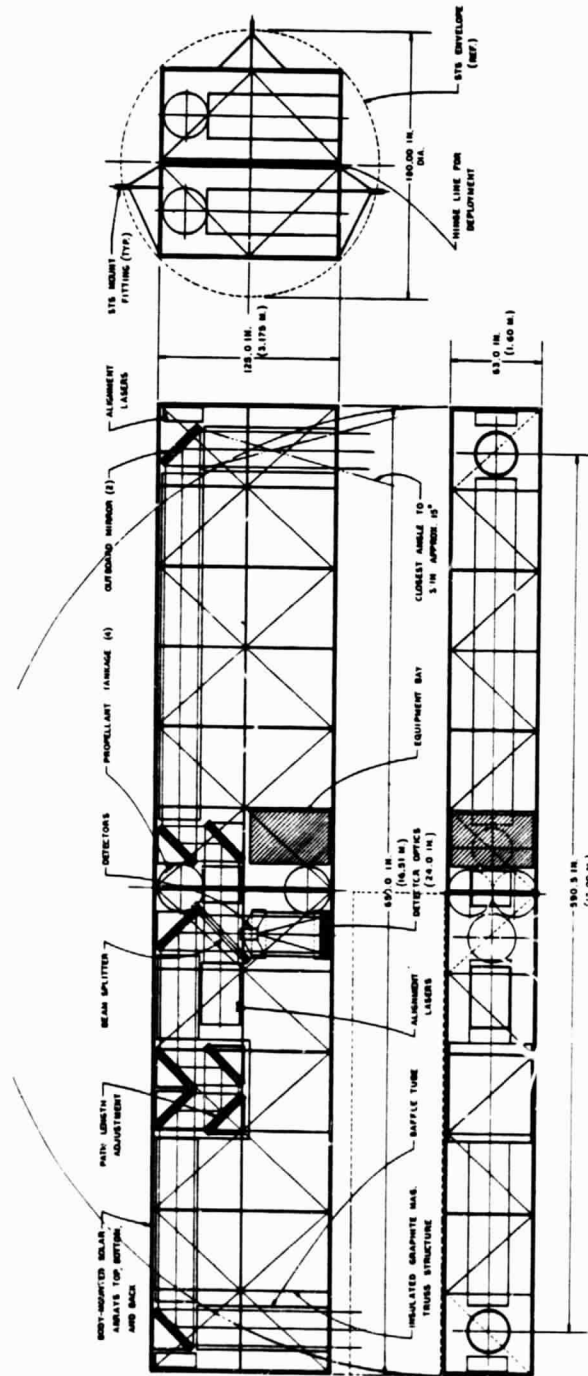


Fig. 3-24 Interferometer System

3-51/52

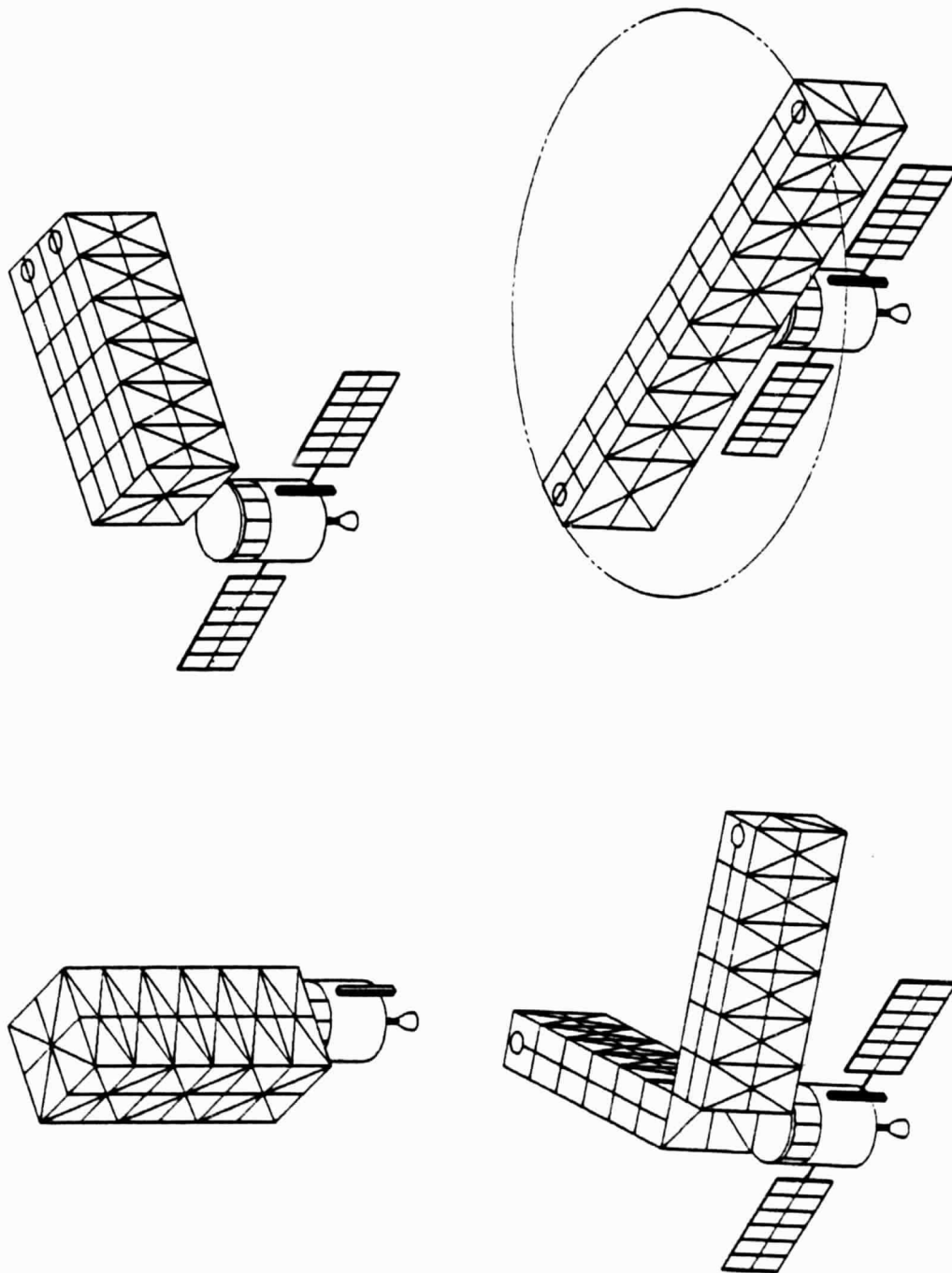


Fig. 3-25 Interferometer deployment

whole - the issue requires study at the design level.

Fig. 3-25 shows the satellite in several stages of deployment. The interferometer package is hinged from the spacecraft. The solar arrays (S/A's) are also deployable and have two degrees of freedom for sun-tracking. The S/C includes a propulsion system for orbit transfer or orbit maintainance. Typical requirements for a one-way transfer of the satellite from STS hand-off at 150 n.mi. to the operational orbit (325-350 n.mi.), in a co-planar orbit transfer, requires approximately 1000 lb of hydrazine propellant (less for a bi-propellant). Alternatively, the system could be directly inserted by the Shuttle into the final orbit; but this would require adding an OMS propulsion kit to the shuttle and reduce the payload capacity.

Fig. 3-27 shows several view (CADM drawings) of the deployed satellite, indicating locations of hi-gain antennas and payload spacecraft interfaces.

The spacecraft is assumed to be a new design for such a large system as the baseline interferometer, and contains the standard subsystems for electrical power generation, handling and storage, for attitude control and guidance (ACS), for communications and data handling (CD&H), for propulsion, and for thermal control. For a detail call-out of the components of these subsystems see Table 3-3.

The interferometer rotates about its optical axis, the system's center axis, as indicated in Fig. 3-24. Since the rotation is likely to be slow (rotation period 10-20 min perhaps), the satellite could be made to rotate as a unit; alternatively, the

ORIGINAL PAGE IS  
OF POOR QUALITY

LISC-D870885

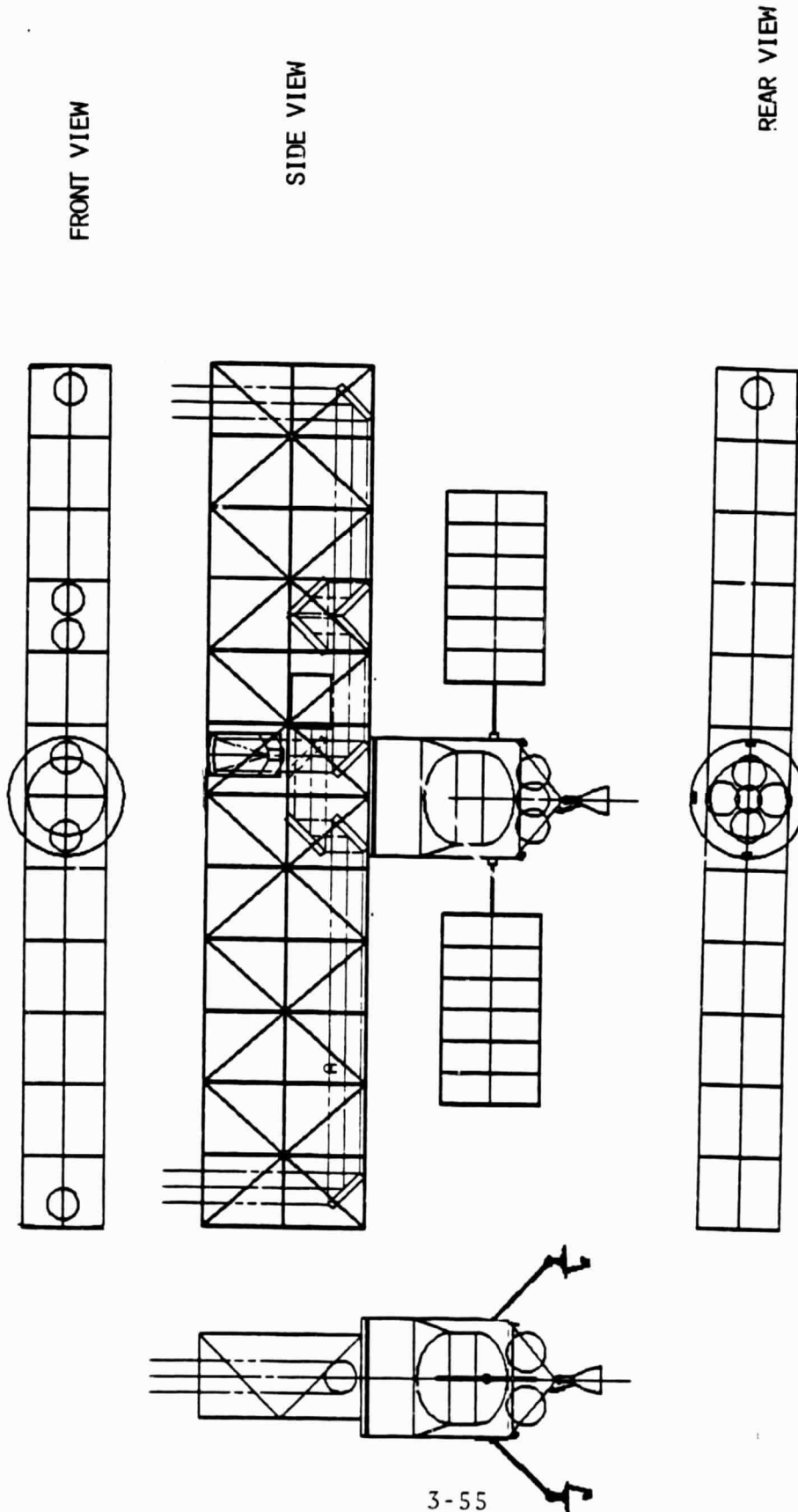


Fig. 3-26 Deployed Interferometer



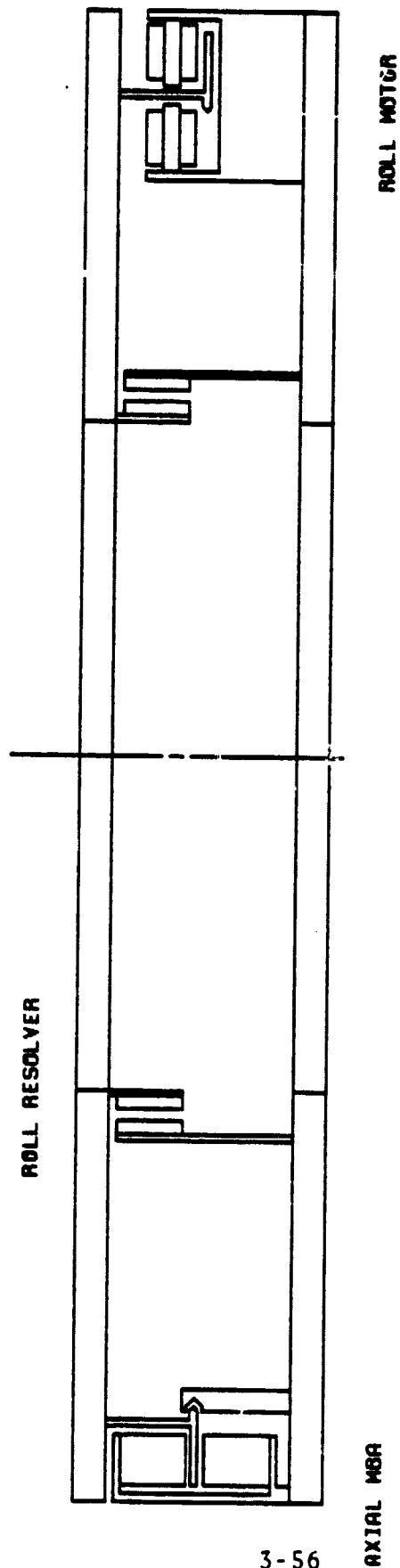


Fig. 3-27 Magnetic Bearing Assembly (MBA)  
(Sperry-Rand Concept)

the interferometer alone could rotate, on a spin table, relative to the S/C. In the first case, there is a possible loss of average power collected by the S/A's due to the ever-changing solar angle. unless the S/A's are rotationally isolated from the rest of the system. In the second case, the interferometer rotates on a spin platform of the S/C. Magnetic bearings in a design such as illustrated in Fig. 3-27 would be used to acoustically isolate the sensor from the S/C. Power transfer and communication links between payload and S/C can be achieved in various ways, e.g. by laser. Electrical power for the sensor itself could also be obtained from solar arrays on the sides of the structure.

### 3.8 Weight

Weights of subsystems and components were based on direct calculations as well as on comparisons with similar or related systems and subsystems. The results are shown in Table 3-3. The total dry weight is about 4500 kg, dividing into Mission Equipment (ME) which is the interferometer, of about 2300 kg, and the spacecraft of about 2200 kg. All weights as shown include 10% contingency.

### 3.9 Cost

Cost estimates for the Mission Equipment were generated parametrically, with judgements made for exotic components. The development cost includes brassboards for components and a prototype flight unit. No GFE (Government Furnished Equipment) was identified, no facilities costs were included, nor launch and operations costs. The cost summary is given in Table 3-5. The numbers represent planning type numbers associated with the current state of program definition. The total cost is \$296.2M; and this number is uncertain by about 25%.

TABLE 3-3  
INTERFEROMETER WEIGHT ESTIMATES  
(kg)

MISSION EQUIPMENT		SPACECRAFT (CTD)	
<u>Structures</u>		<u>Propulsion</u>	
Outer Structure	545	Tanks	141
Optical Tubes & Baffles	103	OAS Motor & Mount	36
<u>Thermal Blankets</u>		Electronics	14
		Valves, Plumbing, Brackets	53
<u>Optics</u>		ACS	
End Mirrors & Holders (2)	163	ACS Thrusters	118
Central Mirrors & Holders (3)	245	Inertial Torquers	227
Beam Splitter	336	Geomagnetic Fine Torquers	105
Path Length Compensator Assembly	427	Control Electronics	7
Telescopes	136	IPR System & Electronics	38
<u>Focal Plane Assembly &amp; Support</u>		Stellar Attitude Sensors & El.	39
		Plumbing, brackets, etc.	38
<u>Alignment Lasers (3)</u>		Communications	
	227	Receivers & Transmitters	24
<u>ME Total</u>		Tracking Beacons	7
	2333	Signal Conditioners	5
	=====	Telemetry sensors	9
		Brackets & Misc.	4
SPACECRAFT		Antennas	
<u>Structures</u>		Downline antennas	27
Deployment Mechanisms	68	Beacon Antennas	3
Equipment Rack	273	Multiplexers	5
STS Mount Fittings	159	Command & Data Handling	
Hold-Downs & Minor Mech.	27	Computer	18
Fastenings & Misc.	36	I.O. Processor	27
<u>Thermal Control</u>		D.P. Electronics	23
Blankets	23	Data Recorders & Electronics	109
Heaters, Sensors, Control Electr.	30	Brackets & Misc	15
Bracketry & Misc.	11	Electrical	
Air Conditioning (pre-Launch)	18	Solar Arrays	159
Shutters & Actuators	23	Batteries, Conditioners, Controllers	213
<u>Grand Total (dry)</u>		Power Junction Box	18
	4492	Cabling, Connectors etc.	109
	=====	S/C Total	2159
			=====

ORIGINAL PAGE IS  
OF POOR QUALITY

LMSC-D870885

ORIGINAL PAGE IS  
OF POOR QUALITY

LMSC-D870885

TABLE 3-4  
INTERFEROMETER COST ESTIMATES\*

	DEVEL. & BB	PROTOFLT	TOTAL
Optics -0.9m	4.2	10.1	14.3
Beamsplitter & Compens.	10.3	11.4	21.3
Telescope 0.9m			
Telescopes 0.4m (2)	7.4	8.1	15.5
Telescopes 0.1m (2)	5.6	5.8	11.4
Delay Lines 0.56m (2)	3.2	4.8	8.0
Delay Lines 0.14m (2)	1.0	1.0	2.0
FPA & Electronics	2.6	4.5	7.1
Gratings	5.0	4.2	9.2
Lasers	10.0	1.5	11.5
Optics Alignment & Control	15.2	9.3	24.5
Computers & S/W	16.1	12.1	28.2
Optical Structure	24.5	7.4	31.9
Outer Structure			
Thermal Blankets	3.8	0.9	4.7
Design, Devt., Hdw	108.9	81.1	190.0
GSE, GHE, STE	10.6	7.2	17.8
Integration & Test	15.7	12.1	27.8
Systems Eng., Q.A., Rel.	22.4	16.5	38.9
Prog. Managt. & Data	12.5	9.2	21.7
TOTAL	170.1	126.1	<u>296.2</u>

\*Payload (Mission Equipment) only

## 4. IMAGING ASTROMETRIC TELESCOPE

### 4.1 Summary

This chapter the principles of operation of the imaging astrometric telescope and the considerations leading to a baseline design of the 16.5-m focal length system. Particular emphasis is laid on the algorithm for signal processing, the choice of detectors, and the stability of the focal plane assembly (FPA). Error sources are identified and their effect on the baseline configuration is examined, in particular the effects of aberrations on the systematic measurement errors and the implication on telescope size.

The imaging telescope is within the state-of-the-art, and our conceptual baseline system uses available technology. An improved baseline makes use of advances in solid state detectors which we expect to occur in the next several years.

Ray trace studies of the aberrations of various optical forms (including refractors) showed the simple parabolic reflector (no subreflector) to be best. The  $f/16$  system is essentially diffraction limited. As the  $f/\text{No.}$  decreases, particularly below  $f/8$ , coma rapidly increases the star image (spot size) thereby decreasing the measurement accuracy by increasing the SNR. As a consequence, the scaled-down telescope ( $f/8$ ) is limited by coma, if other systematic errors do not predominate, and the performance in terms of observation time for a given measurement accuracy is worse for the  $f/8$  than the  $f/16$ , by a factor of 1.4.

We suggest that systematic errors other than photon noise or coma

limit the performance ultimately, but this will depend on the star position measurement algorithm and the scenario. No best algorithm was found, but the centroid integrator (the image centroid being defined as the star position) was chosen as a baseline. It is insensitive to image shape, yields a low data rate, and directly measures the image centroid.

In contrast with the interferometer, the telescope measures a large number of stars simultaneously, and it derives its measurement precision by repeated centroid measurements of these stars. The interferometer makes high-precision measurements of a few (3-4) stars. The stars vary widely in brightness, thus the detecting scheme requires detectors with high spatial resolution, temporal bandwidth, and dynamic range. Detectors such as used in ground-based versions of the concept by Gatewood and Jones are thereby ruled out. We suggest using large area CCDs.

The focal plane architecture involves a split FOV, with a separate detector for the bright center star (the K5,  $m=7.3$  star in the baseline task), and four quadrants each a large area CCD or CID. The focal plane is passively cooled using radiators.

The Ronchi ruling performs the actual measurement of star position. The material of the substrate is fused silica. The lines can be deposited using photolithography or, better, with a diamond ruling machine. A calibrated accuracy of  $0.01 \mu\text{m}$  appears to be possible to obtain for the line accuracy.

Misalignment of the grating is a serious source of systematic errors. Those errors not linear with field angle must be accounted for by higher order modeling rather than the affine transformation appropriate to take out the linear errors.

The modeling may be limited by the SNR of the instrument.

Detector non-uniformities, which could be a source of concern, are minimized by the proper design of the optics relaying the images from the Ronchi ruling to the detectors. A small penalty may be paid in increased background noise; but this may not be serious since most stars are background-limited.

A potential systematic error source is the rotation of the ruling or telescope as a unit, between x and y measurement of star positions. Solutions for the problem are suggested, such as a crossed grating of a double-barrel telescope (each system measuring one of the components of star position, and simultaneously).

An overall systems concept design of the astrometric satellite was made. The telescope structure is a telescoping Gr/Ep or Gr/metal cylinder. As in case of the interferometer, deployment is volume efficient for packaging in the STS payload bay and incurs no identifiable performance penalty.

Total weight of the baseline system is 3800 kg and includes a new spacecraft. An ROM cost estimate, derived parametrically and with judgments for exotic components, gives \$130M for the payload

#### 4.2 Principle of Operation

A schematic description of the measurement principle is given in Fig. 4-1. A single mirror of diameter  $D$  and focal length  $f$  images the star field on a moving reticle. The reticle modulates the star light, which is then reimaged by a relay lens on a detector. The star position, which is encoded in the modulated signal, is retrieved by the data processor. Several features of the measurement scheme are apparent:

LMSC-D870885

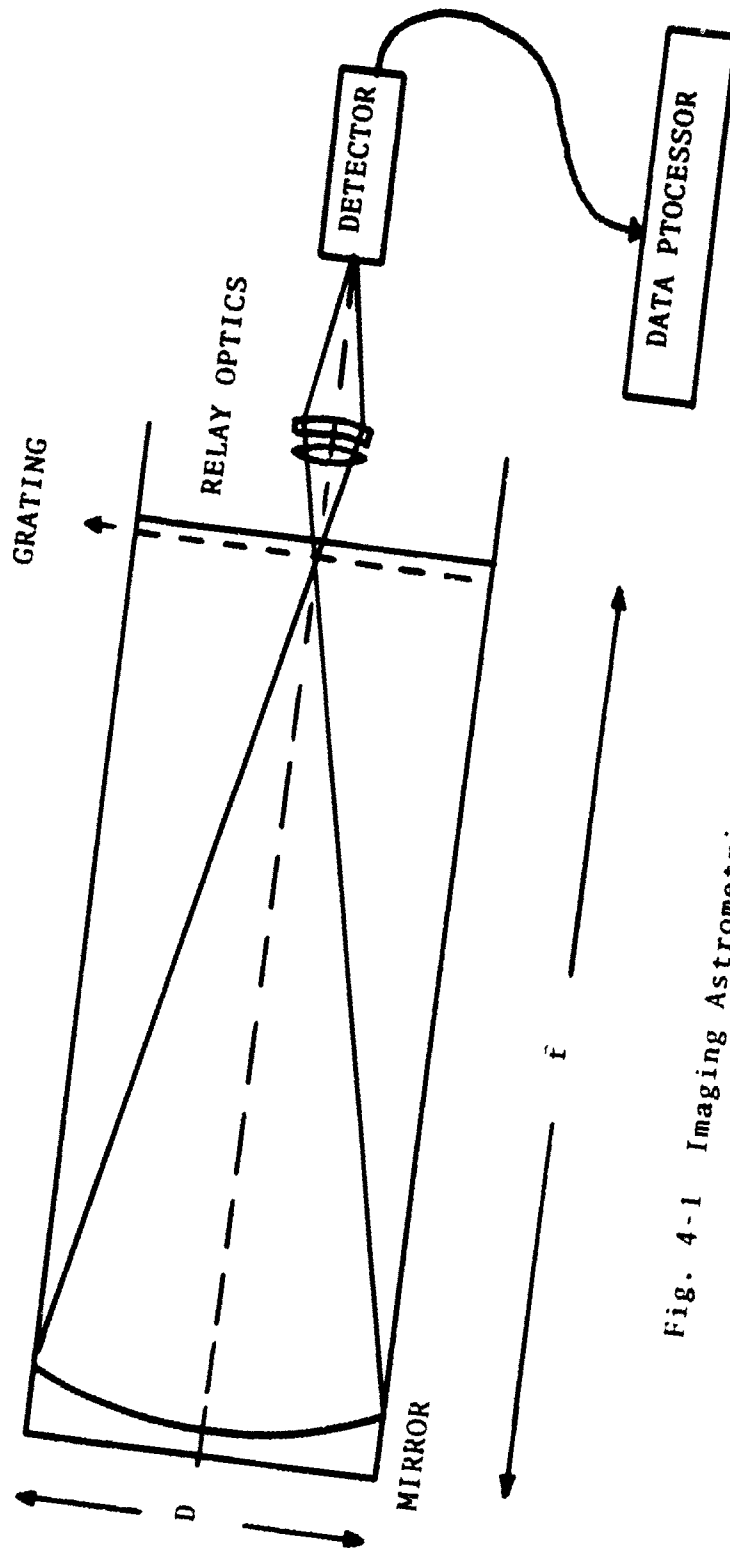


Fig. 4-1 Imaging Astrometric Telescope Schematic



1. The grating modulates simultaneously all the stars in the FOV and thus the position measurements for these stars are conducted in parallel. Many error sources - vibrations, thermal expansion - are field-independent and will therefore cancel when relative measurements are made.
2. The only optical element in the imaging system which may introduce measurement errors is the mirror. However, since the mirror is at the system pupil, the errors are common to all stars in the FOV and cancel. Field-dependent aberrations do exist, however, and their effect is discussed below.
3. The relay lens is not a critical element in the measurement system. Its function is to collect the star light and direct it onto the appropriate detector. Since the detector integrates the light over the whole image, aberrations in the lens do not introduce measurement errors as long as the light reaches the detector.
4. The detector must resolve the stars in the FOV.

The implications of these system features on the design are discussed later in detail.

#### 4.2.1 Image Position and Stellar Position

There are four fundamental questions which must be asked in order to fully understand the measurement scheme:

1. What is the optimal observable image parameter that should be defined as the star position?
2. What is the relationship between this parameter and the information encoded in the signal?
3. What is the best estimator of this parameter assuming various noise sources?

4. What are the systematic errors which affect the measurement and how can they be compensated for?

The stellar disks are unresolved and the stars are far enough that their position is unambiguously defined by the angular direction of the plane wave received at the telescope aperture. However, the stellar image at the focal plane, the point spread function (PSF), has structure, and the relationship between the PSF and the wavefront tilt has to be accurately established. For an aberration-free optical system the relationship is easily established; the resulting Airy distribution is symmetrical and centered at the geometrical image position. However, when aberrations are present the PSF loses this symmetry and an image parameter which is related to the geometrical image position has to be defined. The standard criterion of diffraction-limited optics - the Rayleigh criterion - is not good enough when, as in our case, the required measurement accuracy is of the order of  $10^{-6}$  of the Airy diameter.\* Understanding the effects of aberrations on the PSF is extremely important since they are a potential source of systematic errors. Aberrations can be field dependent and the observed stars will move in the observation field over the 5 years of planned observations.

Several image parameters can be defined as the stellar position. Among the most frequently used are the peak of the irradiance distribution, the mean of the distribution, and various averages of the distribution.

The peak of an aberrated image does not necessarily occur at the geometrical image position and is therefore not a good parameter. This is also true for the median of the distribution although it is probably most commonly used as position parameter. The median is defined by dividing the image into two parts of equal energy - which is what bi-cells or quad-cells do.

\* Airy diameter  $= 2.44\lambda/D = 0.3$  arcsec

The weighted averages used as position parameters are usually defined as

$$\bar{x} = \iint_A x E^k(x,y) dx dy / \iint_A E^k(x,y) dx dy \quad (4-1)$$

where  $E(x,y)$  is the image irradiance distribution over the observation aperture  $A$ . For  $k=1$  one obtains the first moment (centroid, or: center of mass) of the distribution. The relationship between the diffraction PSF and the aberrated wavefront is as follows: If we assume for simplicity that the denominator in Eq.(4-1) is unity, then the centroid  $x$ -coordinate is

$$\begin{aligned} \bar{x} &= \iint x E(x,y) dx dy \\ &= \int x L(x) dx \end{aligned} \quad (4-2)$$

where

$$L = \int E(x,y) dy \quad (4-3)$$

is the line spread function (LSF) along the  $x$ -axis.

The optical transfer function (OTF) is given by the auto-correlation of the pupil function:

$$\text{OTF}(\xi, \eta) = r[P(\xi, \eta)] \quad (4-4)$$

where  $\xi$  and  $\eta$  are normalized spatial frequencies and  $r$  is the auto-correlation operator. When properly normalized the OTF is the Fourier transform of the PSF. Thus, using the moment theorem, the centroid is given by the first derivative of the OTF at the origin:

$$\bar{x} = \frac{1}{2\pi j} \frac{\delta}{\delta \xi} [\text{OTF}(0,0)] \quad (4-5)$$

Similarly, the partial derivative of the OTF with respect to  $\eta$  gives the  $\bar{y}$ -coordinate of the centroid.

The general pupil function is

$$P(\xi, \eta) = A(\xi, \eta) \exp[jkw(\xi, \eta)] \quad (4-6)$$

where  $A(\xi, \eta)$  is a real aperture function (in our case the primary mirror is the aperture) and  $w(\xi, \eta)$  is the wavefront function, in our case a tilted plane wave with some aberration. The derivative of the OTF can be calculated from the auto-correlation by using the relationship  $(f \otimes g)' = f' \otimes g = f \otimes g'$  which is common to convolution. (An asterisk implies convolution). Thus

$$OTF'(\xi, \eta) = P^*(\xi, \eta) \otimes P'(\xi, \eta) \quad (4-7)$$

Since

$$P'(\xi, \eta) = [A'(\xi, \eta) + jkw'(\xi, \eta)] \exp[jkw(\xi, \eta)] \quad (4-8)$$

we have

$$\begin{aligned} OTF'(\xi, \eta) = & A'(\xi, \eta) \exp[jkw(\xi, \eta)] \otimes P^*(\xi, \eta) \\ & + jkw'(\xi, \eta) P(\xi, \eta) \otimes P^*(\xi, \eta) \end{aligned} \quad (4-9)$$

At the origin, the convolution of Eq.(4-9) reduces to the following

$$OTF'(0,0) = \iint A'(\xi, \eta) A(\xi, \eta) d\xi d\eta + jk \iint A^2(\xi, \eta) w'(\xi, \eta) d\xi d\eta \quad (4-10)$$

The first integral vanishes since the function  $A(\xi, \eta)$  is bounded. Thus the x-axis centroid is given by

$$\bar{x} = \frac{k}{2\pi} \iint A^2(\xi, \eta) w'(\xi, \eta) d\xi d\eta \quad (4-11)$$

where  $k=2\pi/\lambda$ . Note that a normalizing factor is missing in Eq. (4-11), with units of  $(\text{length})^2$ . This factor comes from the coordinate transform of  $(\xi, \eta)$  and does not change the functional relationship between the centroid and the wavefront gradient as presented in Eq. (4-11). This relationship says, in essence, that the centroid of the PSF is proportional to the average tilt of the wavefront at the pupil, weighted by the irradiance distribution at the pupil. The weighting factor is important. It quantifies the intuitive notion that reflectivity changes of the mirror with time can cause a systematic error in determining the image centroids. If, however, the residual wavefront aberrations are small enough, reflectivity has only a second order effect since the wavefront gradient becomes, under this assumption, constant over the whole aperture. The image centroid is, in this respect, a preferred position parameter. Not only is it proportional to the stellar angular position, but it is directly related to a major source of systematic image position error: telescope aberrations. We examine this relationship below, when we discuss the error sources and show how aberration errors can be systematically eliminated.

#### 4.2.2 Analysis of the Moving-Grating Position Sensor

We present here a methodology by which the moving-grating position sensing can be analyzed and the relationship between the image centroid and the observed signal be understood. - Let the grating transmission function be  $g(x, y, t)$ . For a Ronchi grating moving in the  $+x$  direction at constant speed  $s$ , the transmission function is

$$g(x, y, t) = \text{rect}(x/d) \cdot \text{comb}\left(\frac{x-st}{2d}\right) \quad (4-12)$$

The functions in Eq. (4-12) are as follows:

$$\begin{aligned} \text{rect}(x/a) &= 1, \quad -\frac{a}{2} < x < \frac{a}{2} \\ &= 0, \quad \text{otherwise} \end{aligned} \quad (4-13)$$

ORIGINAL PAGE  
OF POOR QUALITY

$$\text{comb}(x/a) = |a| \sum_{n=0}^{\infty} \delta(a-na) \quad (4-14)$$

The graphic representation of Eq.(4-14) is given in Fig. 4-2. The detector signal (normalized) as a function of time is given by the integral over the detector aperture area, A:

$$v(t) = \iint_A g(x,y,t) E(x,y,t) dx dy \quad (4-15)$$

where  $E(x,y,t)$  is the time-dependent PSF irradiance function and includes PSF motion. We assume that the detector, or its image, is centered at the origin of the  $(x,y)$  coordinate system and that at time  $t=0$  the grating is centered as shown in Fig. 4-2. We define a detector aperture function  $a(x,y)$  and write Eq.(4-15) in the form

$$v(t) = \iint_{-\infty}^{\infty} g(x,y,t) E(x,y,t) a(x,y) dx dy \quad (4-16)$$

We have assumed that the detector response does not have a time dependence. This is usually not the case since detectors change their characteristics with age, particularly in a space environment. This potential source of errors will be discussed later.

Since the grating moves at a constant speed, the signal is modulated with a fundamental frequency  $\nu_0 = 2s/d$ . The reticle transmission can be expressed as the Fourier series

$$g(x,y,t) = \sum_{n=-\infty}^{\infty} g_n(x) e^{2\pi j n \nu_0 t} \quad (4-17)$$

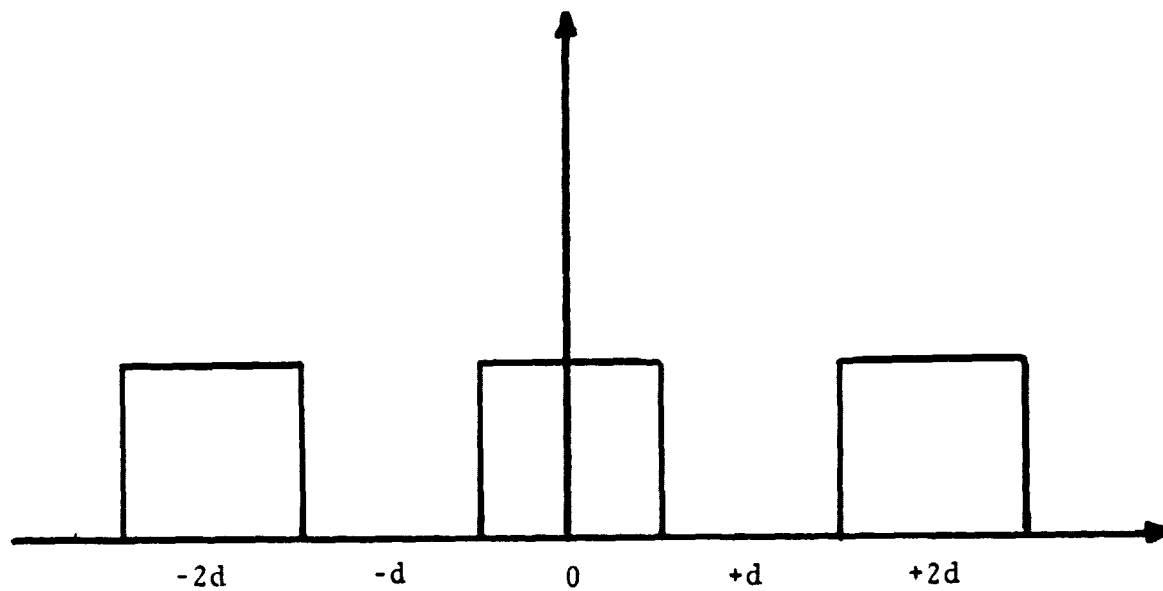


Fig. 4-2 The Function  $\text{comb}(x/d)$

and the detector signal can be thus expressed

$$\begin{aligned}
 v(t) &= \iint_{-\infty}^{\infty} \sum_{n=-\infty}^{\infty} g_n(x) E(x, y, t) a(x, y) e^{2\pi j n v_0 t} dx dy \quad (4-18) \\
 &= \sum_{n=-\infty}^{\infty} \left[ \iint_{-\infty}^{\infty} g_n(x) E(x, y, t) a(x, y) dx dy \right] e^{2\pi j n v_0 t} \\
 &= \sum_{n=-\infty}^{\infty} v_n(t) e^{2\pi j n v_0 t} \quad (4-18)
 \end{aligned}$$

The signal therefore consists of a sum of carriers at frequencies  $n v_0$  modulated by  $v_n(t)$ , where  $v_n(t)$  is a function of the PSF temporal behaviour:

$$v_n(t) = \iint_{-\infty}^{\infty} g_n(x) E(x, y, t) a(x, y) dx dy \quad (4-19)$$

which does not represent a Fourier series because  $v_n$  is time-dependent.

Equ.(4-19) can be investigated in the spatial frequency domain by using Parseval's Theorem. The modulation function  $v_n(t)$  can be expressed as

$$v_n(t) = \iint_{-\infty}^{\infty} G_n^*(\xi) \left[ \text{OTF}(\xi, n, t) ** A(\xi, n) \right] d\xi \quad (4-20)$$

where  $G_n(\xi)$  is the Fourier transform of  $g_n(x)$ ;  $\text{OTF}(\xi, n, t)$  is the optical transfer function of the system given by the normalized Fourier transform of the PSF; and  $A(\xi, n)$  is the transform of the detector's spatial response. For the Ronchi grating we have



ORIGINAL PAGE IS  
OF POOR QUALITY

$$\left. \begin{aligned} g_0(x) &= 1/2 \\ g_{2n+1}(x) &= \frac{1}{(2n+1)\pi j} e^{(2n+1)\pi x/d} \\ g_{2n}(x) &= 0 \end{aligned} \right\} \quad (4-21)$$

and

$$\left. \begin{aligned} G_0(\xi) &= (1/2)\delta(0) \\ G_{2n+1}(\xi) &= \frac{1}{(2n+1)\pi j} \left( \xi - \frac{2n+1}{2d} \right) \\ G_{2n}(\xi) &= 0 \end{aligned} \right\} \quad (4-22)$$

where  $n=\pm 1, \pm 2, \dots$ . We find that the modulation  $v_n(t)$  of the carrier frequency  $n\nu_0$  is zero for even  $n$  and for odd  $n$  is given by

$$v_n(t) = \frac{1}{j\pi n} \left[ \text{OTF}(\xi, n, t) \star \star A(\xi, n) \right]_{\substack{\xi=n/2d \\ n=0}} \quad (4-23)$$

Several important conclusions can be drawn from this analysis. The basic signal, as expressed in Eqs.(4-18) and (4-19), includes the contribution of three functions: the grating function, the detector function, and the function of interest - the PSF. Any time dependent or field dependent variations in the grating and detector functions contribute directly to the measurement error. The signal consists of modulated carriers of odd harmonics of the modulation frequency. Any signal processing scheme which relies on the fundamental component only (for example, phase detection) is not optimal and not accurate. The inaccuracy is obvious from Eq.(4-19) which shows that the modulating function  $v_n(t)$  is field-dependent since  $E(x, y, t)$  is dependent on the field.

### 4.3 Algorithms for Signal Processing

Several algorithms and signal processing schemes were investigated. They include phase detection algorithms, correlation techniques, a centroid integrator, and N-bucket integrators. The main purpose of the investigation was to identify basic limitations of the various schemes and in particular to estimate the sampling bandwidth requirements since these have major implications for the detector. The ideal algorithm should be optimal (from a signal-to-noise point-of-view), free of systematic biases due to field-dependent aberrations, and compatible with the spatial/temporal resolution capabilities of the detector system. As can be expected, the three desired features cannot be obtained simultaneously and compromise must be found among them by trade-off studies.

#### 4.3.1 Correlation Algorithms

Correlation algorithms relate the received signal to a stored reference signal and then detect the peak of the correlation. The mathematical correlation operation is defined as  $C(\tau) = \int S(t)r(t-\tau)dt$  where  $S(t)$  is the signal and  $r(t)$  the reference. In practice, the signals are sampled and quantized and the operation is of the form

$$C(\tau) = \sum_{i=1}^n W_{\tau}(i)S(i) \quad (4-24)$$

where  $W_{\tau}$  is a weighting function and  $S(i)$  is the sampled signal. The accuracy of the correlation algorithm is a function of the a priori knowledge of the form of  $S(t)$ , the number of samples in the sum, and, of course, the noise associated with the measurement of  $S(t)$ . Some phase-detection algorithms are a subset of the correlator. For example, a lock-in amplifier is an analog correlator. Numerical estimation of the phase of sinusoidal signals with known period can be performed by integrating the periodic signal on the detector into N-buckets during a period. If the integration intervals are designated  $S_1, S_2$ , etc. the following examples show algorithms for

phase detection with 4 or 8 buckets:

$$N=4 \quad \tan \phi = \frac{S_1 - S_3}{2S_2 - (S_1 + S_3)} \quad (4-25)$$

or

$$\tan \phi = \frac{S_1 - S_3}{S_2 - S_4} \quad (4-26)$$

$$N=8 \quad \tan \phi = \frac{S_1 - S_4 - S_5 + S_8 + 0.41(S_2 - S_3 - S_6 + S_7)}{S_2 + S_3 - S_6 - S_7 + 0.41(S_1 + S_4 - S_5 - S_8)} \quad (4-27)$$

These algorithms can be performed with a relatively small number of samples during a period. They are limited, however, in their accuracy by the variation in the PSF shape as noted above. They can be useful for processing the signals from a star in the center of the FOV where the effects of aberrations are minimal.

A general correlation function can be used over the full field if the reference signal variations with field angle can be calculated or calibrated by experiment. Such an algorithm, however requires fine sampling of  $S(t)$  resulting in a low measurement bandwidth.

#### 4.3.2 Centroid Integrator

The centroid integrator algorithm converts the total energy collected by a detector (the total photon count) directly into a measure of the image centroid. Consider the geometry of Fig. 4-3, which shows a knife-edge scanning an image distribution  $E(x,y)$  at a constant velocity,  $s$ . The power on the detector which collects the passing light is given by the integral

$$S(t) = \int_{x(0)}^{x(t)} dx \int dy E(x,y) \quad (4-28)$$

ORIGINAL PAGE IS  
OF POOR QUALITY

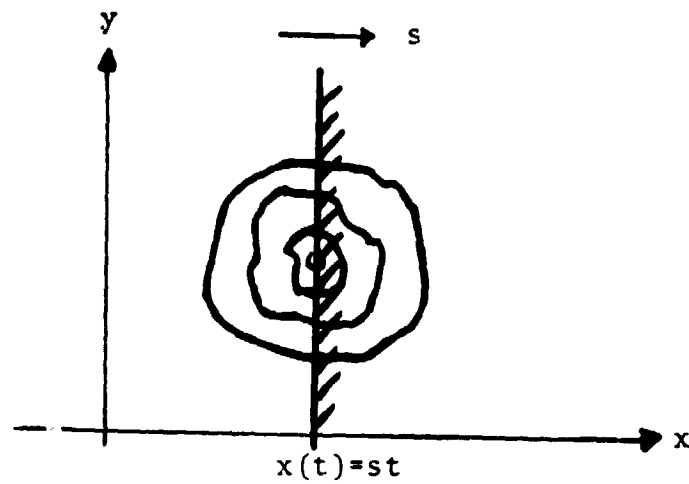


Fig. 4-3 Centroiding with Knife Edge

The derivative of the integral is

$$S'(t) = \frac{dx}{dt} \int E(x,y) dy \quad (4-29)$$

and the image centroid is

$$\bar{x} = \frac{\int_{-\infty}^{\infty} \int_{-\infty}^{\infty} x E(x,y) dx dy}{\int_{-\infty}^{\infty} \int_{-\infty}^{\infty} E(x,y) dx dy} \quad (4-30)$$

If we assume that the aperture (i.e. the grating line spacing) is wide enough, then at time T when the full image is exposed

$$S(T) = \int_{-\infty}^{\infty} \int_{-\infty}^{\infty} E(x,y) dx dy \quad (4-31)$$

and

$$\bar{x} = \frac{s}{S(T)} \int_0^T t S'(t) dt \quad (4-32)$$

where we assume

$$x(t) = s \cdot t \quad (4-33)$$

Integration by parts yields

$$\bar{x} = sT - \frac{s}{S(T)} \int_0^T S(t) dt \quad (4-34)$$

The integral in this expression is the total integrated energy (photon count) on the detector between  $t=0$  and  $T$ . The reference window  $(0,T)$  has to be well known. The position of the star in the field is thus composed of the position of the grating line at  $t=0$  plus the term  $\bar{x}$  given by Eq.(4-34). The term  $S(T)$  is the power of the star and is obtained from the average of many frames.

The main disadvantage of the centroid integrator is that it requires a relatively large spacing of the grating lines in order to minimize systematic measurement errors which arise from "clipping" of the edges of the PSF. It is possible, however, to refine this algorithm by sampling the signal several times during a period and generating in effect a measurement window which is adjusted to the relative position of the star in the frame. This allows a reduction of the width of the grating lines and improves the efficiency of the algorithm. The algorithm has several definite advantages:

1. It is directly related to the image centroid.
2. It can be performed with as few as one detector reading per period and requires very few computations.

#### 4.4 Focal Plane Architecture and Detectors

The baseline scenario for the astrometric telescope calls for simultaneous position measurements of a large number of stars ranging in magnitude from a bright target star ( $m=7$ ) to faint reference stars ( $m=20$ ). The star population and photon rates are summarized in Table 4-1. It is immediately apparent that the detector system faces a challenging task:

- spatial resolution of the order  $10^3 \times 10^3$  pixels
- temporal bandwidth of greater than 10 Hz
- dynamic range of better than  $10^5$ .

The spatial resolution requirement results from the need to match the pixel size to approximately the image size, in order to maximize the SNR. The temporal bandwidth requirement is driven by the need to average a large number of frames to achieve the required accuracy. The exact detector requirements depend on several design features

TABLE 4-1 STAR POPULATION AND PHOTON RATES

<u>Magnitude</u>	<u>Photon Rate (<math>\text{m}^{-2} \text{s}^{-1}</math>)</u>	<u>Average No. in FOV</u>	<u>Total Photon Rate (<math>\text{m}^{-2} \text{s}^{-1}</math>)</u>
7.3 (target)	$4 \times 10^7$	--	$4 \times 10^7$
13 (reference)	$2 \times 10^5$	4	$8 \times 10^5$
15 "	$3 \times 10^4$	25	$7 \times 10^5$
17 "	$5 \times 10^3$	120	$6 \times 10^5$
19 "	$8 \times 10^2$	440	$3 \times 10^5$
21 "	$1 \times 10^2$	1400	$1 \times 10^5$

like the algorithm, the grating line spacing, and the telescope configuration and the FOV discussed later.

The requirements as stated above rule out the adaption of the detection techniques used with the ground-based astrometric instruments like the individual photomultipliers used by Gatewood or the image dissecting tube used by Jones. Such large spatial resolution and parallel photon integration can be obtained only by large area silicon detector arrays, like the charge-coupled (CCD) or charge-injected (CID) devices. There are two basic options in employing these detectors. One is direct detection - the usual way these devices are used. The other is intensified detection, whereby the silicon array is used in conjunction with an image intensifier tube. The main difference in performance is that the direct detection has better quantum efficiency and dynamic range, while the intensified detection has lower noise.

In order to compare the detectors let us assume that the CCD detector has quantum efficiency  $Q_1$  and readout noise  $C$  electrons per pixel. Then the signal from  $N$  photons is

$$S_1 = NQ_1 \quad (4-35)$$

and the noise is

$$n_1 = (NQ_1 + C^2)^{1/2} \quad (4-36)$$

The gain of the intensified detector is such that no readout noise is present and with quantum efficiency  $Q_2$  the signal is

$$S_2 = NQ_2 \quad (4-37)$$

The noise is only the photon noise



$$n_2 = (NQ_2)^{1/2} \quad (4-38)$$

The CCD is better when  $S_1/n_1 > S_2/n_2$ , which results in

$$N > (Q_2/Q_1)C^2/(Q_1 - Q_2) \quad (4-39)$$

Thus for photon counts above a certain threshold  $N$  the CCD without intensification is better than the intensified sensor. Fig. 4-4 plots this threshold level as a function of the CCD readout noise for quantum efficiency ratios ( $Q_1/Q_2$ ) ranging from 2 to 6. Cooled CCDs (charge-coupled devices) can achieve less than 20 noise electrons per pixel, at quantum efficiencies approaching 50%, which is 2 to 5 times better than the integrated quantum efficiency of photocathodes. A comparison of attainable SNR for two cases with different assumptions is presented in Table 4.2: Case A favors the CCD and results in equivalent SNR at 50 photons while Case B, which assumes less favorable parameters for the CCD, has equivalent SNR at about 500 photons.

The implication of the above comparison on the problem at hand is that at low measurement bandwidth (long integration times) the CCD is superior. This is demonstrated in Fig. 4-5 which plots the bandwidth for equivalent SNR as a function of stellar magnitude, assuming an optical efficiency of 20% for the system. In the region below the lines which represent cases A and B the CCD is superior in SNR to the intensifier. For bandwidth of 10 Hz this occurs at about 18.6 magnitude for case A, and 16.2 magnitude for case B.

Dark current, which is a potential noise source in silicon detectors, is eliminated by cooling the device. Fig. 4-6 shows empirical plots of noise electrons/s due to dark current as a function of temperature for characteristic leakage current densities ranging from 1 to 12

ORIGINAL PAGE IS  
OF POOR QUALITY

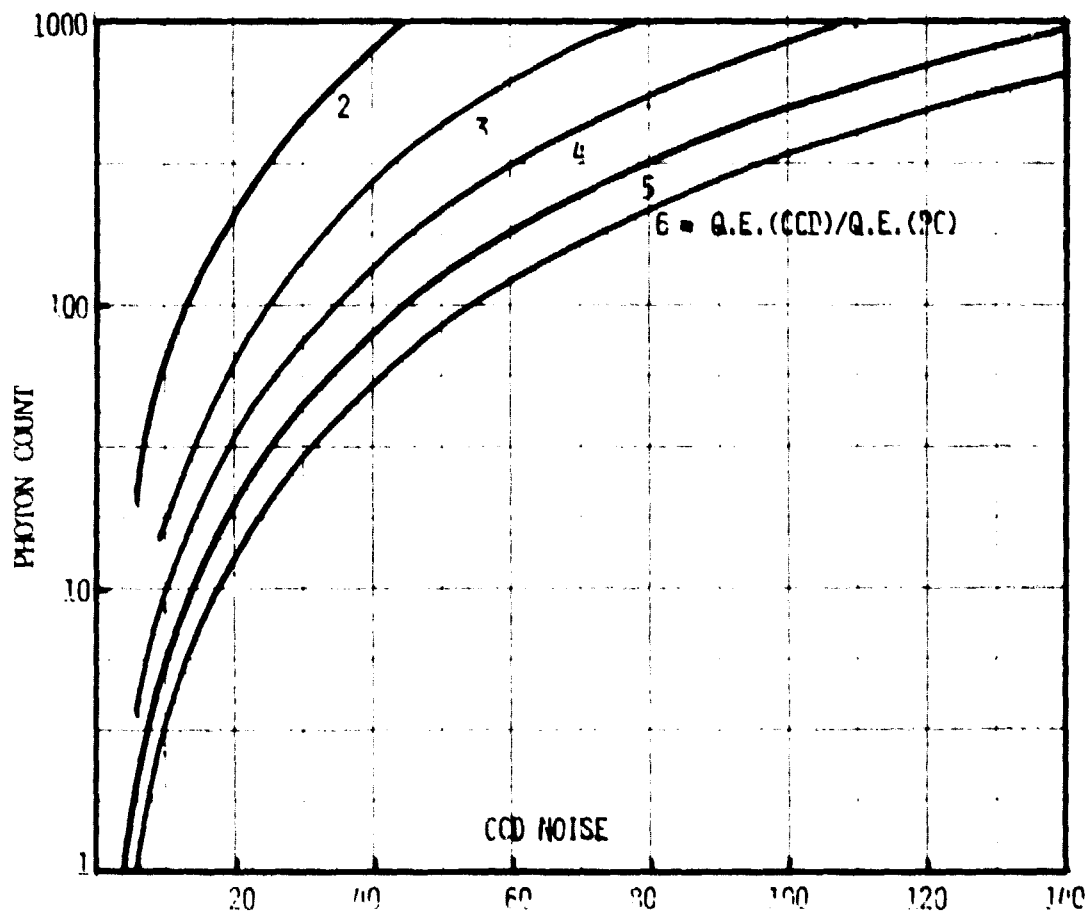


Fig. 4-4 Counts/Pixel at which CCD is better than PMT

TABLE 4-2

PMT VS. CCD - AN EXAMPLE

CASE	A	R
CCD QE ( $Q_1$ )	0.5	0.5
CCD NOISE (C)	10	20
PMT QE ( $Q_2$ )	0.1	0.2
	SNR :	
AVAILABLE PHOTONS	<u>CCD</u>	<u>PMT</u>
10	0.49	1.0
50	2.24	2.24
100	4.08	3.16
500	13.16	7.07

ORIGINAL PAGE IS  
OF POOR QUALITY

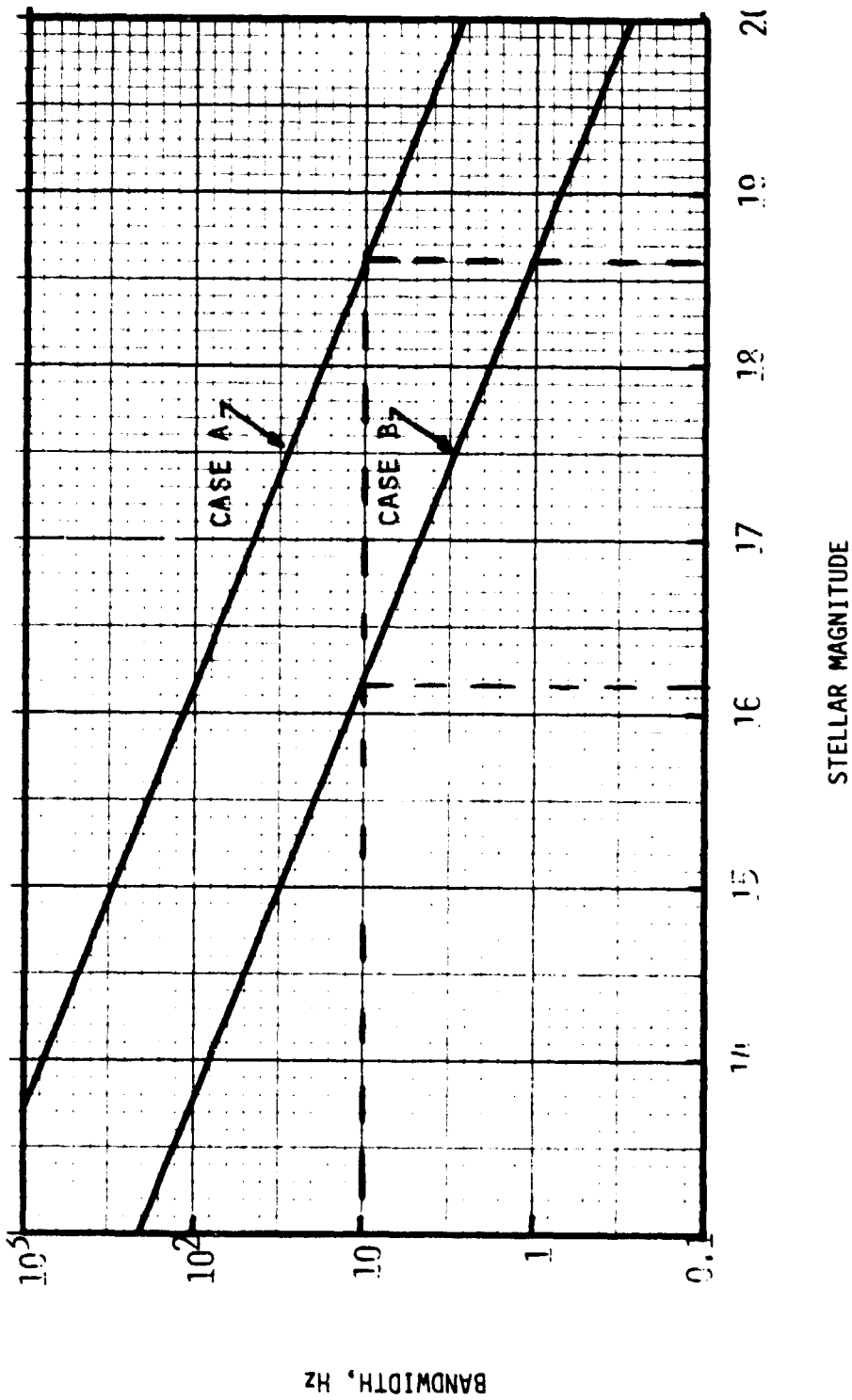


Fig. 4-5 Maximum Bandwidth for which CCD is Superior

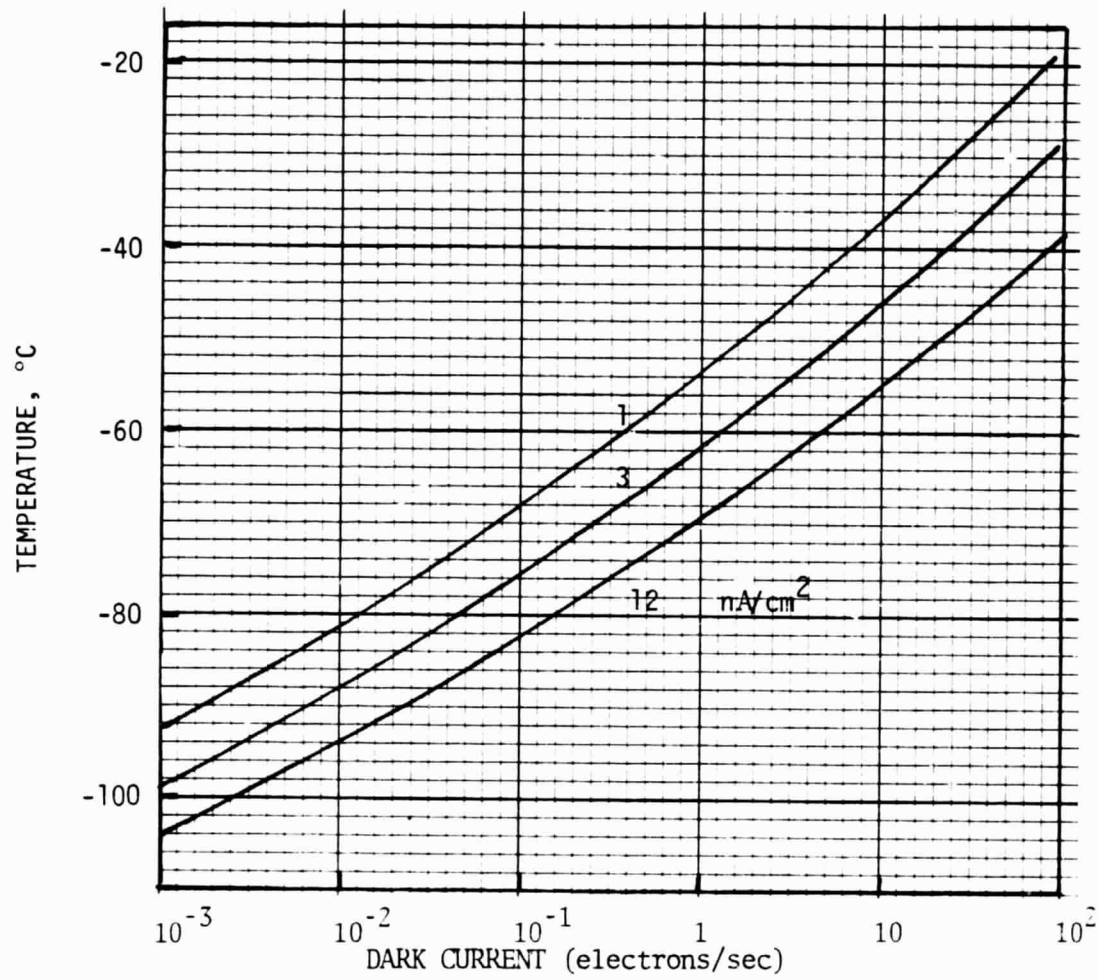


Fig. 4-6 Dark Current Generation

$\text{nA/cm}^2$ . These values are typical for buried channel CCDs like the one developed for the Space Telescope. It can be seen that at 200K the rate is less than 1 electron/s - negligible when compared to the readout noise of 10-20 electrons/pixel of these devices.

While CCD detectors can be operated at serial readout rates as high as  $2 \times 10^7$  pixels/s, low noise operation is limited to a rate of  $10^6$  pixels/s. We can estimate the temporal bandwidth attainable with this readout rate. Assume that the FOV is  $10' \times 10'$  and the telescope aperture has a diameter of  $D=1\text{m}$ . The Airy diameter is then  $1/4$  arcsec and if we assume that the required detector resolution is somewhere between a minimum of  $1/4$  of the Airy diameter to 4 Airy diameters, the total number of pixels in a frame ranges from  $3.6 \times 10^5$  to  $9.2 \times 10^7$ . The temporal resolution under these assumptions is plotted in Fig. 4-7. The figure shows the one-dimensional array size as well as the frame readout rate assuming serial readout or a 16-channel parallel readout. Since the largest arrays being developed have 1024 pixels on a side, a focal plane architecture which allows parallel readout is required. Parallel detection is possible by optically splitting the image plane on separate detectors and by employing detectors which are designed with a multitude of parallel outputs.

#### 4.5 Grating and Grating Drive

The grating is another critical component in the measurement system. It is constructed of a slab of transparent material, as wide as the image field and as long as is practically possible. The grating is deposited on the front surface of the slab by conventional thin film techniques. The main issues regarding the grating are the material stability and the stability of the drive system.

ORIGINAL PAGE IS  
OF POOR QUALITY

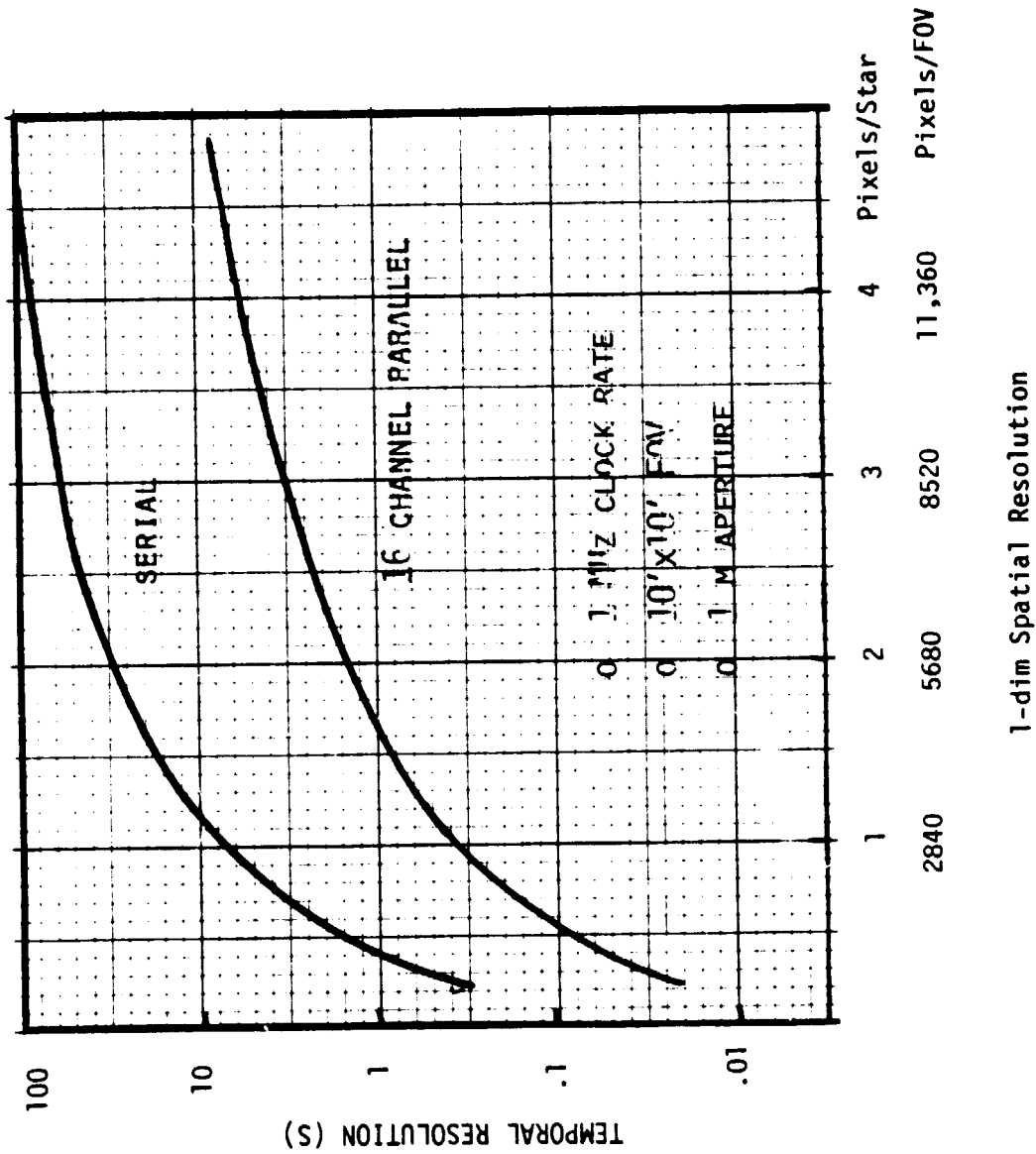


Fig. 4-7 Temporal Resolution Obscured with Large Area CCD

#### 4.5.1 Grating Material Considerations

The grating material is required to be of excellent optical quality, homogeneous and, most of all, exhibit minimal variation in its coefficient of thermal expansion. The favored materials are fused silica and ULE, which is 7% titanium silicate glass. Fused silica has zero coefficient of expansion at about 140K, and for ULE this point is at 300K. It should be noted that the soak temperature of the focal plane assembly might be substantially lower than room temperature. At 200K, for example, ULE has an expansion coefficient of  $\alpha = -0.2 \times 10^{-6} \text{K}^{-1}$ , which is comparable to fused silica. At 300K,  $\alpha = 0.56 \times 10^{-6} \text{K}^{-1}$  for fused silica.

An important consideration in material selection is the homogeneity of  $\alpha$ . Since uniform expansion of the grating translates into a scale change, which can be calibrated out of the data, it is the spatial variations of  $\alpha$  which will degrade the performance of the sensor. In this respect fused silica is much better than ULE. According to Barnes\*, the total variation of  $\alpha$  is  $5 \times 10^{-9} \text{K}^{-1}$  for fused silica and  $15 \times 10^{-9} \text{K}^{-1}$  for ULE. Fused silica has also more favorable thermal diffusivity and conductivity, which helps minimize thermal gradients. It can be concluded that fused silica is the preferred material for the grating.

To evaluate the thermal effects, assume that we encounter the full excursion in  $\alpha$  of  $5 \times 10^{-9} \text{K}^{-1}$  over a linear FOV of 5 cm. The non-linear thermal expansion can be thus estimated:

$$\frac{dx}{dT} \approx \Delta \alpha \Delta x \quad (4-40)$$

---

\* W.P. Barnes, Jr., Chapter 4 in "Applied Optics and Optical Engineering" Vol. 7, R.R. Shannon and J.C. Wyant, eds. (Academic Press, 1979)



TABLE 4-3  
THERMAL PROPERTIES OF FUSED SILICA AND ULE

	Fused Silica	ULE
$\alpha$ ( $10^{-6}K^{-1}$ ) at 300K	0.56	$0 \pm 0.03$
$\alpha$ ( $10^{-6}K^{-1}$ ) at 140K	0	
$\alpha$ homogeneity ( $10^{-9}K^{-1}$ )	5	15
Specific heat (J/kg.K)	741	766
Conductivity (W/m.K)	1.37	1.31
Diffusivity ( $10^{-6}m^2/s$ )	0.840	0.777

$$\begin{aligned}
 &= (5 \times 10^{-9}) \times (5 \times 10^{-12} \text{ m}) \\
 &= 2.5 \times 10^{-10} \text{ m} = 2.5 \text{ \AA}
 \end{aligned}$$

Thus we arrive at a thermally induced dimensional variation of 2.5 Å/K spread over the full FOV. Even if the error was correlated over the whole area, it still agrees with the required accuracy, since a temperature gradient of less than 0.2 Å/K in fused silica can surely be maintained.

#### 4.5.2 Grating Drive

The best candidate for the grating drive mechanism is a magnetic bearing linear motor assembly. This technology is being developed for precision machining of optical surfaces and is at an advanced state of maturity.\* The technique uses magnetic fields to suspend the moving parts between a set of rails. An axial drive force is generated by applying currents to a control coil on the moving part. Since there is no mechanical contact between the rails and the grating, any vibrations in the support structure can be greatly attenuated. Highly accurate control of the grating can be obtained by closed loop control of the driving currents. Using a laser interferometer position sensor, accuracies of better than 80 nm at driving speeds from zero to 10 cm/min have been reported.\* The accuracy was essentially limited by the laser interferometer: when the resolution of the interferometer was extended by a factor of 30, the linear drive system resolution was measured as better than 8 nm. There is no doubt that in the acoustically benign environment of space the grating motion can be even better stabilized. Space operation has another advantage: the weightless grating assembly can be supported by weak magnetic fields. Relatively large forces may be required only when the direction of motion is reversed; but the average driving power is very small.

#### 4.5.3 Active Grating Position Control

In addition to motion stabilization and vibration attenuation, functions which are performed by the magnetic drive assembly, it is necessary to accurately monitor the position

---

\* Barkman, W.E. 1978. "The Linear Motor Slide Drive System,"  
Proc. SPIE 159, p. 25

of the grating relative to the optical axis of the primary mirror so that slow position drifts can be sensed. The source of such drifts can be thermal dimensional instability and electronics drift. A convenient laser position sensing scheme is described in Fig. 4-8. The distance from reference surfaces on the rim of the mirror to retroreflectors on the grating assembly is measured. The distance measuring interferometer is a variation on the proven Hewlett-Packard interferometer technology and allows the use of a single laser with multiple sensors. This arrangement allows absolute positioning of the grating assembly in the focal plane to sub-wavelength accuracies.

#### 4.6 Optical Form

Several optical forms were evaluated, single element as well as two-mirror designs. The forms included the parabola, a Rosin system (parabola and refractive corrector near the focus), off-axis parabola, a Schmidt system, and a super-achromat doublet. The system performance was studied with the ACCOS V lens-design computer program. An immediate conclusion was that refractive elements are not uniform and stable enough to maintain the extreme accuracies required over the mission duration (5 years). Using data for the variation of the index of refraction with temperature and for the effects of radiation and aging (cf. also Fig. 2-4) we found that the induced errors are several orders of magnitude greater than the measurement goal. Thus refractive systems, which are corrected for coma, are precluded in this application. Next, an off-axis parabola was compared with a centered system. PSF analysis showed that the off-axis coma enlarges the PSF more than the central obscuration of the centered system. The off-axis system is also disadvantageous concerning size and weight. Thus we did not identify a system better than the parabola.

ORIGINAL PAGE 13  
OF POOR QUALITY

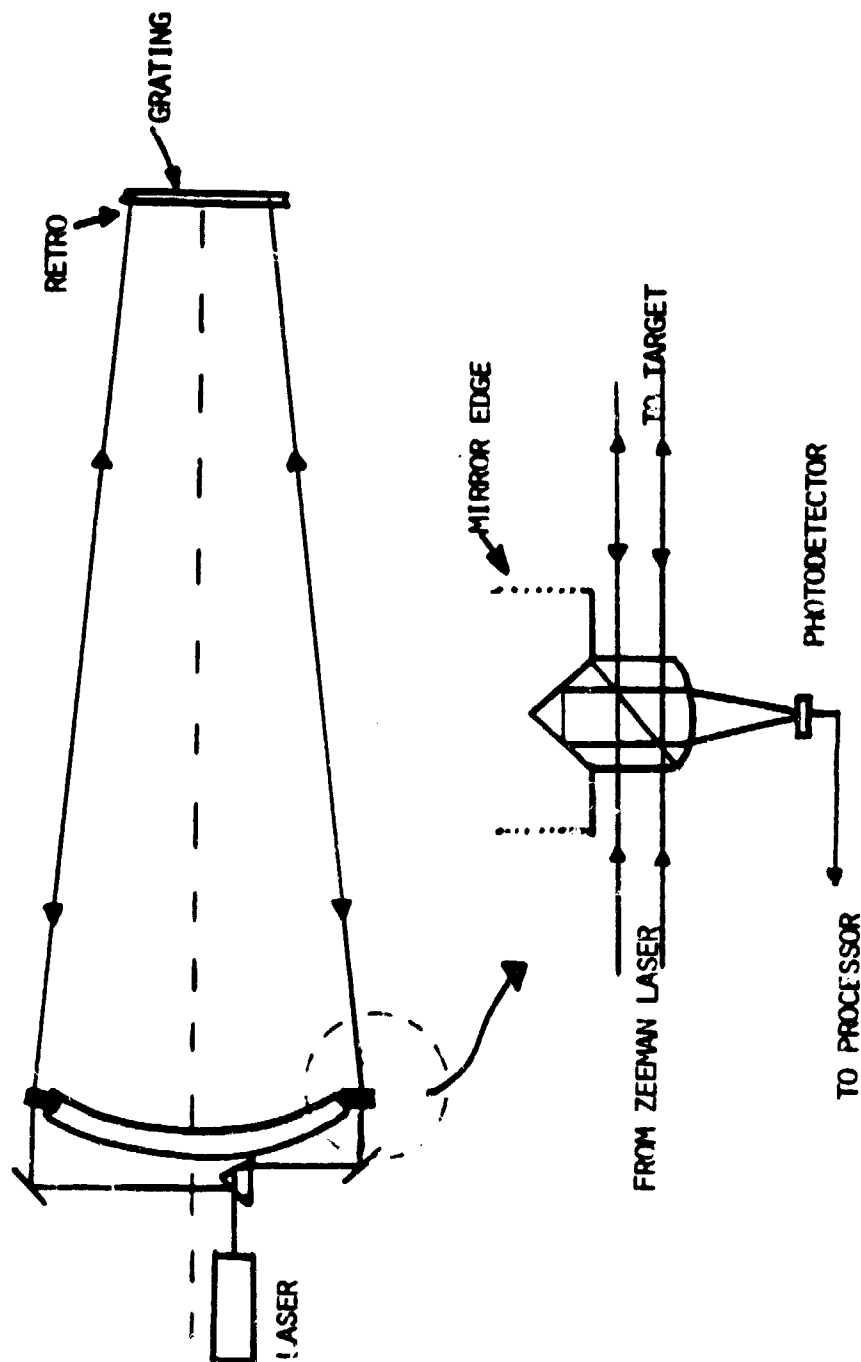


Fig. 4-8 Active Laser Position Sensor

#### 4.6.1 Evaluation of Optical Performance

Evaluation of the optical performance of the parabola using ray tracing included the following items:

- Centroid shift due to aberrations
- Radial energy distribution
- Variation of spot size across the FOV

Centroid shift due to aberrations can be a source of systematic errors. The theory predicts that the centroid shift is proportional to the average wavefront gradient. Coma, which is the major aberration in our case, has a gradient which linearly increases with field angle. The centroid shift due to coma is

$$\Delta x = \frac{x_0}{16f_{\#}^2} \quad (4-41)$$

where  $x_0$  is the field position. For an f/16 telescope, at the edge of a 10'x10' FOV,  $\Delta x = 0.073$  arcsec. We searched for a non-linear gradient dependency on the field, using 20 field points and 1000 ray traces for each. The centroids followed a linear curve limited by the ray-trace accuracy of about  $10^{-5}$  arcsec.

The radial energy distribution analysis compared the diffraction limited PSF to the aberrated PSF. Fig. 4-9 shows the radial energy distribution for the f/16 mirror at full field (5'). The geometric energy distribution indicates that more than 98% of the rays fall within the Airy disk. Obviously, in this case diffraction dominates. Fig. 4-10 compares the energy distribution due to diffraction and aberrations across the field for a f/16.5 parabola. The Airy diameter of a 1 m mirror is indicated as well as the radial energy distribution due to diffraction (the upper axis is used in this plot). The variation of the 100% and 90% encircled energy points across the field are indicated along with the rms spot size (the lower axis is used

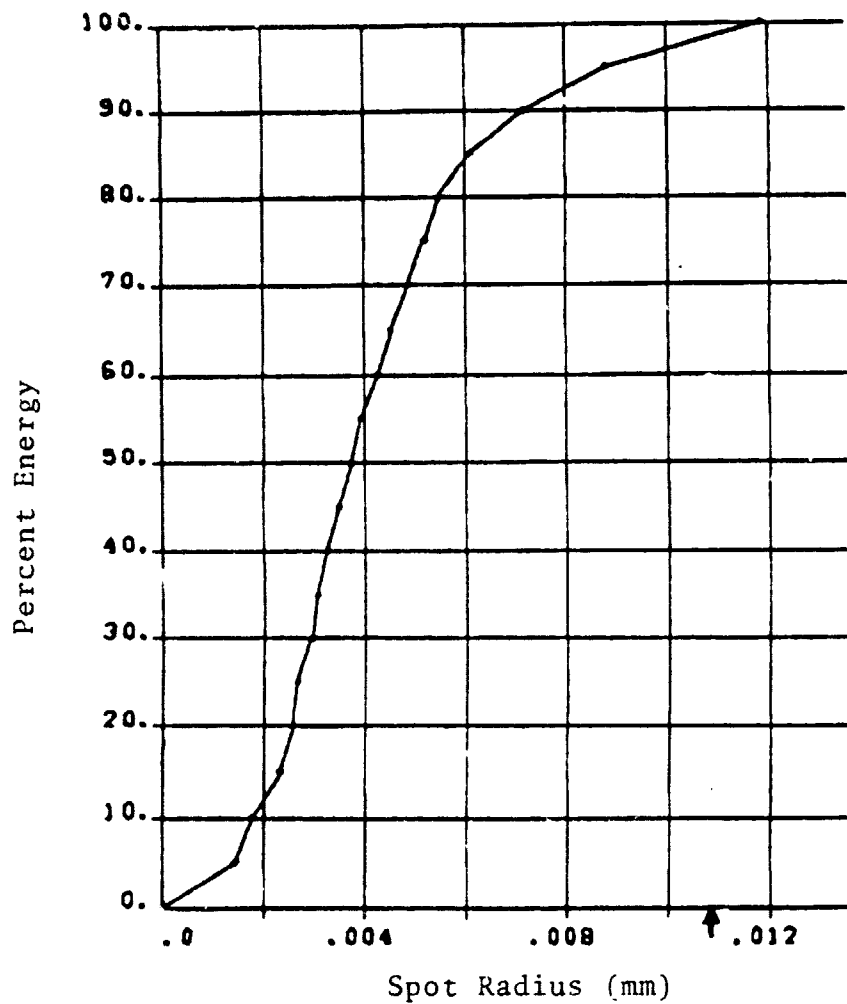


Fig. 4-9 Radial Energy Distribution, 1 m,  
f/16 parabola. Arrow indicates  
Airy radius at 0.55 μm wavelength

ORIGINAL PAGE IS  
OF POOR QUALITY

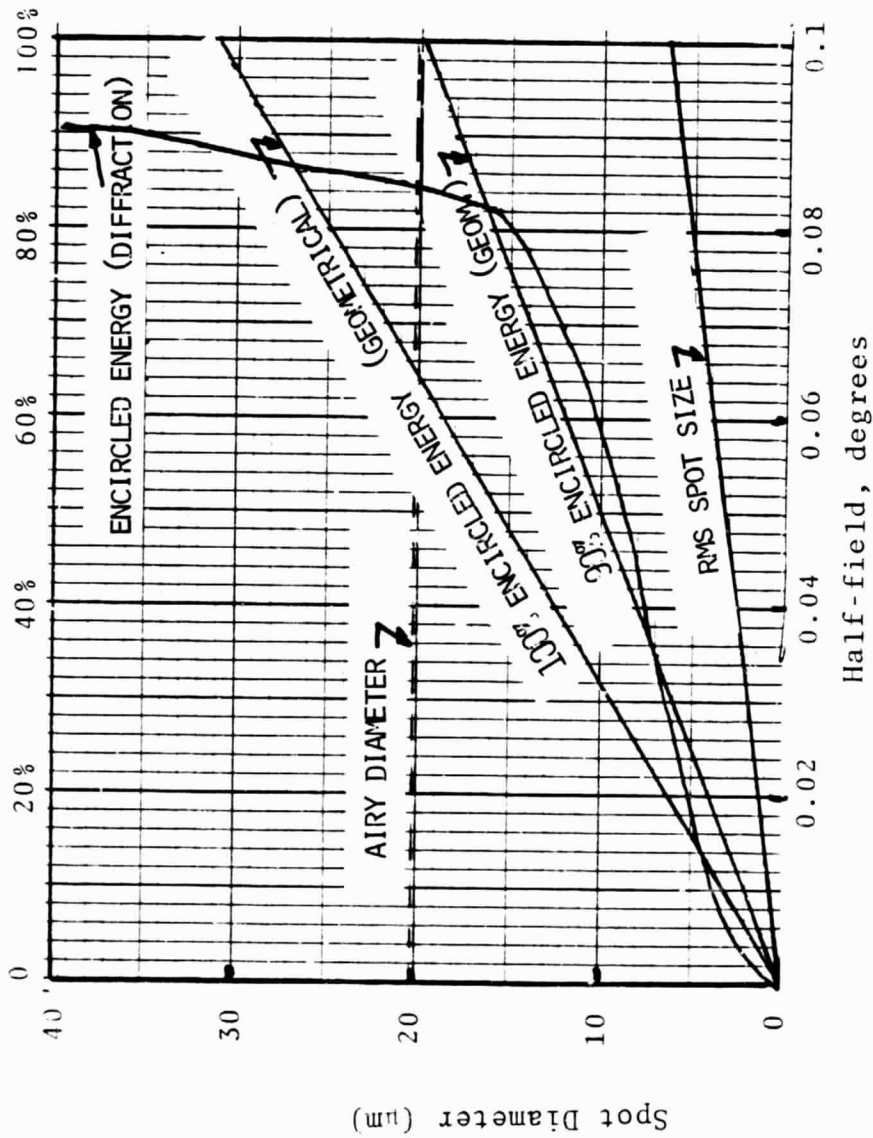


Fig. 4-10 Radial Energy distribution, RMS Spot Size Dependency on Field Angle (F/16.5 Parabola, 1 m diameter)



here). It is apparent that this system is diffraction limited. Since the theoretical limit on the position measurement accuracy depends on the spot size, it is interesting to compare the rms spot size of the diffraction limited PSF and the aberrated PSF. The results are shown in Table 4-4 for  $f/16$ ,  $f/8$  and  $f/4$ , 1 m diameter parabolas. Note that the spot size scales as  $f_{\#}^{-2}$ . The comparison is presented for the full 5' field point and for 0.707 of full field, which is the median of the star field distribution. The calculations assume a flat field and paraxial focus. Shifting to best focus at 0.707 field will improve the spot size slightly. The results show that the  $f/16$  is indeed diffraction limited. The spot size of the  $f/8$  system increases by a factor of 1.2 at .707 field and by a factor 1.7 at full field. The  $f/4$  system is dominated by the aberrations, which increase the rms spot size almost 7 times at full field.

#### 4.7 Focal Plane Assembly

The focal plane assembly (FPA) includes the grating, the relay optics, and detectors. A conceptual architecture which allows deployment of parallel detectors is described here. This concept is by no means the best solution but rather indicates how problems arising from detector technology limits can be overcome. The concept is illustrated in Fig. 4-11. It shows a relay lens imaging the grating plane on a glass prism. The prism transmits the center of the image and focuses the transmitted light on a detector. The rest of the field is split by the prism, reflected and relayed to imaging detectors. This arrangement accomplishes the following:

1. The target star, which is at the center of the FOV, is detected by a fast, large dynamic range detector. The high SNR signal can be used for high position measurement, supplying an accurate reference signal for controlling the grating motion. An  $m=7.3$  target star produces a

ORIGINAL PAGE IS  
OF POOR QUALITY

LMSC-D870885

TABLE 4-4  
RMS SPOT SIZE FOR A 1 M DIA. PARABOLA  
(arcsec)

	F No.	16	8	4
Field	1	0.0602	0.2399	0.9622
	0.707	0.0424	0.1694	0.6801
Diffraction limit		0.14	0.14	0.14

ORIGINAL PAGE IS  
OF POOR QUALITY

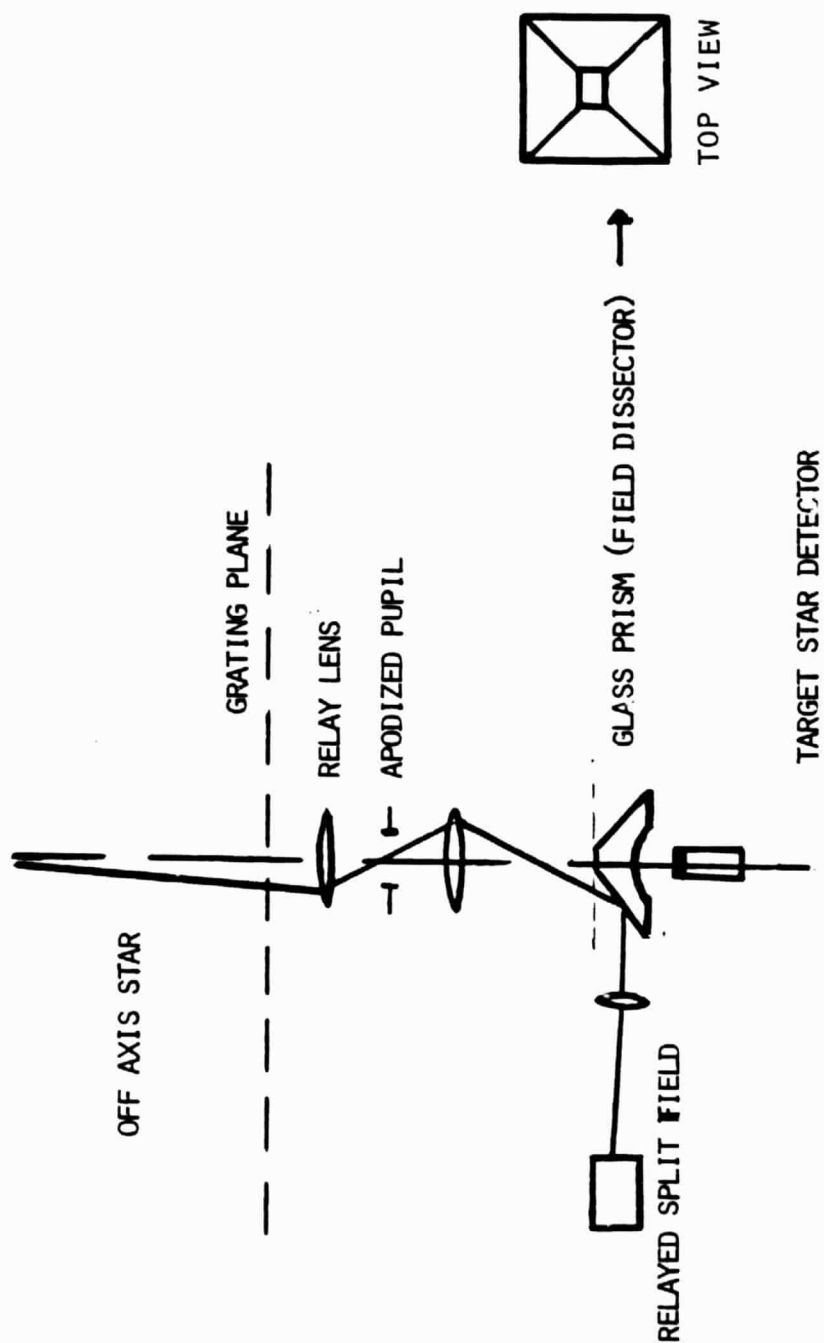


Fig. 4-11 Split-Field Focal Plane

count rate of  $4 \times 10^6$  photons/s (at 10% total system efficiency) with a photon-noise limited position accuracy of  $28 \times 10^{-6}$  arcsec at 1 Hz.

2. The separation of the target star onto a dedicated detector reduces the dynamics range requirements significantly. Assuming reference stars ranging from 13 to 21 magnitude, a dynamic range of 2000 only is required, instead of  $10^6$ .
3. The multiplicity of detectors reduces the demanding spatial resolution requirements and increases the temporal resolution.
4. The relay lens provides also a relayed pupil. This pupil can be apodized by a mask which matches the shape of the obscuration caused by the focal plane assembly. There is therefore no need for a cumbersome shade on the primary mirror to block the area of the aperture which is not common to all stars.

#### Grating Configuration

The construction of the grating was discussed earlier. Here we discuss the grating line configuration regarding two aspects of the design: the orientation of the lines and their separation.

The instruments of Gatewood and Jones use gratings which are oriented perpendicular to the direction of motion. In this mode of operation, measurements are conducted along a certain axis (x) and then the grating or the whole apparatus is rotated in order to obtain position measurements along the y-axis. For a space-borne system this raises some problems:

1. Rotation of the FPA is complex and risky, and rotating the whole telescope is wasteful both in energy and observation time.

2. Cross-coupling between the x-y coordinates will occur since the accuracy to which the axes can be established is several orders of magnitude away from the required measurement accuracy. The cross-coupling effects can be accounted for by data processing, but an error will occur if the star field position varies substantially during the elapsed time between x and y measurements.

These problems can be alleviated in at least two ways. A double-barrel telescope, which uses two identical telescopes side-by-side, has the best potential performance. This concept, which is attractive in many ways, is discussed later. The other concept uses a grating with lines at  $45^\circ$  to the direction of motion. The line inclination changes by  $90^\circ$  every so often, as illustrated by Fig. 4-12. The crossed grating still performs position measurements in an axis perpendicular to the grating lines. The relative motion of a star image consists of motion along the grating line, which causes no modulation, and motion perpendicular to the lines, which gives the modulation, as before with the simple grating. The measurement axis switches as the star image switches between the  $+45^\circ$  and  $-45^\circ$  lines. The penalty paid because of the "dead" zones in-between is relatively small. The gain is considerable: there is no need to rotate the telescope or the grating, and the elapsed time between x and y measurements is only a fraction of the integration time.

The line separation is a parameter which has considerable implication on the measurement accuracy. The optimal separation is dependent on the image size and on the position information retrieval algorithm. The measurement accuracy depends on the modulation depth which increases as the line separation increases. On the other hand, the background noise contribution also increases (relative to the signal), as the photon collecting area (which should match the line separation) increases. As a result, a trade-off exists between noise and

ORIGINAL FIGURE IS  
OF POOR QUALITY

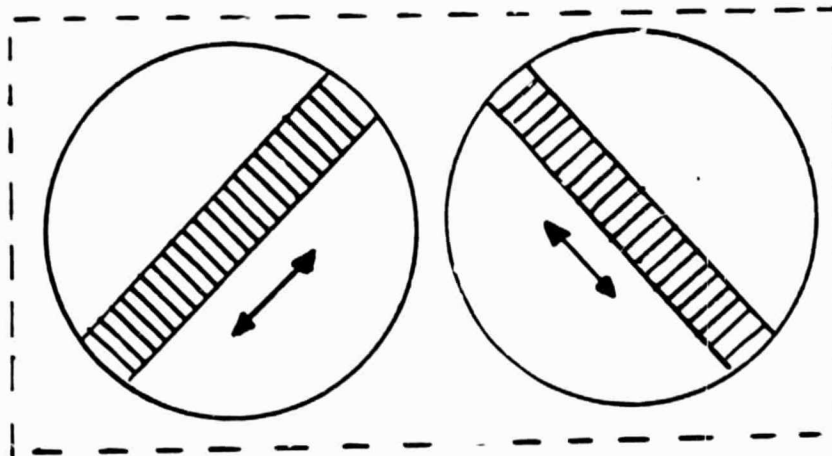
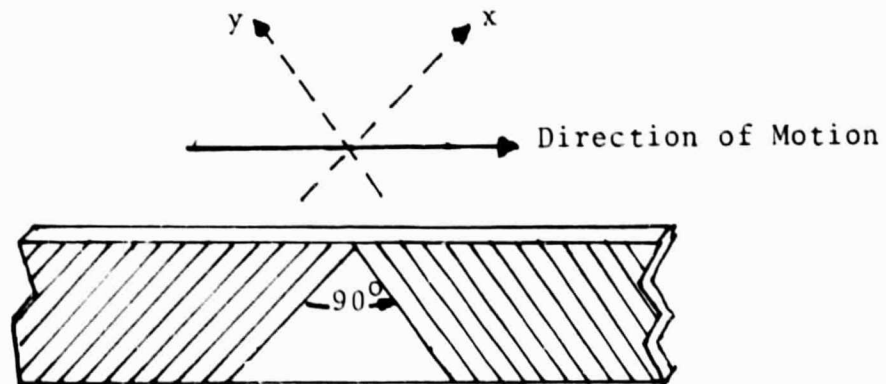


Fig. 4-11 X-Y Measurement

above: crossed grating

below: double-barrel telescope

modulation depth, which is very sensitive to the algorithm, the PSF and the detector configuration. It is safe, however, to bound the line separation between a minimum of one Airy disk diameter and a maximum of about four. The latter number applies to the centroid integrator algorithm. It is arrived at by equating the measurement error contribution due to clipping the tail of the PSF to the error due to background and photon noise.

In the  $f/16$  system, the grating has a maximum of 50 lines/mm. This frequency doubles for an  $f/8$  system (Sec. 6) but still is well within the capabilities of ruling machines and, of course, photolithographic techniques.

#### Detector Configuration

An important item in considering suitable detectors is the spatial resolution or, equivalently, the optimal pixel size. The pixel should be large enough to collect the star photons but as small as possible to reduce the background noise. The minimum number of pixels required to cover the star image is 4, since the image can be centered either on a pixel or on a boundary between pixels. If the detector pixel size is small compared to the Airy diameter, the minimum number of pixels increases to 9: the center pixel and its 8 closest neighbors. Since the limiting noise in many cases is the detector readout noise, it is advantageous to increase the pixel size to about 1.5-2 times the Airy diameter. This assures that at least 90% of the star energy is collected by four detector pixels, regardless of the star location on the detector array. The effect of background noise can be minimized by matching the pixel size to the grating line spacing. For example, if the line spacing is one Airy diameter, it is best to make the pixel size exactly 2 Airy diameters. The average background flux on the pixel remains constant as the grating moves.

What effect does this rather coarse detector resolution have on the ability to resolve and identify each star in the FOV? - Assuming  $10^3$  stars, an Airy diameter of 0.28 arcsec, and a 10' FOV diameter, the area covered by the stars is only about  $2 \times 10^{-4}$  of the detector area. The average separation between stars is about 140 Airy diameters. The probability for stars to be separated only by a few pixels is very small indeed!

The baseline configuration splits the field into quadrants. Assume a pixel size of 0.55 arcsec (2 Airy diameters); then each detector requires about 540x540 elements. Detectors of this size are well within current CCD technology. Assuming a low-noise device with 1 MHz readout rate the serial frame rate is 3.4 Hz. It is possible, however, to considerably exceed this rate by reading out selected lines only, or by designing the device with parallel video output.

Current CCD technology can be exemplified by the image sensor developed for the NASA Solar Optical Telescope (SOT) program, in a joint effort by JPL and Texas Instruments. This device, which will be used on the Lockheed Coordinated Filtergraph Spectrograph experiment, has 1024x1024 elements, 1 MHz readout rate, 20 noise electrons per pixel, and a dynamic range of  $10^5$ . The dark current is 0.3 electrons/sec at 200°K.

An alternative detector, which allows random access to blocks of pixels is the Charge Integrated Device (CID). This detector can achieve higher frame rates due to its random access capability. Developed by General Electric, it approaches a quantum efficiency of 50% at 0.5  $\mu$ m and so far is available in sizes of up to 388x488 pixels. A device with 512x512 pixels, hardened for space applications, is under development.



### Effects of Detector Non-Uniformities

The requirement of simultaneous position measurement of a large number of stars mandates detection at an image plane, since only there can the stars be resolved and identified. The detector signal as described by equations (4-18) and (4-19) is a function of the product of the irradiance distribution  $E(x,y,t)$  and a generalized aperture function  $a(x,y)$  which includes the relay optics, PSF, as well as spatial variations in the detector responsivity. The latter is a serious potential error source, since the candidate detectors (PMT or solid state devices) will exhibit large spatial and temporal variations in response relative to the intended accuracy of the instrument.

This problem can be eliminated if detection can be performed in the pupil plane rather than in an image plane. In this case, the product  $E(x,y,t)a(x,y)$  is converted into a convolution  $E*a$  and the spatial variations in the detector responsivity do not introduce a measurement error. Unfortunately, the stars are not resolved in a pupil plane, and it is required therefore to devise a way by which resolution is preserved and, at the same time, an effect approximating pupil plane detection is created. Essentially, it is required to "scramble" the star light after it passes through the grating, in such a way that the image of the grating will appear diffuse in the detector plane. There are several methods of achieving this effect, and all incur a penalty of increasing the effective detection area and admitting more background light. The most obvious solution is to design the relay lens such that it does not resolve the grating. This is guaranteed if the apodized stop matches exactly the relayed pupil size. In this case the F No. of the relay optics is given by

$$F_r = -mF_p \quad (4-42)$$

where  $F_r$  and  $F_p$  are the focal ratios of the relay optics and the

primary mirror, respectively, and  $m$  is the magnification of the relay optics. It is easy to see that the lens cannot resolve the grating lines, if the lines are spaced by one Airy diameter. The resolution of the lens is  $2.44 \lambda F_r$ , or, equivalently,  $m(2.44 \lambda F_p)$ , with the obvious result that as long as the numerical apertures are matched the relay lens cannot do better than the primary mirror resolution. There is, therefore, a fundamental difference between a detector which is in proximity to the grating, and a detector which is in proximity of a relayed image of the grating. In the first case, as the grating moves across the detector, different parts of the detector sense the transmitted light. In the latter case, since the grating is unresolved, the light transmitted by the grating is spread over the detector. Since the grating diffracts light it is advantageous to use relay optics with a numerical aperture larger than that of the primary mirror, so that several diffraction orders can be collected. There is a trade-off then between the grating spacing and the relay lens resolution: the effects of detector non-uniformity are less important as the grating line spacing increases.

Additional blurring can be obtained by defocussing the relay lens slightly. Since the stars are separated on the average by many Airy diameters, identifying and resolving them is not a problem. Defocussing is more effective as the numerical aperture of the relay lens increases since the depth of focus decreases.

To conclude, detector non-uniformities are not detrimental to the measurement accuracy, and the penalty paid by admitting more background light onto the detector is not severe since for most stars the limiting noise is photon noise, not background (cf. Fig. 2-7).

### Cooling

The focal plane should be cooled if non-intensified CCD detectors are used. It is also desirable to maintain the grating at a low temperature to minimize the coefficient of thermal expansion of the fused silica substrate. The optimal temperature is below 200K and is well within the capacity of passive cooling systems. For example, the Infrared Handbook presents data on large area passive coolers, including a system which maintained 100 K with a cold patch area of 12 ft<sup>2</sup>, a net cooling capacity of 1 w, with a radiator diameter of 46 in.

### Data Handling Requirements

It is expected that the astrometric telescope will have a certain degree of on-board processing and autonomy of house keeping functions. The exact level of partition between on-board functions and ground-controlled functions is difficult to define at this stage of the concept. It is easier to assess the load of data processing.

The maximum frame rate of the detectors can be estimated from a consideration of photon noise: 1/100 s of integration time yields about 30 photons from a 15-magnitude star and a 100-Hz frame rate, almost independent of the algorithm used, is a safe upper bound. We assume on-board discrimination of the pixels which contain useful information, which is a relatively simple function to perform. With 4 pixels per star and 10<sup>3</sup> stars, the useful information comes at a maximum rate of 4x10<sup>5</sup> words per second.

As a comparison, consider the UARS observatory which is specified with a maximum of 512 k bps data transfer rate through TDRSS or GSTDN. It appears that the astrometric satellite requirements can be met with on-board-processing to compress the data. A lower bound on the data rate can be estimated by assuming a 1-Hz frame rate, centroid calculations by on-board computer, and a star population

of 100 stars, which results in a data rate of only 400 words/sec.

The preferred approach to signal processing is a Programmable Pipeline Processor (PPP), which is an extremely efficient architecture for serial processing of algorithms that do not require any parametric update, or require updates at a low rate. Such architecture can perform the centroid algorithms at rates of the order of several Mbps, which is well within our requirements. A rather small computer is then required to handle house-keeping functions and update the algorithm parameters.

#### 4.8 Discussion of Measurement Error Sources

The photon-noise limited measurement error is given by

$$\sigma = \frac{\lambda}{2D} \text{SNR}^{-1} \quad (4-43)$$

where the signal-to-noise ratio is

$$\text{SNR} = \frac{D}{2} (\pi \eta N t)^{1/2}$$

D is the mirror diameter,  $\eta$  the total optical efficiency, N the photon rate (photons/m<sup>2</sup>.s) and t the integration time. The practical limit on accuracy is set by a multitude of other error sources. We distinguish between systematic and random errors. The systematic errors can be attenuated by calibration procedures, while the random errors can be attenuated by data averaging and increased observation time. It is impossible to derive accurate performance values without a system model and modeling the noise processes. Within the scope of this study we addressed several obvious error sources and tried to assess their impact using some simplified assumptions, as discussed in the following sections.

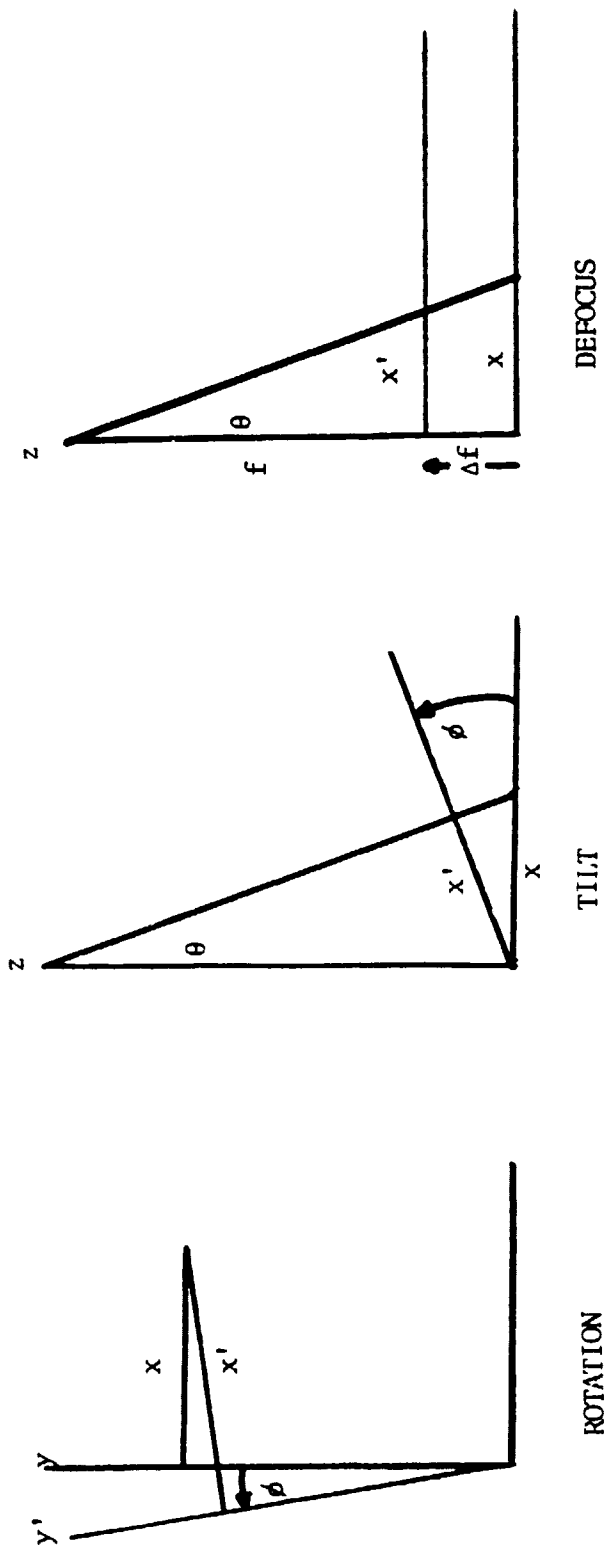


Fig. 4-12 Grating Misalignment

#### 4.8.1 Grating Misalignment

Grating misalignment is a potential source of systematic errors. These can be classified into errors which are linear with respect to the star position in the FOV, and non-linear errors. The linear errors result in a scale change or in a shift of the origin. These errors are taken out by means of an affine transformation. The non-linear errors require higher-order modeling. Since the instrument measures a large number of stars simultaneously, a higher order model is possible in principle, but it is limited by the SNR of the instrument.

##### In-plane Motion

Suppose after measuring the x-coordinate of a star, the ruling is turned by  $90^\circ + \phi$ , where  $\phi$  is the error in question. (The z-axis is the optical axis). The measured angle y-coordinate of the star is  $y'$  while the actual one is  $y$ . The difference is

$$\begin{aligned}\Delta y &= y' - y = y \cos \phi - x \sin \phi - y \\ &\approx -y \phi^2/2 - x \phi \\ &\approx -x \phi\end{aligned}\tag{4-45}$$

since  $\phi$  is presumably a small angle. For two stars, 1 and 2, the relative y-coordinate error is

$$\Delta y_1 - \Delta y_2 = (x_2 - x_1) \phi\tag{4-46}$$

Let  $x_2 - x_1 = 5$  arcmin (a typical star separation in a  $10 \times 10$  arcmin FOV). Then the error is  $10^{-6}$  arcsec if

$$\begin{aligned}\phi &= 10^{-6} \text{ arcsec} / 5 \text{ arcmin} \\ &= 0.6 \times 10^{-3} \text{ arcsec}\end{aligned}\tag{4-47}$$

Rotation of a 10 cm long ruling by this angle corresponds to a motion of the tip (of the ruling) of about  $16 \text{ \AA}$  only! - Note that the error is linear with field angle.

##### Tilt

Suppose the ruling is tilted by a small angle  $\phi$  as shown in Fig. 4-12. A star at the field angle  $\theta$  will have an image at  $x'$  instead of  $x$ . Now

$$v \ x = L \tan \theta \quad (4-48)$$

$$\frac{x'}{\sin \theta} = \frac{L}{\sin (\pi/2+\phi-\theta)} \quad (4-49)$$

which gives

$$\Delta x = x' - x \quad (4-50)$$

$$\begin{aligned} &= L \left[ \frac{1}{\cos \theta} - \frac{1}{\cos (\theta-\phi)} \right] \\ &\approx \theta^2 \phi \cdot L \end{aligned}$$

The error in the measured field position is  $\Delta x/L$ , which is quadratic in field angle  $\theta$  and thus not a scale factor. For  $\theta=5$  arcmin,  $\Delta x/L=5 \times 10^{-12}$  rad ( $=10^{-6}$  arcsec), we have  $\phi=2 \times 10^{-6}$  rad = 0.5 arcsec, the allowable tilt.

#### Defocus

If the primary mirror-grating distance changes by the amount  $\Delta f$  as shown in Fig. 4-12, then a star with field angle  $\theta$  will have an image centered at  $x'$  instead of  $x$ . The measured position is then in error by the amount

$$\Delta \theta = \theta \frac{\Delta f}{f} \quad (4-51)$$

This error is linear with field angle and thus a scale change which can be taken out in data processing. A second order effect will be the aberration balance. However, ray traces executed for even 250  $\mu$ m defocus showed no detectable non-linearity. Focus can be controlled by thermal control of the truss and active alignment to  $\mu$ m accuracy.

#### 4.8.2 Grating Line Errors

The grating lines are the scale by which the star positions are determined, and irregularities in the lines result in a measurement error.

The grating can vary in line center and line width. The line center can be defined as the average over the FOV. The width varies along the line and can be characterized in terms of average and rms variation. The statistics can be taken over the full line length or over an Airy diameter only. The errors can be further divided into calibrated and uncalibrated errors. The measurement accuracy (whether with optical microscope or SEM) is better than the manufacturing accuracy, and direct calibration of the grating geometry should improve performance. The production accuracy depends, naturally, on the technology. Lithographic methods can probably hold dimensional stability of  $0.1 \mu\text{m}$  or better. Ruling machines can do better. The diamond turning machine developed at Lawrence Livermore Laboratory is designed to achieve a displacement stability of better than  $2.5 \text{ \AA}$ . The design specifications for material removal (surface accuracy) are  $0.027 \mu\text{m}$  rms over 64" travel of the diamond tool, and  $0.01 \mu\text{m}$  peak-to-valley accuracy in the azimuthal direction, obtained by turning the work piece while the diamond tool is stationary. The rms surface finish is better than  $0.004 \mu\text{m}$  rms. This machine is controlled by laser interferometers and achieves local temperature stability of  $0.001^\circ\text{F}$ .

In the light of the above, it is reasonable to assume that, given the resources, the grating lines can be produced and calibrated to an accuracy of better than  $0.01 \mu\text{m}$  rms, both in line center and line width. Assuming that the errors in line center are not correlated, about  $2 \times 10^4$  line crossings will be required to reduce the error to  $10^{-6}$  arcsec (rms) with a 16 m telescope, and  $8 \times 10^4$  crossings with a 8 m telescope. These numbers put



a lower limit on the measurement bandwidth. For example, if the integration time is 10 hours, the minimum frame rate is about 0.5 Hz for the 16 m telescope, and 2 Hz for the 8 m telescope. These rates are compatible with the proposed detectors.

#### 4.8.3 Effect of Aberrations

Aberrations in the optical system have two major effects: 1. They move the image position, and 2. they enlarge the PSF.

The image motion due to aberrations is not as severe a problem as one might suspect: The centroid of the PSF is proportional to the average gradient of the wavefront. As long as the mirror is uniformly illuminated, the average gradient depends only on the value of the wavefront at the boundaries. This means that "bumps" on the mirror will not shift the centroid! (This is another advantage of using the centroid as image position parameter).

The spot enlargement directly impacts the SNR. While the exact nature of the effect depends on the algorithm, to first order the theoretical limit on accuracy is inversely proportional to the rms spot size. This puts a limit on the F/number of the telescope for a given desired performance. The angular spot size grows rapidly off-axis as the focal length is reduced to below F/8 (cf. Table 4-4). This is why an F/8 system (or slightly slower) is proposed and evaluated as baseline for a scaled-down astrometric telescope (scaled down to save cost with minimum loss of performance) in Sec. 6.

#### 4.8.4 Photon-Noise-Limited Integration Time

For the imaging telescope, the centroiding accuracy is

$$\sigma = \frac{\lambda}{2D} \frac{1}{\text{SNR}} \quad (4-43)$$

where

$$(\text{SNR})^2 = (\pi D^2/4) \eta N t \quad (4-44)$$

D the aperture diameter, SNR the (photon-noise-limited) signal-to-noise ratio,  $\eta$  the photon efficiency, N the number of photons per unit area of the aperture, t the integration time.

Suppose a reference frame accuracy of  $\sigma$  is to be obtained using all stars in the FOV with magnitude between m and M, and suppose  $n_i$  is the number of stars (in the FOV) with magnitude between i and (i+di). Then

$$N = 3.1 \times 10^{10} \sum_{i=m}^M n_i 10^{-0.4i} \quad [\text{photons.m}^{-2}\text{s}^{-1}] \quad (4-52)$$

Inserting N into Equ.(4-44), we have for the integration time

$$t = \left[ \frac{\lambda}{2D} \right]^2 \sigma^{-2} \left[ \frac{\pi D^2}{4} \eta 3.1 \times 10^{10} \sum_m^M n_i 10^{-0.4i} \right]^{-1} \quad (4-52)$$

If D is in meters,  $\sigma$  in  $10^{-6}$  arcsec, then

$$t = 0.13 D^{-4} \eta^{-1} \sigma^{-2} \left[ \sum_m^M n_i 10^{-0.4i} \right]^{-1} \quad [\text{s}] \quad (4-53)$$

For the baseline telescope, D=1. If we assume a total photon efficiency of 0.1 (factor 0.5 loss of photons by the Ronchi ruling, plus 20% photon and optical train efficiency),  $\sigma=1$ ,  $m=M=15$ , then  $n_{15}=24$ , and  $t=15$  hours. If stars between 15 and 21 magnitude are used as references,  $m=15$ ,  $M=21$ , and  $\sum n_i 10^{-0.4i}=10^{-4}$ ,

which gives  $t \approx 4$  hours. The total photon efficiency of the astronomic telescope may be as high as 20%, in which case  $t \approx 2$  hours. We conclude that the integration time to establish a stellar reference frame to 1 micro-arcsec accuracy requires between 1 and 10 hours integration time, depending on the choice of reference stars and the system efficiency.

The image centroiding accuracy in a single frame is also limited by the grating line accuracy.  $N$  grating crossings will (at least in theory, providing other systematic and random errors are negligible) reduce the error by  $N^{-1/2}$ . If the grating lines are measurable to  $0.01 \mu\text{m}$  (cf. Sec. 4.6.2), the integration time for  $10^{-6}$  arcsec accuracy is

$$t = \left( \frac{10^{-8}}{5 \times 10^{-12} \times 16} \right)^2 \frac{1}{\nu} \quad (4-54)$$

where  $\nu$  the frame rate. For a frame rate of 10 Hz, the time is about 0.4 hours. This is about 40% above the value for an  $m=7.3$  (total efficiency of 0.1 assumed). Thus accuracy is limited by line inaccuracy in this case. By contrast, for much fainter stars, say  $m=15$ , the reverse is true. For the F/8 telescope, The integration time limited by line accuracy, for the same conditions, is a factor 8 higher than the photon-noise limited time (increase in spot size due to increased coma taken into account) for the  $m=7.3$  star. Still, for the much fainter stars, the photon-noise limit dominates.

#### 4.9 Telescope Baseline System

Fig. 4-13 shows the overall design of the astrometric telescope in the deployed configuration as well as stored in the Shuttle payload bay. The overall length is 23.6 m and it includes an extended front baffle (sun shade). Actual length of the sunshade is TBD from detailed straylight analysis. The main structure is a graphite-epoxy monocoque shell in two sections. In the stored configuration the sunshade is slid over the forward section of the telescope barrel which in turn is slid over the rear section. As stored, the total length of the system is about 11 m - significantly less than the Shuttle payload bay length (18 m). This deployed telescope design is therefore volume efficient.

The forward section of the telescope barrel contains the focal plane, and the rear section the 1 m diameter, solid ULE primary mirror (f/16) and its support. There is no secondary mirror.

The spacecraft components are supported in a Gr/e structure to which the telescope barrel is attached as shown in Fig. 4-13. The figure also shows how the system is attached to and supported in the Shuttle payload bay. The 500 ft<sup>2</sup> (3.0 kW power) solar arrays are hinged from the spacecraft and have two degrees of freedom for sun-tracking. In stored configuration they fold underneath the spacecraft structure as shown in Fig. 4-13.

The resonant frequency of the telescope barrel is about 14 Hz; the frequency can be increased by increasing the wall thickness of the barrel (i.e. at a weight penalty which increases rapidly with increasing frequency, as Fig. 4-14 shows).

The spacecraft is a new design and has the subsystems: Attitude Control and Guidance (includes thrusters, torquers, attitude sensors, inertial reference units); Electrical power (solar arrays, batteries and power conditioners); Propulsion (tankage, engines & mounts, propellant); Command Control and Communication (CD&H) (computers, recorders, receivers, transmitters, antennas and multiplexers); and Thermal control (insulation MLI blankets,

ORIGINAL PAGE IS  
OF POOR QUALITY

LMSC-D870885

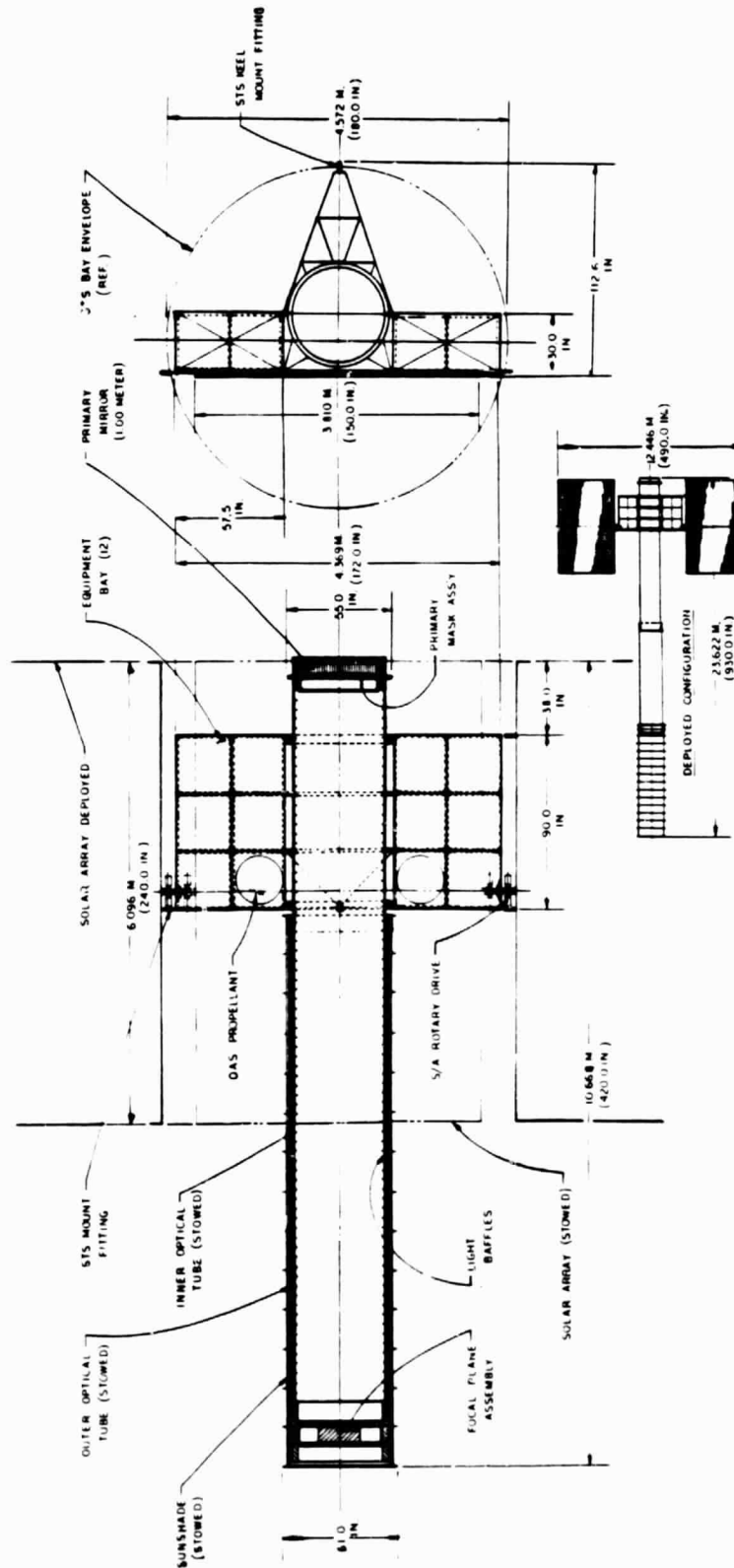


Fig. 4-13 F/16.5 Imaging Telescope System

4-57/58

ORIGINAL PAGE IS  
OF POOR QUALITY

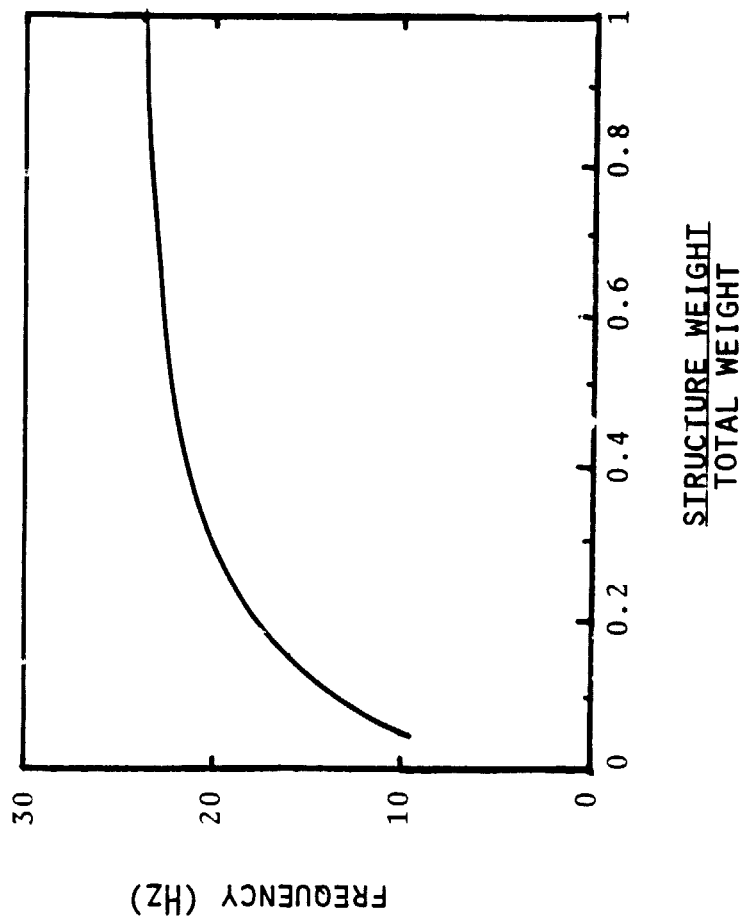


Fig. 4-14 Structure Resonance Frequency

heaters, sensors and electronics; thermal door, pre-launch air-conditioning).

#### 4.10 Weight

A weight breakdown of the system was made, based on direct calculations, estimates, and comparison with comparable systems or subsystems. The results are given in Table 4-5. The total dry weight is 3829 kg and includes a contingency of 10%.

#### 4.11 Cost

Cost estimates were generated parametrically, with judgments made for exotic components. The development cost includes brassboards for components and a prototype flight unit. No facilities requirements were identified and no GFE. The cost summary for the Mission Equipment (telescope) is given in Table 4-6. The total cost is about \$130M in constant 1982 dollars. The structure represents the major cost item because of size, deployment and use of exotic materials (Gr/Ep).

A cost estimate was also generated for a suitable spacecraft, for which, because of the size of the instrument, a new design was assumed. The RCM cost is about \$350M (compare: ST spacecraft, the SSM, cost is \$336M). Thus a total system cost (not including launch and operations) would be about \$480M. To reduce the total cost, therefore, a scaled-down imaging telescope was considered which uses an existing low-cost spacecraft. This is discussed in Ch. 6 of this report.

ORIGINAL PAGE IS  
OF POOR QUALITY

TABLE 4-5  
ASTROMETRIC TELESCOPE WEIGHT ESTIMATE  
(kg)

STRUCTURAL SUBSYSTEM	1321	PROPULSION	261
Optical barrels	496	Tanks	158
Sunshade	209	Motor and mount	36
Equipment rack	291	Control electronics	14
Deployment mechanisms	102	Plumbing, valves, brackets	53
Fittings, fastenings	223		
		CD&H	276
PAYLOAD	698	Computer, processors	68
Mirror and support	355	Data recorders	109
Baffle assembly	61	Receivers, transmitters	24
Focal plane & support	264	Multiplexers, antennas	43
Alignment system	18	Telemetry sensors	9
		Brackets, fastenings	18
		Signal conditioners	5
ATTITUDE CONTROL & GUIDANCE	472		
Thrusters	18	THERMAL CONTROL	198
Torquers & electronics	339	Insulation blankets	64
Inertial reference frame	38	Heaters, sensors, electronics	27
Attitude sensors, electronics	39	Thermal door, drive	80
Plumbing, valves, brackets	38	Pre-launch airconditioning	18
		Brackets, etc.	9
ELECTRICAL POWER	603		
Solar arrays	263		
Batteries	164		
Conditioners, controllers	49		
Power-Junction box	18		
Cables, connectors	109		
		Total weight (dry): 3829 kg	
		=====	



TABLE 4-6

## ASTROMETRIC TELESCOPE COST ESTIMATES (\$M)\*

	DEVEL. & BB	PROTOFLT.	TOTAL
1 m dia. primary, ULE, & support	2.4	2.0	4.4
FPA, Support and electronics	7.5	4.2	11.7
Motorized grating, electronics, software	9.0	5.5	14.5
Optics alignment, control and S/W	7.9	4.8	12.7
Telescope structure	28.2	8.6	36.8
Telescope thermal	2.8	0.7	3.5
Design, development, hdw. subtotal	57.8	25.8	83.6
GSE, GHE & STE	5.6	1.7	7.3
Integration & Test	8.3	4.2	12.5
Systems Engineering, Q.A., Reliability	11.9	5.1	17.0
Program Manag.t & Data	6.6	2.9	9.5
TOTAL	90.2	39.7	<u>129.9</u>

\* Mission Equipment only

## 5. INTERFEROMETER-TELESCOPE COMPARISON

### 5.1 Summary

Principal characteristics of the two systems are listed in Table 6-1 which highlights the main differences as well as similarities.

Overall size and weights are similar, the interferometer being somewhat heavier due to the more complex optical system. The instrument costs are, by contrast, quite different, the interferometer being more than twice as expensive.

The measurement techniques are of course quite different which is reflected in the substantially different optical design, the interferometer being more complex than the imaging telescope. The interferometer relies on precision measurements of a few stars (four are assumed in our baseline concept design), whose sufficiency needs yet to be established. The telescope averages low accuracy measurements of many stars, in order to obtain the same stellar reference frame accuracy as the interferometer.

While the interferometer is more sensitive than the imaging telescope, as reflected in the lower photon-noise limited integration time<sup>\*</sup>, the interferometer faces two difficulties in obtaining sufficient accuracy: one lies with the instrumental errors, the other with the fact that only a few stars can be observed simultaneously. Due to the instrumental errors, the feasibility of the interferometer is questionable and a conceptual breakthrough seems required. By contrast, the imaging telescope is within the state-of-the art, although an optimal design requires study and would benefit from further advances in solid state detectors.

<sup>\*</sup>for some scenarios

TABLE 5-1  
INTERFEROMETER - TELESCOPE COMPARISON

ISSUE	INTERFEROMETER	TELESCOPE
Overall length	16.5 m	18 m + sunshade
Weight (all-up), dry, kg	4500	3800 kg
System structure	folding Gr/Ep truss	telescoping Gr/Ep barrel
Spacecraft	new	
Orbit	circular 325-350 n.mi., 28.5° incl	
Delivery to orbit	Shuttle plus transfer by system engine	
ROM instrument cost, \$M	296	130
Central wavelength, Å	5500	
Passband, Å ( $\Delta\lambda$ )	3000	only detector limited
Primary Optics	2, 0.9 m circular flats (ULE)	1 m diam. parabola (ULE)
Secondary optics	folding and turning flats	no secondary
	focussing optics	focussing optics
Detectors	image dissecting tube	CCDs or CIDs
Measurement technique	OPD between stars	centroid images
Accuracy achieved	precision measurement of a few stars	averaging of many stars low accuracy each
Number of stars observed	4	$>10^3$ , detector limited
Nominal integration time (baseline task)	~10 min (15th mag ref. stars) ~1 hr (all FOV ref. stars)	~8 hrs. (15th mag. ref. stars) ~1 hr. (all FOV ref. stars)
Dependence on mirror diameter D length (L or f)	D <sup>-2</sup> L <sup>-2</sup>	D <sup>-4</sup> for F>8 F <sup>-4</sup> for F≤8 (coma limited)

LMSC-D870885

TABLE 5-1 ctd

ISSUE	INTERFEROMETER	TELESCOPE
Concept Feasibility/risk Performance sensitive parameters	uncertain/high optical tolerances star switching frequency photon efficiency	established/low grating stability x-y measurement coupling high order aberrations photon efficiency
Technology challenges	alignment system beam-splitter grating beam sampler control system architecture	large area parallel access CID
Further study items	sufficiency of a few stars alignment & control system scaling (cost, performance, feasibility)	optimal measurement algorithm' modeling of errors optimal f No. simultaneous x-y measurement

LMSC-D870885

## 5.2 Comparison of Speed

The centroiding accuracy of the astrometric telescope is

$$\sigma_T = \frac{\lambda}{2D_T} \frac{1}{\text{SNR}_T} \quad (5-1)$$

and of the interferometer

$$\sigma_I = \frac{\lambda}{2\pi L} \frac{1}{\text{SNR}_I} \quad (5-2)$$

(the subscripts  $T$  and  $I$  refer to Telescope and Interferometer, respectively in all that follows).  $D_T$  is the mirror diameter of the telescope,  $L$  the baseline separation of the interferometer end mirrors (diameter  $D_I$ ), SNR is the signal-to-noise ratio, which in the photon-noise limit is

$$\text{SNR} = \sqrt{A\eta Nt} \quad (5-3)$$

where  $A$  the collecting area,  $\eta$  the total photon efficiency,  $N$  the rate of photons to the aperture ( $\text{photons} \cdot \text{m}^{-2} \cdot \text{s}^{-1}$ ), and  $t$  the integration time.

The speed of the instrument will be compared in terms of the time required to establish a reference frame of  $n$  stars to the accuracy  $\sigma = 10^{-6}$  arcsec. The comparison can be made in several ways. As shown in Appendix B,  $N$  is the photon rate from all  $n$  stars. Thus

$$N = \sum_{k=1}^n N_k \quad (5-4)$$

where  $N_k$  is the rate from the  $k$ -th star. A fundamental difference between the telescope and the interferometer is that the  $n$  stars are observed simultaneously by the telescope, each using the full aperture, whereas in the interferometer they share the aperture

spatially or temporally. Consider two cases: (I) The stars are all of magnitude  $m$ ; and (II) the stars range from magnitude  $m$  to  $M$ .

(I) All stars of magnitude  $m$  in FOV

In this case

$$N_T = 3.1 \times 10^{10-0.4m} n_m \quad [\text{photons} \cdot \text{m}^{-2} \cdot \text{s}^{-1}] \quad (5-5)$$

where  $n_m$  is the number of stars with magnitude between  $m$  and  $(m+dm)$  in the FOV (cf. Fig.1-1). For the interferometer, if we assume that the stars share the full aperture equally

$$N_I = 3.1 \times 10^{10-0.4m} \quad (5-6)$$

Thus

$$\frac{t_T}{t_I} = \left( \frac{\pi L}{D_T} \right)^2 \frac{\eta_I}{\eta_T} \frac{A_I}{A_T} \frac{1}{n_m} \quad (5-7)$$

For the two baseline systems, the first factor in (5-7) is about 2200. If we assume the same collecting areas and photon efficiencies for the two instruments (one basis of comparison among several!), then

$$\frac{t_T}{t_I} = 2200/n_m \quad (5-8)$$

Using a  $10 \times 10$  arcmin FOV and 25 15th magnitude reference stars, the interferometer is a factor  $\approx 90$  faster than the telescope. If on the other hand we assume all 21st magnitude stars in the FOV to be reference stars, then the ratio is about 2.

If we assume instead of equal effective areas, equal physical areas of the primary mirrors, then  $A_I/A_T = 2^{-1/2}$  since the interferometer end mirrors are tilted  $45^\circ$  to the line of sight. In that case the ratio of integration times is by the same factor smaller.

An equally valid basis of comparison would be to assume that the two end mirrors of the interferometer are circular flats of the same diameter as the telescope mirror; then  $A_I/A_T=2^{1/2}$ , and the ratio of integration times is greater by the same factor than in (5-8). Other bases of comparison may be assumed.

(II) Reference stars not the same

Suppose that all stars in the FOV with magnitude between  $m$  and  $M$  define the reference frame. Then

$$N_T = 3.1 \times 10^{10} \sum_m^M n_i 10^{-0.4i} \quad (5-9)$$

whereas

$$N_I = 3.1 \times 10^{10} \sum_m^M n_i 10^{-0.4i} / \sum_m^M n_i \quad (5-10)$$

If the collecting area is the same for both sensors, then

$$\frac{t_T}{t_I} = 2200 / \sum_m^M n_i \quad (5-10)$$

If  $m=15$ ,  $M=21$ ,  $\sum n_i = 3100$ . In the "worst" case (equal total physical mirror area of the sensors),  $t_T/t_I = 2200/3100/2^{1/2} = 0.5$ . In conclusion the interferometer is a factor between 1 and 100 faster than the telescope on the basis of photon-noise limit and equal photon efficiencies, and assuming that all stars share the interferometer aperture area equally.

Fig. 5-1 compares the speed of the two instruments on the following basis:

1. The FOV is  $10 \times 10$  arcmin
2. All stars in the FOV with magnitude  $m$  to  $(m+dm)$  are used,  $m \geq 15$  (case I)
3. All stars in the FOV with magnitude greater than 15 are used (case II).

ORIGINAL PAGE IS  
OF POOR QUALITY

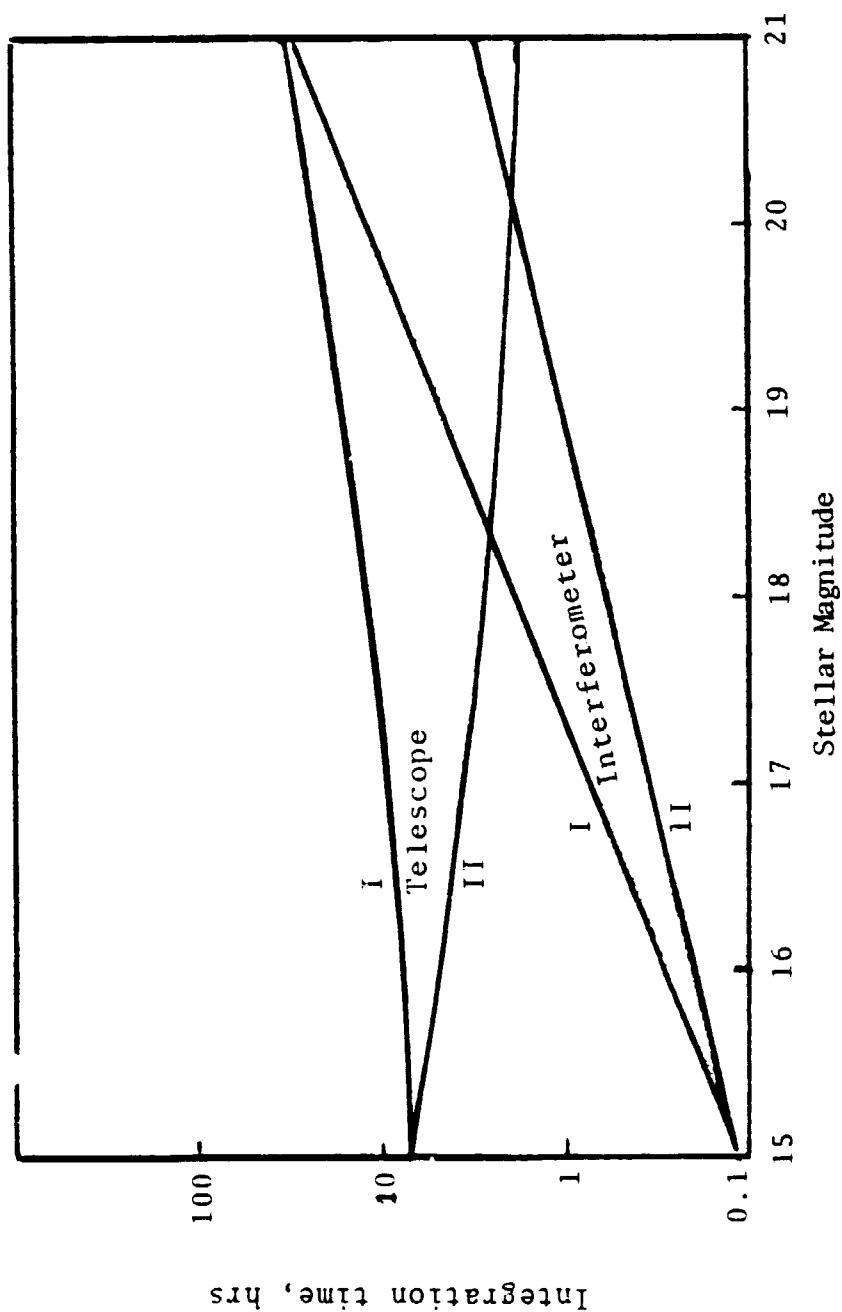


Fig. 5-1 Speed of Instruments



4. The effective areas are in the ratio  $A_I/A_T=2^{-1/2}$
5. The photon efficiencies are the same, 20%.
6. The stars share the interferometer aperture equally.
7. The reference frame accuracy is  $10^{-6}$  arcsec (nominal goal).

We see that the enormous advantage in speed of the interferometer is gradually offset as the number of stars of the reference frame increases and the stars become fainter. Eventually, if all stars in the FOV with magnitude 15 to 21 are used, the speed of the two instruments is comparable. In the case of the interferometer, it is probable that no more than 3-4 stars will be measured simultaneously. A possible aperture geometry is shown in Fig. 3-4. Suppose now that we compare the speed of the instruments on the basis of measuring (centroiding) a faint target star. The star will presumably use one of the larger of the two sets of sub-apertures in Fig. 3-4. If  $D = .9m$ , then we have  $A_T/A_I=3$ , and  $t_T/t_I = 2200/3 = 733$ .

#### Photon Efficiency

The telescope using a transmission grating loses 50% of all incident photons. Further loss by the optics is difficult to estimate at this stage - as it is for the interferometer. For simplicity we might assume the losses to be the same, although there are more reflecting surfaces for the interferometer to be considered. If we assume the interferometer visibility factor to be 0.6, the ratio of the photon efficiencies is  $.5/.6^2=1.4$  in favor of the telescope. Furthermore, means of recovering the other 50% of the telescope photons, at least in principle, e.g. using a corrugated grating or, as suggested in Sec. 4, using a dual-barrel telescope.

Comparison of the instrument performances is likely to be controversial due to the fact that the number and magnitude of required reference stars is in question. It is probably safe to presume that it depends on the observational task and may be less for the interferometer, though how much less is not established. If the interferometer can do with a few (bright) reference stars, say 3-10 as suggested by Shao, then a heavy burden is shifted from measurement accuracy of the system to data processing, analysis and modeling. The question arises how many variables must be modeled, and how successful is this approach compared with relying on the averaging out of the irregular motions of a very large number of stars? Clearly, these issues should be addressed.

### 5.3 Scaling

Because of the lower instrument cost and the feasibility with state-of-the-art technology, the imaging telescope appears to be the preferred concept of an astrometric satellite. To reduce total cost, a scaled down telescope is investigated in Ch. 6, resulting in a 1-m diameter, 8-m focal length system using the Multi-Mission Modular Spacecraft as support system. The scaling of cost and performance of the telescope is relatively straightforward. By contrast, a possible scaling of the interferometer appears more complex.

Many error sources identified for the interferometer can be eliminated by star switching as described in Ch. 3. For planetary detection a sufficiently bright star is always in the FOV to make star switching feasible. In applications, where no such star is available, the method seems uncertain. A larger baseline and larger end mirrors would ease the problem but increase the

difficulties of manufacturing and maintaining the optical tolerances. The reverse would be true by scaling down the baseline and the end mirror size. Performance potential, as given by the photon-noise limited integration time, is very sensitive to scaling (integration time  $\propto L^{-2}D^{-2}$ ). Scaling down the interferometer would therefore have a significant impact on this potential. In summary, the scaling of the interferometer appears to be a more complex issue than for the imaging telescope. With a smaller system an existing small spacecraft (e.g. the MMS) can possibly be used rather than designing a new spacecraft. This issue deserves to be studied further.

## 6. SCALED-DOWN IMAGING TELESCOPE

### 6.1 Summary

In this chapter we present the considerations leading to the concept design of an imaging astrometric telescope of reduced focal length. Since the astrometric telescope with a 1-m mirror diameter and 16.5-m focal length was found feasible with existing technology (cf. Ch. 4) but the total cost, sensor plus spacecraft, excessive, a smaller system capable of utilizing an existing spacecraft design is considered. Sec. 6.2 discusses options of cost reduction, Sec. 6.3 the change in performance of a reduced focal length, and Sec. 6.4 the concept design of a 1-m diameter 8-m focal length system.

The system is illustrated in the frontispiece: The overall length is 13 m, total weight 2900 kg. The main structure is a thermally self-compensating, insulated steel-aluminum truss supporting the telescope tube and the spacecraft. This structure is, in contrast with the full-length baseline 16.5-m focal length system (Sec. 4.7-4-9), non-deployed.

The performance in terms of the baseline task integration time is reduced relative to the  $f/16.5$  system, by a factor 1.4. The total cost of the satellite is, however, significantly reduced: it is \$148M (\$92M for the telescope, \$56M for the MMS plus S/C-P/L integration) compared to \$483M.

### 6.2 Cost Considerations

Total cost can be minimized by reducing the size, avoiding use of exotic materials and high-risk designs, using an "off-the-shelf" spacecraft, and other means.

#### 6.2.1 Reduction of Size

(i) Focal length

Shortening the system has several advantages:

1. Deployment (which we suggested for the full-length baseline, to maximize use of Shuttle payload volume) is a non-deployed structure is simpler and less expensive.

2. The total weight is less, and requirements for propulsion and attitude control capability are reduced.

3. The inertia ellipsoid is more nearly spherical since the largest moment of inertia is reduced; therefore the torques are smaller and the requirements for the ACS are lower.

4. The structural stiffness and thereby the resonance frequency of the truss are increased.

Disadvantages are

1. For the same mirror diameter and FOV the aberrations are greater. However, in this case only the non-linear aberrations are of concern.

2. There may be more straylight in the optical train increasing the requirements for efficient baffling (e.g. longer sunshade).

(ii) Mirror diameter

Reducing the mirror diameter, for example in the same proportion as the focal length (to keep the aberrations constant), has only a small effect on the total system cost but a large effect on performance, since the standard integration time is proportional to  $D^{-4}$ .

### 6.2.2 Material Selection

Basic requirements for the structural material are

- high stiffness
- low weight
- low thermal expansion coefficient
- simple manufacturing techniques
- low cost

Metal matrix composites, now under development for space applications have superior thermal and mechanical properties but are costly in terms of both, raw materials and design/manufacture of structural members. These materials are non-isotropic, and it is not known how their properties change with time in a space environment.

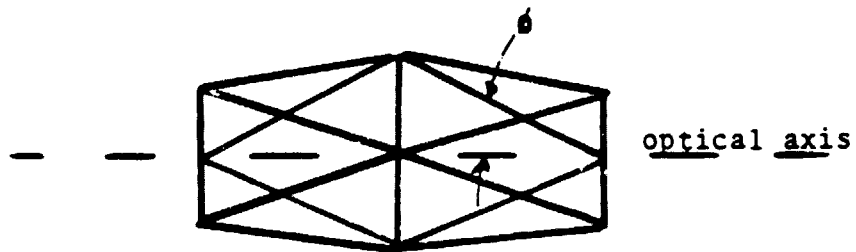
Graphite-epoxy is further developed than metal-matrix and is less expensive but also non-isotropic. Furthermore, the material suffers from moisture absorption and outgassing.

Metals, such as aluminum, steel, invar, titanium, are isotropic materials with no outgassing problems. The manufacturing techniques are well developed and the long-term behavior is known. The bulk material is inexpensive, and stiff and thermally inert structures can be made with them, although the bulk thermal/mechanical properties are poorer than metal-matrixes of Gr/ep.

The concept of a space truss using Al-Steel combination is shown in Fig. 6-1. Truss members for isosceles triangles; the longerons are steel, the cross members aluminum. By properly choosing the angles, a thermally self-compensating structure (no change in length with uniform change in temperature) can be made. Uniform temperature can be achieved with a combination of multilayer insulation and selective heat application.

ORIGINAL PAGE IS  
OF POOR QUALITY

LMSC-D870885



$$\phi = \arcsin \left\{ \sqrt{\frac{a_{\text{longerons}}}{a_{\text{transverse}}}} \right\}$$

Fig. 6-1 Athermal truss concept

### 6.2.3 Other Options

Cost may also be reduced by minimizing

- the degree of autonomy of the system (rely more on ground control). The savings in system design may be outweighed by increased program cost
- the number of degrees of freedom of the solar arrays
- the extent of (autonomous) optical alignment and inertial and thermal control

The actual savings are difficult to assess at this conceptual stage of definition of the instrument and mission objectives.

Concerning a shorter mission life, we considered the alternative of a lower orbit than the minimum required for 5 years:

#### A. Lower orbit

For a lower orbit less orbit transfer propulsion is required i.e. smaller engines, less fuel. A lower orbit also may give more shadow observation time (cf. Fig. 2-3) If operating in the earth's shadow is requirement (not established) the usable orbit time is greater. However, the gain is rather small.

The radiation hazard for electro-optical components is lower in a lower orbit (Fig. 2-4); and finally, retrieval/rescue/reservice cost is lower.

#### B. Same orbit

For the same orbit altitude, a shorter mission duration implies less

- propulsion for orbit maintenance
- solar array degradation (i.e. less requirement for oversizing)
- less radiation exposure (lowered requirement for radiation hardening)



The possible small cost advantages associated with a shorter mission life seem to be outweighed by the loss in science utility: Reducing for example, the lifetime from 5 to 2 years means loss of 3/5 of the programs. In addition, some programs, particularly extrasolar planet detection, may be entirely unfeasible with a mission life much shorter than 5 years.

#### 6.2.4 Spacecraft

The choice of a suitable spacecraft is driven by cost and performance requirements. The latter are outlined in Table 6-1. A possible choice exists between the Multimission Modular Spacecraft (MMS) and the System Support Module (SSM) of the Space Telescope. The SSM has a greater payload capacity but lacks a propulsion system for orbit transfer - which the MMS has. The SSM would also be more expensive than the MMS, thus the MMS was chosen as spacecraft for a reduced telescope system.

##### MMS Spacecraft - General Description

The baseline MMS is described by Table 6-2 and Fig. 6-2. The MMS is modular, and the subsystems are: the central support structure and the payload interface ring; the modules for electrical power handling and storage, for attitude control (ACS), communications and data handling (CD&H), and for propulsion. User-supplier mission-peculiar equipment is

- solar arrays
- antennas
- additional batteries & equipment

The MMS has standard interfaces for ground checkout, test procedures, deployment and retrieval, and on-orbit module-interchange.

TABLE 6-1  
SPACECRAFT REQUIREMENTS

Cost	Less than \$75M
Payload capacity	Greater than 4000 lb
Launch vehicle compatibility	Shuttle, others desirable
Design life	5 years
Attitude control	Drift less than 1 arcsec/min
Electrical Power	1-3 kW; 1 kW average to user
Command and Data Handling	STDN, TDRSS compatible
Orbit transfer	150-350 n.mi.

TABLE 6-2  
MMS BASELINE SPECIFICATIONS

Payload capability	>10,000 lb (Shuttle)
Life	5 years
Launch vehicle compatibility	Shuttle, Delta, Atlas, Titan
Attitude Control	3-axis stabilized, IRU, Star Trackers Pointing accuracy better than $10^{-5}$ deg* Pointing stability better than $10^{-6}$ deg* 20 in.oz. max torque; 15 ft.lb.s momentum storage
Electrical power	3 kW peak, 1.2 kW average, 22-35 V DC (2) 20-Amp.hr, or (3) 50 Amp. hr. batteries
CD&H	STDN-TDRSS compatible; 2 Mbits stored data dump rate $10^8$ or $10^9$ bits tape recorders
Propulsion	Modules PM-1 through PM-VII (cf. Table 6-3)
Weight	2000 lb dry w/o solar arrays, antennas (user-defined)

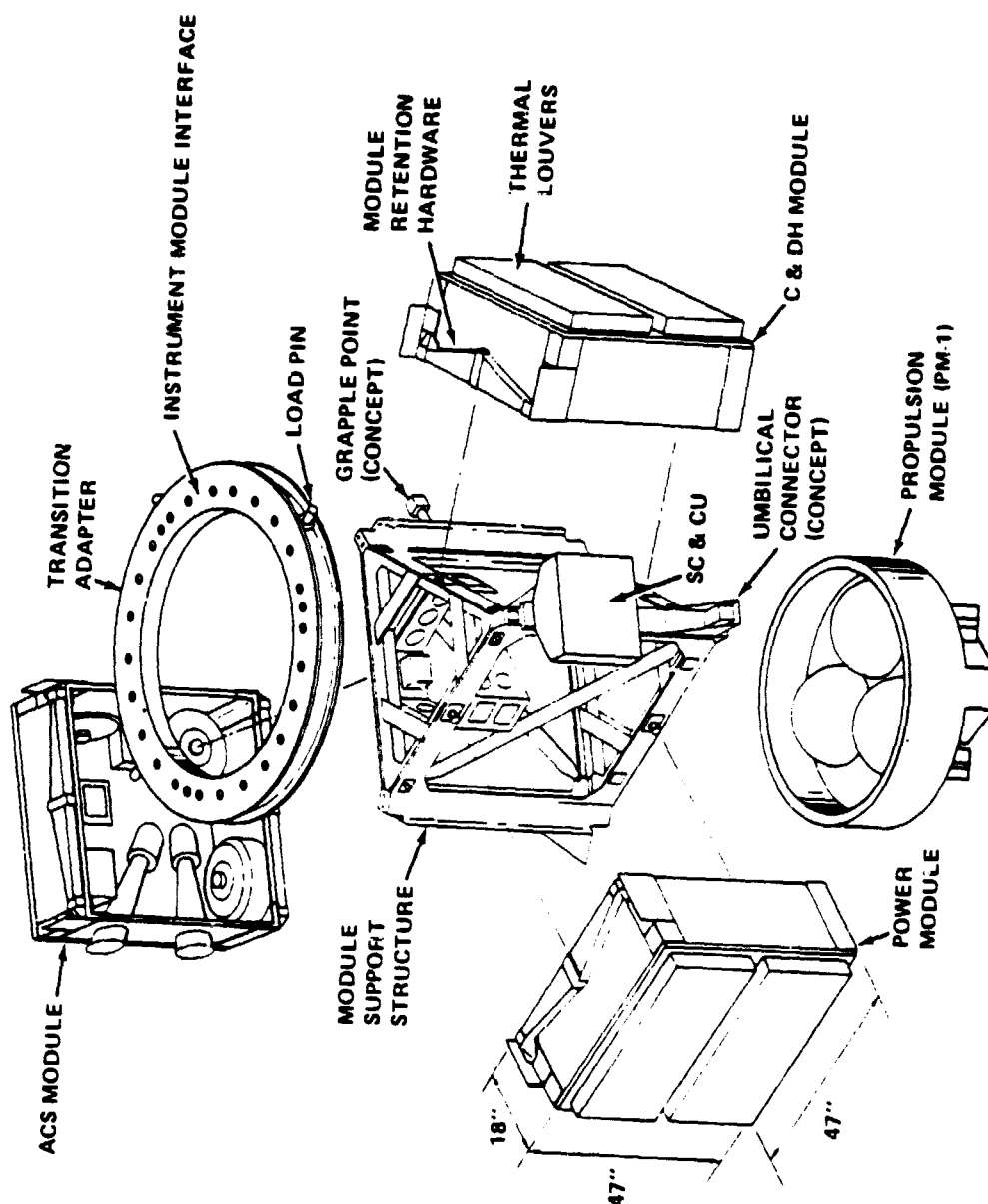


Fig. 6-2 MMS Subsystems

ORIGINAL PAGE IS  
OF POOR QUALITY

LMSG-D870885

### Propulsion

Transfer of the system to the operational orbit (300-350 n.mi.) can be achieved in two ways: By the Shuttle, which would require, as Fig. 6-3 shows, an additional OMS kit. The addition would limit the payload capacity of the Shuttle. (We anticipate that the astronomic telescope will not be the only payload). Alternatively, the system's own propulsion unit could be used.

Transfer from an altitude  $h_1$  to  $h_2$  requires a velocity change of

$$\Delta v = 7.92 \frac{h_2 - h_1}{2R_E} (1 + h_1/R_E)^{-3/2} \text{ [km.s}^{-1}\text{]} \quad (6-1)$$

where  $R_E$  the radius of the earth. The fuel requirement depends on  $\Delta v$ , the payload mass  $m$ , and the fuel efficiency, the specific impulses  $I_{sp}$ :

$$\mu = m \left[ \exp\left(\frac{\Delta v}{I_{sp}g}\right) - 1 \right]^{-1} \quad (6-2)$$

where  $g=9.81 \text{ m/s}^2$ . All except the most powerful propulsion module of the MMS use hydrazine monopropellant for which  $I_{sp} = 230 \text{ s}$ . Since the exponent in (6-2) is small compared with unity, we have approximately

$$\mu/m \approx 0.0005 h_2 - 0.075 \quad (6-3)$$

where  $h_2$  is in n.mi. Table 6-4 shows the fuel requirements as a function of payload mass and orbit altitude, for  $h_1=150 \text{ n.mi.}$  (Shuttle handoff). The mass of the 8-m focal length telescope is 5700 lb (dry). For a transfer to 350 n.mi. (probably an upper limit) the required fuel is 570 lb. The module PM-1A is thus sufficient for a one-way transfer.

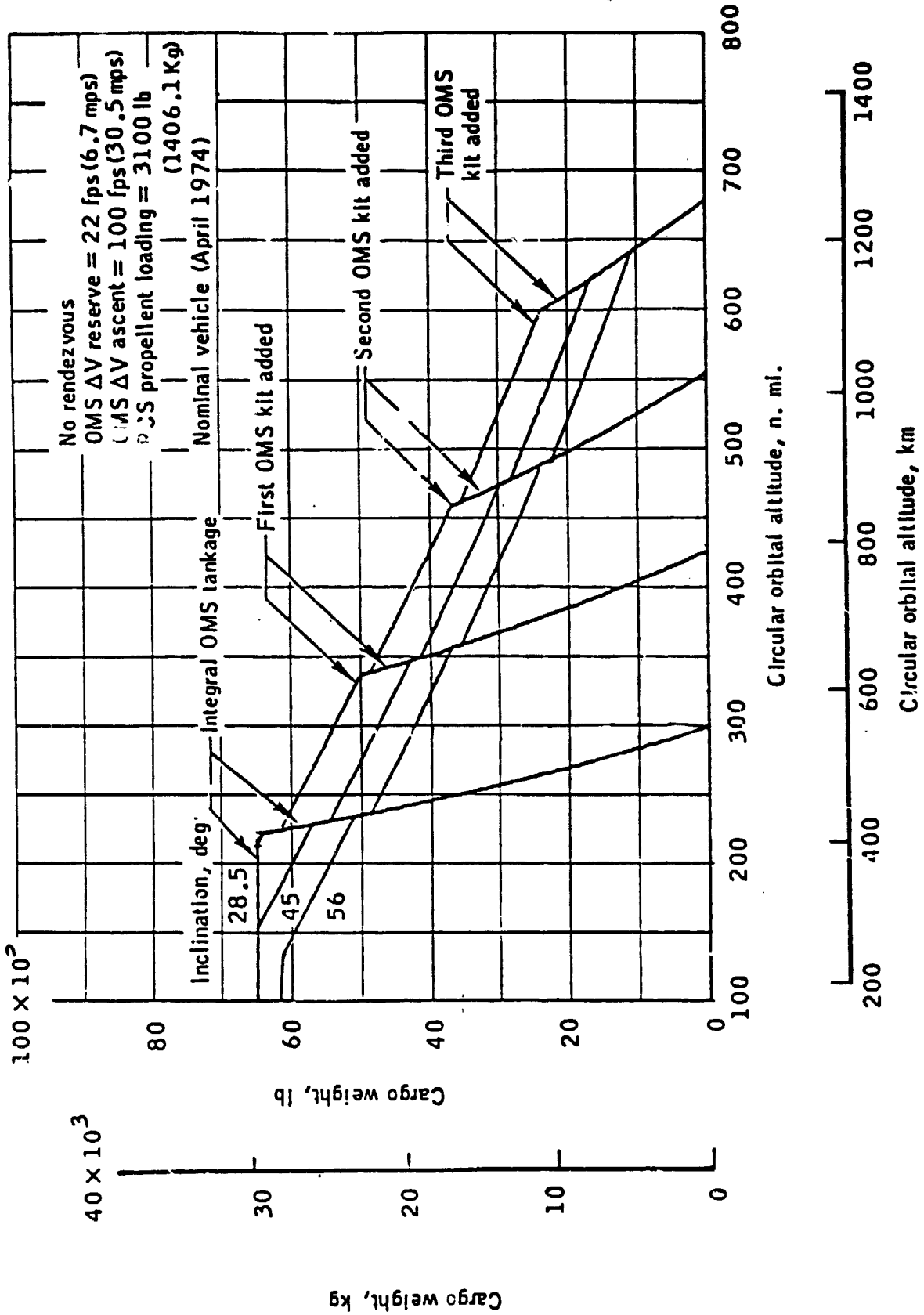


Fig. 6-3 Shuttle Payload Capacity

TABLE 6-3  
FUEL REQUIREMENTS  
(1b hydrazine)

		Orbit Altitude (n.mi.)				
		<u>250</u>	<u>275</u>	<u>300</u>	<u>325</u>	<u>350</u>
Payload mass (lb)	2000	98	123	149	175	201
	4000	196	246	297	349	401
	6000	294	369	446	523	602
	8000	392	493	595	698	803
	10000	490	616	743	873	1003

TABLE 6-4  
MMS PROPULSION SYSTEMS

<u>Module</u>	<u>Propellant</u>	<u>Cost (est)</u>	<u>Comments</u>
PM-I	170 lb hydrazine	-	Insufficient for transfer to 350 n.mi.
PM-IA	588 "	-	Maximum baseline standard
-II	660 "	-	Added tank
-III	974 "	.8-1.5M	Structure mod.s required
-IV	974 "	.55-1.25M	Payload interface mod.s
-V	974 "	1.1-1.9M	
-VI	1130 bi-propellant	1.6-1.9M	



A two-way transfer may be desired, for example for the purpose of refurbishing the telescope after several years. The required fuel is slightly less than twice that for a single transfer. The module PM-V may be adequate for this application. If a greater capacity is desired (two way transfer plus orbit adjust, for example), the PM-VI may be appropriate. The greater  $I_{sp}$  value (300 s) and volume (1130 lb) for that module are equivalent to about 1470 lb hydrazine - more than adequate for a two-way transfer between 150 and 350 n.mi.

#### Attitude Control

Gravity gradient and cross orbit torques are large for elongated structures like the astrometric telescope. The torque is approximately

$$\tau = \frac{3}{2} (I_{11} - I_{33}) \Omega^2 \quad (6-4)$$

where  $I_{11}$  and  $I_{33}$  are the largest and smallest moment of inertia, and  $\Omega$  is the orbital angular velocity ( $10^{-3}$  rad.s $^{-1}$ ). The more nearly spherical the inertia ellipsoid, the smaller the torque. To maintain the system pointed at a star, the ACS must provide sufficient torque to counterbalance the gravity-gradient and cross orbit torque. For the 8-m focal length telescope, we find  $I_{11}=13,000$  kg.m $^2$ ,  $I_{33}=4000$  kg.m $^2$ , and

$$\begin{aligned} \tau &\approx 0.014 \text{ N.m} \\ &\approx 2 \text{ in.oz} \end{aligned} \quad (6-5)$$

The MMS has an adequate torque of 20 in.oz. However, the momentum storage is only 15 lb.ft.s; therefore the torque of 2 in.oz. can be sustained for only 24 minutes. An increase in the momentum storage is thus required. A factor 2-3 increase can be achieved without significant cost differential.

An issue to be further studied is whether guiding with geomagnetic torquers rather than momentum wheels is required. The geomagnetic torquers would introduce no vibration but a spacecraft modification would be required. A simple torquing system is a set of coils wound at  $45^\circ$  to the optical axis of the telescope, on the outside of the vehicle. Three coils are required as a minimum, each arranged  $120^\circ$  from either of the other two. The minimum current each coil must carry is

$$I = \tau / NBA \sin \phi \quad (6-6)$$

where N the number of turns per coil, B the magnetic flux, and A the projected area of the coil perpendicular to the optical axis;  $\phi = 45^\circ$ . For  $N=1000$ ,  $A=2 \text{ m}^2$ ,  $B=10^{-5} \text{ Wb.m}^{-2}$ ,  $\tau=0.01 \text{ N.m}$ , we find  $I=1 \text{ amp}$ . An iron core could be permanently magnetized by an initial current surge, and the large diameter coil could be used as a vernier.

### 6.3 Performance

The reduction of the focal ratio of the telescope increases the rms spot size of the stellar images, as discussed in Sec. 4.6. While the f/16.5 system is diffraction-limited, coma enlarges the spot size by a factor 1.2 at 0.707 of full field for an f/8 telescope. If we assume that the measurement accuracy is proportional to rms spot size, the f/8 system is by a factor 1.2 less accurate than the f/16, and the integration time is correspondingly by a factor  $1.2^2=1.4$  (i.e. 40%) longer. For even shorter focal lengths, the performance degrades rapidly, since spot size is proportional to (f number) $^{-2}$ , for  $f \leq 8$ . Since the system cost, however, does not decrease in the same proportion, there is an optimal f number which may be determined in a detailed systems trade in further studies. We shall assume a baseline system of 8-m focal length.

#### 6.4 8-meter Focal Length Telescope

A conceptual design of a 8-m focal length telescope (1 m mirror diameter) is presented here. As discussed below, the cost of the imaging telescope varies slowly with mirror diameter, and the choice of an f/8 system is not necessarily optimal in terms of performance and cost. It is presented as a baseline primarily because the total cost lies just below a nominal ceiling of \$150M. The concept is shown in Fig. 6-4, and the frontispiece (artist's conception). The primary subsystems of the concept are (i) the structure, (ii) the optics including primary mirror and support, focal plane and support, and baffles; (iii) the MMS spacecraft, with propulsion module PM-1A, and user-defined solar arrays and antennas. The overall length, including sunshade, is about 13 m. The all up weight is 6300 lb which includes 588 lb of propellant for orbit transfer (one way).

##### 6.4.1 Structure

The space truss, which provides structural and thermal stability of the telescope is a self-compensating steel-aluminum concept, consisting of a series of isosceles triangles. The truss weight is 840 lb and the lowest resonance frequency is about 30 Hz, above the anticipated measurement bandwidth of 1-10 Hz. The frequency can be further increased at the expense of increased weight (thicker walls of the truss members), and the weight penalty increases quickly with increasing weight (Fig. 6-5).

The principle of a self-compensating truss - a truss whose overall length (direction of optical axis) does not change with a uniform temperature change, is as follows. Two materials, with different thermal coefficients of expansion,  $\alpha$ , can be structurally combined in such a way that the effective expansion coefficient in one direction is near zero over a wide range of ambient temperatures. Steel and aluminum are commonly selected, aluminum having nearly twice the expansion coefficient than steel. Typically, as in the design, Fig. 6-4, the longitudinal members are steel and the transverse ones aluminum, which form the compensating structure. The steel joints are welded whereas the aluminum

ORIGINAL PAGE IS  
OF POOR QUALITY

LMSC-D870885

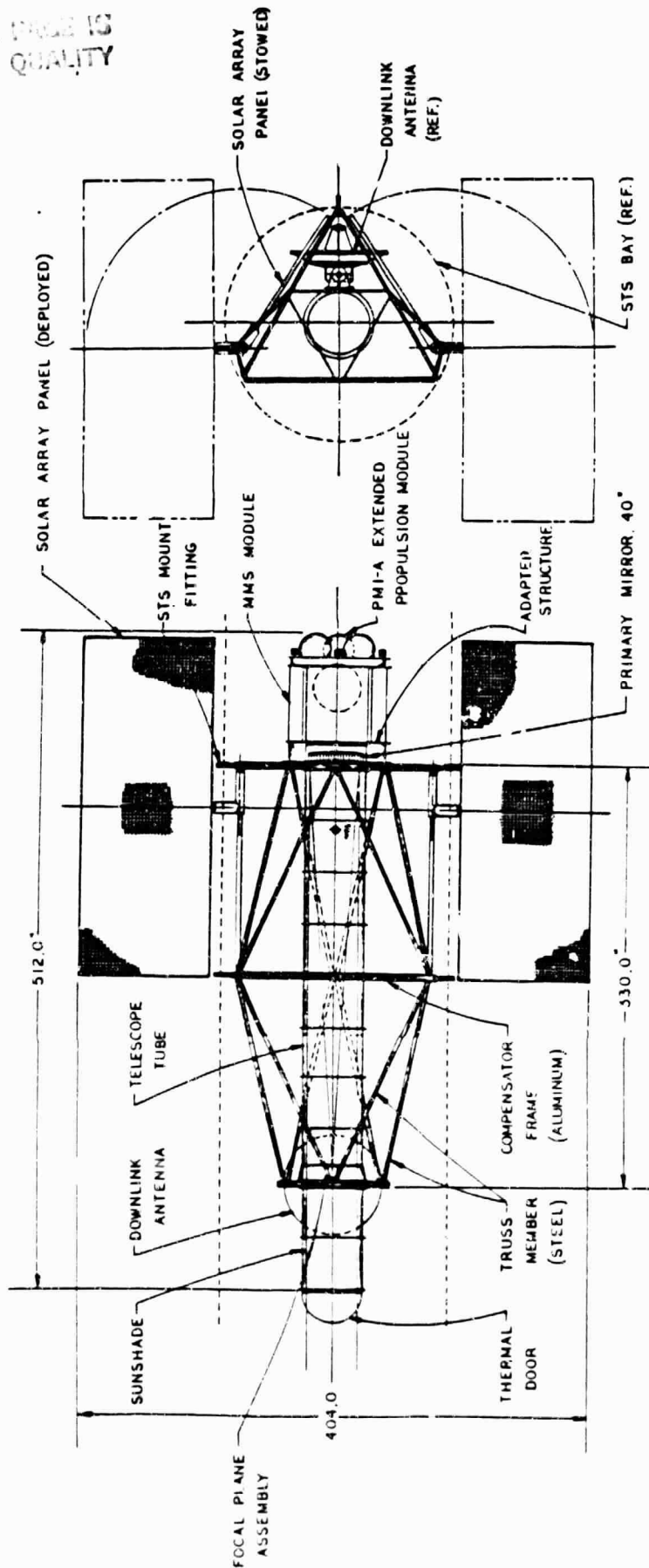


Fig. 6-4 F/8 Astrometric Telescope System

ORIGINAL PAGE IS  
OF POOR QUALITY

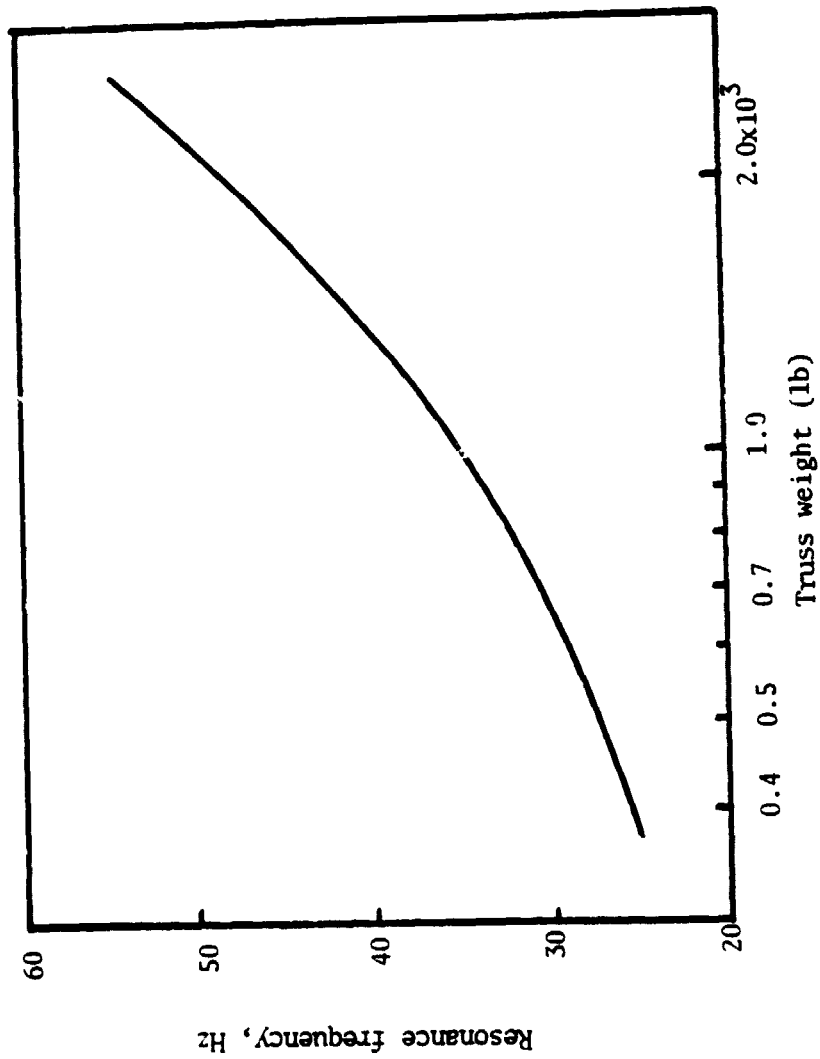


Fig. 6-5 Structure Resonance Frequency

members are bolted together. For maximum stiffness the structure consists of a series of isosceles triangles, each with the short leg of aluminum and the two long legs of steel, equally inclined to the longitudinal (athermalized) axis (which is the optical axis). As the temperature increases uniformly over the truss, the steel members would cause the structure to increase in length. However, the apex angle of each triangle increases since aluminum has a greater expansion coefficient than steel. By selecting the angle properly, the decrease caused by the aluminum just cancels the increase by the steel. Instead of steel-aluminum, steel-invar can also be used. The apex angle would be different. A nearly uniform temperature can be achieved by multilayer insulation of the truss and selective application of heat. The anticipated temperature control is in the range  $0.1-1^{\circ}\text{F}$ , and the heat dissipation a few ten watts.

#### 6.4.2 Telescope

The telescope subsystems are (i) the primary mirror, 40" diameter, solid ULE, parabolic,  $f/8$ ; and a standard triple bi-pod support structure; (ii) the primary baffle mask assembly, (iii) the light tube with baffles, non-structural and thermally insulated; (iv) the focal plane assembly, including ULE Ronchi ruling (50 cm length; 25 cm width) and support/drive; detectors and electronics; (v) the sunshade and thermal door. Thermal control of the payload is provided by insulation blankets, sensors and heaters.

#### 6.4.3 Spacecraft

The spacecraft is the baseline MMS with the maximum PM-1A propulsion module for one-way orbit transfer, plus additional batteries, antennas, solar arrays. The solar arrays (2 panels) have a total area of  $350\text{ ft}^2$  (3.5 kW power) and one degree of freedom for sun-tracking.

#### 6.4.4 Weights

A detailed weight break down is given in Table 6-5. The overall weights, which include 10% contingency, are as follows:

Telescope	2749 lb
MMS (dry)	1907
Mission peculiar equipment	1058
Propellant (hydrazine)	588
total	<hr/> 6302 lb (2859 kg)

#### 6.4.5 Cost

A cost breakdown is shown in Table 6-6. The cost basis is as follows:

1. Development includes component brassboards and a protoflight unit
2. The MMS spacecraft is used without modifications
3. Launch and operations are not included
4. No new facilities were identified
5. Data processing on the ground (and software development for that purpose) is not included. It is assumed to be part of the operations cost of part of the PI budget.

The cost estimates were derived parametrically in 1982 \$ and represent placeholder numbers associated with the current state of program definition. The cost of \$148M total is made up of mission equipment \$92M, spacecraft user-defined equipment \$41M, and payload-spacecraft integration \$15M. Cost estimates for the payload are uncertain to about 25%; the MMS cost on production rate and is uncertain by about 10%. Thus the net uncertainty is about 15%.

TABLE 6-5  
F/8 TELESCOPE WEIGHT ESTIMATES

	Lb	Kg
TELESCOPE		
<u>Structures</u>		<u>532.5</u>
Metering truss	840	
Primary baffle & Mask assembly	135	
Light tube and baffles	135	
Spacecraft adapter	64	
<u>Thermal Control</u>		<u>188.2</u>
Insulation blankets	120	
Thermal control electronics	25	
Heaters and sensors	35	
Thermal door and drive	175	
Air-conditioning (pre-launch)	40	
Bracketry, etc.	20	
<u>Optics</u>		<u>353.8</u>
Primary Mirror	540	
Primary Mirror Support	240	
<u>Focal Plane Assembly (FPA)</u>		<u>145.2</u>
FPA	160	
Support	160	
<u>Command &amp; Control Computer</u>	60	<u>27.2</u>
Telescope total	<u>2749</u>	<u>1246.9</u>
MISSION PECULIAR EQUIPMENT		
<u>Antennas</u>		<u>45.4</u>
High gain downlink dish (2)	60	
Cabling, connectors, etc.	40	
<u>Electrical</u>		<u>434.6</u>
Batteries (2)	180	
Solar array including structure	450	
Power conditioners (added)	60	
Charge controllers (added)	48	
Cabling, connectors, etc.	220	
MPE total	<u>1058</u>	<u>480</u>
SPACECRAFT		<u>1134</u>
MMS dry	1907	
Propellant & pressurants	588	
Grand Total	6302 =====	2895 =====



TABLE 6-6

F/8 TELESCOPE COST (\$1982M)

MISSION EQUIPMENT

Optics & Support Structure	4.52
FPA, Support & Electronics	5.95
Motorized Grating, Electronics & Software	13.10
Alignment system, Computer, S/W	7.47
Structure	21.63
Thermal & Doors	6.50
<hr/>	
Design, Development & hardware	59.17
GSE, GHE & STE	5.26
Integration & Test	8.87
Systems Engineering, Q.A, & Reliability	12.06
Program Manag.t & Data	6.72
<hr/>	
ME total	92.08

SPACECRAFT & INTEGRATION

MMS Bus	
Propulsion Module PM1-A	
S/C Simulator & GSE (on loan)	} 35.00
MMS Bus Integration & Test	
Mission peculiar equipment	
Solar arrays & batteries	5.00
Antennas	1.00
Overall integration & test	15.00
<hr/>	
S/C & Integr. subtotal	56.00

Grand total 148.03  
=====

#### 6.4.6 Variation of Cost with Mirror Diameter

Cost estimates were also prepared for 8-m focal length systems with 0.5 m and 2 m mirror diameters. The results are shown in Fig. 6-6 (for the 2-m mirror a lightweight construction was assumed). The payload cost varies very slowly with mirror diameter, and, if a fixed spacecraft plus integration cost is assumed (same as for the f/8 system), the total sensor cost even more slowly.

A 0.5 m mirror system is probably not cost-effective because the system is a factor 16 slower than with a 1 m mirror (there will also be significant blocking of the FOV by the focal plane). A 2-m mirror telescope (f/4) has significantly more coma than the 1-m diameter, 8-m focal length system: The rms spot size at 0.707 field is a factor 4 larger, therefore the accuracy (assumed to be proportional to rms spot size) by the same factor worse. The integration time for a 2-m system (8-m focal length) is thus about the same as for a 1-m, f/8 system since it is proportional to  $(\text{spot size})^2 / (\text{diameter})^4$ . Fig. 6-7 shows the variation of the merit parameter (cost x integration time)<sup>-1</sup> (normalized to unity for the f/16 system) as a function of mirror diameter. An optimum diameter may be found by detailed trade studies. We assume the f/8 system as an initial baseline.

#### 6.4.7 Dual-Barrel Telescope

A variant of the f/8 concept is two identical optical systems in a single structure (identical optical trains, focal plane, etc.) The x and y components of stellar positions are measured simultaneously (the Ronchi rulings are inclined 90° to each other) instead of sequentially. The concept offers these advantages:

1. No coupling of x-and y-measurement errors
2. No rotation of telescope or focal plane
3. Built-in redundancy (if one system fails the other can still measure x and y by rotating the telescope)

Table 6-7 shows a cost estimate for a dual-barrel telescope (payload only). The cost is 23% above that of a single-barrel telescope (1 m mirror diameter always assumed). The cost increase is modest because there is only one optical design, and computers and alignment systems are shared. (Additional software is charged to the second barrel because of increased software complexity).

ORIGINAL PAGE IS  
OF POOR QUALITY

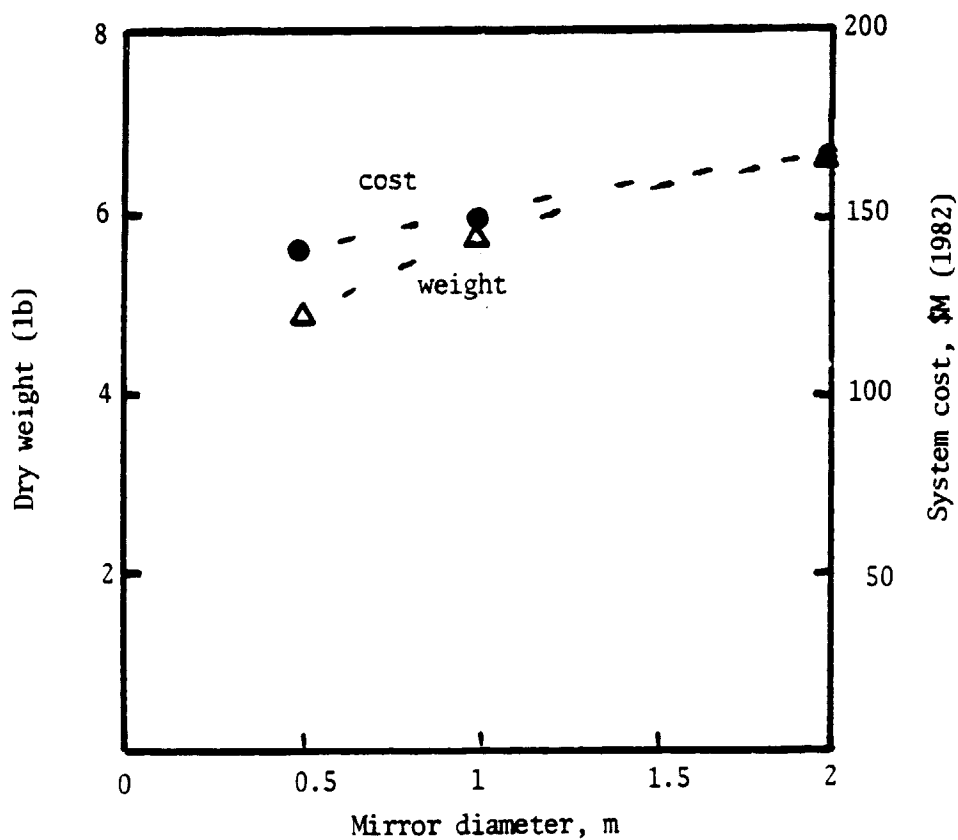


Fig. 6-6 Weight and Cost of Telescopes

TABLE 6-7  
DUAL BARREL F/8 TELESCOPE COSTS  
(\$1982M)

MISSION EQUIPMENT	BASIC TELESCOPE	SECOND BARREL	TOTAL
Optics & Support Structure	4.5	1.8	6.3
FPA, Support & Electronics	5.9	1.7	7.6
Grating, Electronics & S/W	13.1	3.5	16.6
Alignment, Computer & S/W	7.5	1.5 (S/W)	9.0
Telescope Structure	21.6	3.9	25.5
Thermal & Doors	6.5	1.5	8.0
	<hr/>	<hr/>	<hr/>
Design, Dev.t, H/W	59.1	13.9	73.0
GSE, GHE, STE	5.3	0.8	6.1
Integration & Test	8.9	2.5	11.4
Syst. Eng., Q.A., Rel.	12.1	2.7	14.8
Prog. Managt. & Data	6.7	1.6	8.3
	<hr/>	<hr/>	<hr/>
ME Total	92.1	21.5	113.6
			=====

ORIGINAL PAGE IS  
OF POOR QUALITY

LMSC-D870885

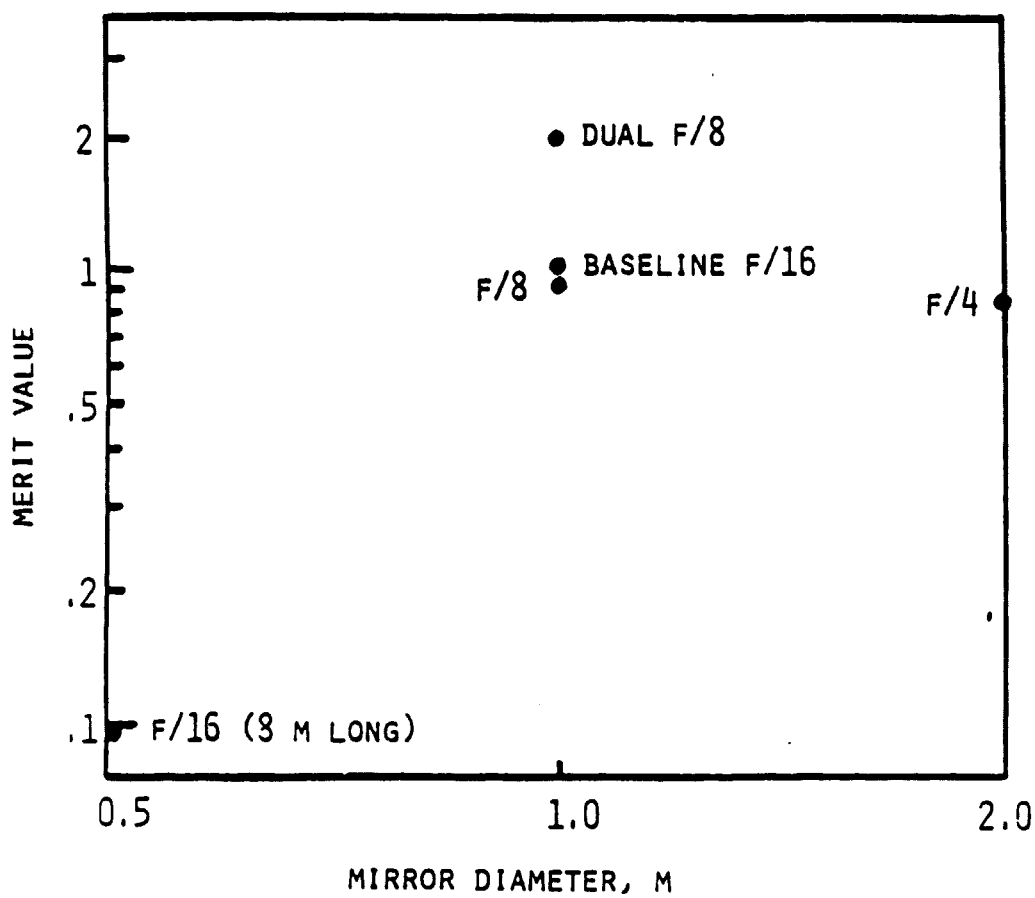


Fig. 6-7 Cost-Effectiveness

## APPENDIX A

### INDIRECT VERSUS DIRECT DETECTION OF EXTRA-SOLAR PLANETS

In a previous study\* the feasibility of direct detection of extra-solar planets with an earth-orbiting instrument was studied. As in the present study, two competing instruments were evaluated for feasibility and compared, and again, the two instruments were an imaging telescope and an interferometer. Similarities as well as differences between the two sets of instruments are highlighted in Table A-1.

The main problem of direct detection is to resolve the star and planet images, the planet being close to and much fainter than the parent star. The two methods of separation of the images were: For the imaging telescope (APOTS), which operates in the visible part of the spectrum, the diffraction wings of the star image were reduced in intensity by apodizing the telescope aperture. For the interferometer (IRIS), which operates in the infrared ( $26\mu\text{m}$ ) the star image was nulled out by pointing the optical axis of the interferometer at the star and rotating the interferometer about its axis.

While there were no questions concerning the feasibility of the interferometer, but substantial challenges such as long-term cooling of the primary mirrors to 30 K, the imaging telescope concept was beset with the apparently insurmountable difficulty of manufacturing and maintaining a very smooth mirror surface. In the visible, mirror ripple causes light from the parent star to be scattered to the diffraction wings to such an extent that the theoretical performance potential derived from apodization, could not be achieved to within several orders of magnitude, as measured in integration time for the baseline task: detection of a Jupiter mass planet around a Sun-like star at 10 parsecs. The estimated

Table A-1

Comparison of Instruments for Detection of Extra-Solar Planets

Mission duration, yrs.	<u>Direct Detection (APOTS/IRIS)</u>		<u>Indirect Detection (Astrometry)</u>	
	Shuttle + boost, free-flyers		Shuttle + boost, free-flyers	
Deployment				
Orbit, n. ml.	300		325	
Primary aperture dia., m.	3		1	
Largest dimension, m.	13, baseline separation (IRIS) 15, focal length (APOTS)		15, baseline separation (Interferometer) 16.5, focal length (Telescope)	
Weight - dry, kg.	6600 IRIS 6300 APOTS		4500 (I) 3800 (T)	
Wavelength	26 + 2 m (IRIS) 4000 - 7000 Å (APOTS)		4000 - 7000 Å	
Baseline task	detection of Jupiter-type planet around sun-like star, from a distance of 10 pc		detection of earth-type planet in a 5-yr orbit around K5 star, at distance 10 pc	
Baseline integration time, t, hrs.	1 (IRIS) 100 (APOTS)		.2 (I) 8 (T)	
Sensitivity of t to L, D	D <sup>-4</sup> L <sup>-4</sup> (IRIS) D <sup>-5</sup> (APOTS)		D <sup>-2</sup> L <sup>-2</sup> (I) D <sup>-4</sup> (T)	
Technical challenges	cryo-cooling of large Be-optics (IRIS) smooth primary mirror (APOTS)		OPD measurement to 1 Å precision (I) efficient detector mosaics (T)	

LASC-D870885

LMSC-D870885

integration time for the two instruments was in the ratio  
interferometer:telescope = 1:100.

---

\* "Systems Level Feasibility Study for the Detection of Extra-Solar Planets", Vol. 1: Infrared Interferometer (IRIS), Vol. 2: Apodized Telescope (APOTS). LMSC-D676425 (July 1979).